AD-A067 311 NEW MEXICO STATE UNIV LAS CRUCES PHYSICAL SCIENCE LAB F/G 9/5
THEORETICAL INVESTIGATION OF THE MICROSTRIP ANTENNA.(U)
JAN 79 K R CARVER, E L COFFEY DAAG29-78-G-0082
UNCLASSIFIED PT-00929 ARO-15384.1-EL NL

1 OF 1
AD
A067311

END
DATE FILMED
6-79
DDC

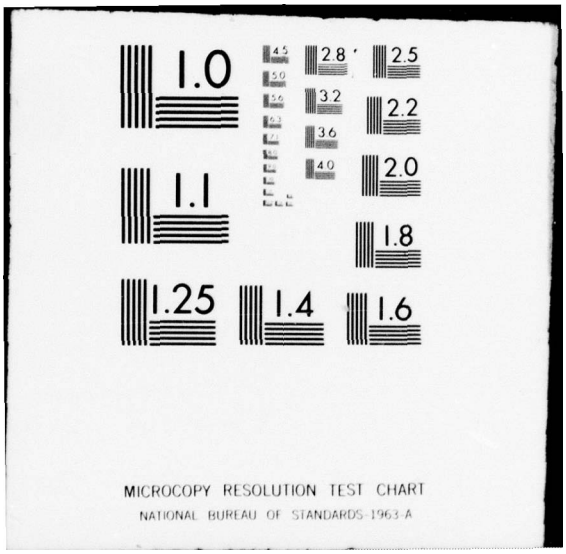
1.0
1.1
1.25
1.4
1.6
1.8
2.0
2.2
2.5
2.8
3.2
3.6
4.0
4.5
5.0
5.6
6.3
7.1
8.0
9.0
MICROCOPY RESOLUTION TEST CHART
NATIONAL BUREAU OF STANDARDS-1963-A

LEVEL II

(5)

Technical Report PT-00929

THEORETICAL INVESTIGATION OF THE MICROSTRIP ANTENNA

A Semi-Annual Progress Report

by

Keith R. Carver

Edgar L. Coffey

AD A067311

DDC FILE COPY

DDC
RECEIVED
APR 12 1979
C

prepared for

Army Research Office
Research Triangle Park
Durham, N.C.

ARO Grant DAAG29-78-G-0082

January 23, 1979

NEW MEXICO STATE UNIVERSITY

Physical Science Laboratory

BOX 3-PSL, LAS CRUCES, NEW MEXICO 88003
AREA (505) 522-4400 TWX 910-983-0541

79 04 09 101

Unclassified

SECURITY CLASSIFICATION OF THIS PAGE (When Data Entered)

(18) ARO

REPORT DOCUMENTATION PAGE

READ INSTRUCTIONS BEFORE COMPLETING FORM

1. REPORT NUMBER: (19) 15384.1-EL	2. GOVT ACCESSION NO. (2) 5 semi-annual progress rept. (2)
3. RECIPIENT'S CATALOG NUMBER	
4. TITLE (and Subtitle): (6) Theoretical Investigation of the Microstrip Antenna	5. TYPE OF REPORT & PERIOD COVERED: Technical
	6. PERFORMING ORG. REPORT NUMBER
7. AUTHOR(s): (10) Keith R. Carver, Edgar L. Coffey	8. CONTRACT OR GRANT NUMBER(s): (15) DAAG29-78-G-0082
9. PERFORMING ORGANIZATION NAME AND ADDRESS: New Mexico State University, Las Cruces, New Mexico 88003	10. PROGRAM ELEMENT, PROJECT, TASK AREA & WORK UNIT NUMBERS
11. CONTROLLING OFFICE NAME AND ADDRESS: U. S. Army Research Office, P. O. Box 12211, Research Triangle Park, NC 27709	(11) 12. REPORT DATE: 23 Jan 79 13. NUMBER OF PAGES: 85
14. MONITORING AGENCY NAME & ADDRESS (if different from Controlling Office): (14) PT-00929	(12) 91p. 15. SECURITY CLASS. (of this report): Unclassified 15a. DECLASSIFICATION/DOWNGRADING SCHEDULE

16. DISTRIBUTION STATEMENT (of this Report)

Approved for public release; distribution unlimited.

17. DISTRIBUTION STATEMENT (of the abstract entered in Block 20, if different from Report)

18. SUPPLEMENTARY NOTES

The view, opinions, and/or findings contained in this report are those of the author(s) and should not be construed as an official Department of the Army position, policy, or decision, unless so designated by other documentation.

19. KEY WORDS (Continue on reverse side if necessary and identify by block number)

microstrip antennas
design techniques
systems applications
cylindrical arrays
planar-arrays
geosynchronous satellites
transmission-line theory

20. ABSTRACT (Continue on reverse side if necessary and identify by block number)

This report begins with a discussion of a general mathematical framework for the analysis of microstrip antennas. A discussion is then presented of methods based on the finite elements approach along with key aspects of a computer code developed along these lines. Next, a classical modal expansion method is presented and applied to both rectangular and circular patches. Finally, the finite-elements approach is used to solve for the magnetic currents on the radiating walls of a five-sided patch which can produce circular polarization.

DD FORM 1 JAN 73 1473 EDITION OF 1 NOV 65 IS OBSOLETE

Unclassified 282 450

Technical Report PT-00929

THEORETICAL INVESTIGATION OF THE MICROSTRIP ANTENNA

A Semi-Annual Progress Report

by

Keith R. Carver

Edgar L. Coffey

DDC
RECEIVED
APR 19 1979
C

prepared for

Army Research Office
Research Triangle Park
Durham, N.C.

ARO Grant DAAG29-78-G-0082

January 23, 1979

NEW MEXICO STATE UNIVERSITY

Physical Science Laboratory

BOX 3-PSL, LAS CRUCES, NEW MEXICO 88003
AREA (505) 522-4400 TWX 910-983-0541

282450

THEORETICAL INVESTIGATION OF THE MICROSTRIP ANTENNA

A Semi-annual Progress Report

by

Keith R. Carver

Edgar L. Coffey

prepared for

Army Research Office

Research Triangle Park

Durham, N.C.

ARO Grant DAAG29-78-G-0082

January 23, 1979

Physical Science Laboratory

New Mexico State University

Las Cruces, N. M. 88003

TABLE OF CONTENTS

1.0 INTRODUCTION 1

2.0 THEORETICAL MODELS 3
2.1 Introduction 3
2.2 Notation 5
2.3 Formalism for the Interior Problem 5
2.3.1 Complex Source Power 9
2.3.2 Dissipated Power 10
2.3.3 Radiated Power 10
2.3.4 Stored Energy 11
2.3.5 Input Impedance 13
2.3.6 Impedance Bandwidth 16
2.3.7 Antenna Efficiency 17
2.4 Formalism for the Exterior Problem 18

3.0 NUMERICAL TECHNIQUES FOR THE INTERIOR PROBLEM 27
3.1 Mathematical Development and Numerical Implementation 28
3.2 Numerical Difficulties Overcome/ to be Overcome . . . 31
3.2.1 Matrix Calculations for Irregular Polygons . . 31
3.2.2 Impedance Boundary Conditions 32
3.2.3 Eigenvalue/Eigenvector Computation 33
3.2.4 Size of Matrices vs. Core Memory 35

4.0 RESULTS FOR SPECIFIC MICROSTRIP ANTENNAS 37
4.1 The Rectangular Patch 37
4.1.1 Closed Cavity Formulation 37
4.1.2 Radiating Cavity Formulation 41
4.1.3 Multiple-Mode Effects 60
4.2 The Circular Patch 67
4.3 The Pentagon Patch 73

ACCESSION for
NTIS White Section
DDC Buff Section
UNANNOUNCED
JUSTIFICATION
BY
DISTRIBUTION/AVAILABILITY CODES
Dist. SPECIAL
A

5.0 CONCLUSIONS 80

6.0 REFERENCES 82

1.0 INTRODUCTION

This report presents theoretical techniques which may be used in the analysis and design of microstrip antennas. The involvement of the Physical Science Laboratory in the theoretical analysis of these electrically thin radiators has been principally motivated by a practical requirement for better design techniques which could be applied to the development of microstrip antennas for systems applications. Over the past seven years, PSL has acquired considerable practical experience in the design of both stripline and microstrip antennas; microstrip antennas have been produced in wrap-around cylindrical arrays for sounding rocket application [Weinschel, 1975] and in planar-array versions for UHF communication from buoys and ships to geosynchronous satellites [Weinschel and Carver, 1976]. Until recently, however, these designs have come from a combination of experimental cut-and-try techniques supplemented by standard transmission-line theory applied to simple rectangular patches.

The microstrip antenna concept dates back some twenty-five years to work by Deschamps [1953]. However, nearly eighteen years passed before the work was renewed and reported by J. Q. Howell at NASA Langley Research Center [1972, 1975], R. E. Munson at Ball Brothers Research Corporation [1972, 1975] and H. D. Weinschel at the Physical Science Laboratory [1973, 1975].

Mathematical modeling of the basic microstrip radiator was initially carried out by applying transmission-line analogies to simple rectangular patches fed at the center of a radiating wall [Munson, 1974; Derneryd, 1976]. The radiation pattern of a circular patch was analyzed and measurements reported by Carver [1976].

These earlier mathematical models, while giving reasonably good results for center-fed rectangular patches, all shared some serious deficiencies: (1) they consistently predicted resonant frequencies which were a few percent off (usually on the high side) from measured resonant frequencies, (2) they could not be adapted to multi-mode structures with arbitrary feed points (such as corner-fed rectangular patches), and (3) they could not be adapted to patches of arbitrary shape.

The present analytical work began in January, 1977 and received ARO support beginning in April, 1978. It has been directed along two complementary paths: (a) for rectangular and circular patches, a modal expansion

method incorporating impedance boundary conditions at the radiating walls, and (b) for patches of arbitrary shape, a numerical approach based on the method of finite elements. The initial proposal for the numerical analysis was to use the Unimoment-Monte Carlo technique [Coffey, 1976; Coffey and Carver, 1977]; however, for reasons discussed in Sec. 3.0, this numerical technique has been abandoned in favor of the method of finite elements. During the course of this effort, a comprehensive report was received from workers at the University of Illinois [Lo, et. al., 1977] which used a similar expansion method applied to impedance and radiation pattern analysis of rectangular, circular and triangular patches. One of the differences between the Illinois report and the present approach is that the latter incorporates impedance boundary conditions at the radiating walls, whereas the former does not. The wall conductance used in the present report is based on a parallel-plate TEM waveguide radiating into a half-space [Marcuvitz, 1949; Harrington, 1961]. The wall susceptance is based on a formulation by Hammerstad [1975]. The result of this model is a prediction of impedance vs. frequency behavior which shows very good agreement with measured results for rectangular patches; there is also good agreement with measured results for circular patches.

This report begins with a discussion of a general mathematical framework for the analysis of microstrip antennas. A discussion is then presented of methods based on the finite elements approach along with key aspects of a computer code developed along these lines. Next, a classical modal expansion method is presented and applied to both rectangular and circular patches. Finally, the finite-elements approach is used to solve for the magnetic currents on the radiating walls of a five-sided patch which can produce circular polarization.

2.0 THEORETICAL MODELS

2.1 Introduction

A microstrip antenna is shown in Figure 2.1 as a patch of arbitrary shape separated from a large ground plane by a homogeneous dielectric of thickness t, where t is assumed to be much less than a wavelength. Practical microstrip antennas have been fabricated with rectangular, circular, semi-circular, triangular and pentagonal patch shapes. It is therefore of interest to develop a theoretical foundation which can handle patches of arbitrary size and shape.

The objectives of such an analysis are to predict both the far-field pattern characteristics (including gain and polarization) as well as such near-field characteristics as input impedance, impedance bandwidth, antenna efficiency, mutual coupling, etc. This is an ambitious program and will require the efforts of many investigators before it is completed. It is expected that approximation methods will be needed in order to obtain practical answers. However, to date there have been no publications in the open literature which attempted to set up a formalism for the microstrip antenna based on a rigorous approach. It seems worthwhile to attempt such an attack even though satisfactory solutions may be difficult.

The analysis of the microstrip antenna may be facilitated by dividing the radiation into an interior region and an exterior region. The interior region is a cavity formed by the patch, the portion of the ground plane under the patch, and the radiating walls formed by the projection of the patch perimeter onto the ground plane. The exterior region is the rest of space and includes the remainder of the ground plane, the remainder of the dielectric and the top of the patch conducting surface. Practical ground planes are usually several wavelengths in dimension so that the assumption of an infinite ground plane is justified for purposes of computing the far-field pattern shape over most of the upper hemisphere. However, for angles near the plane of the ground plane, edge diffraction effects must be considered.

The connection between the interior and exterior problems may be made by enforcing the boundary condition that there be continuity of the tangential

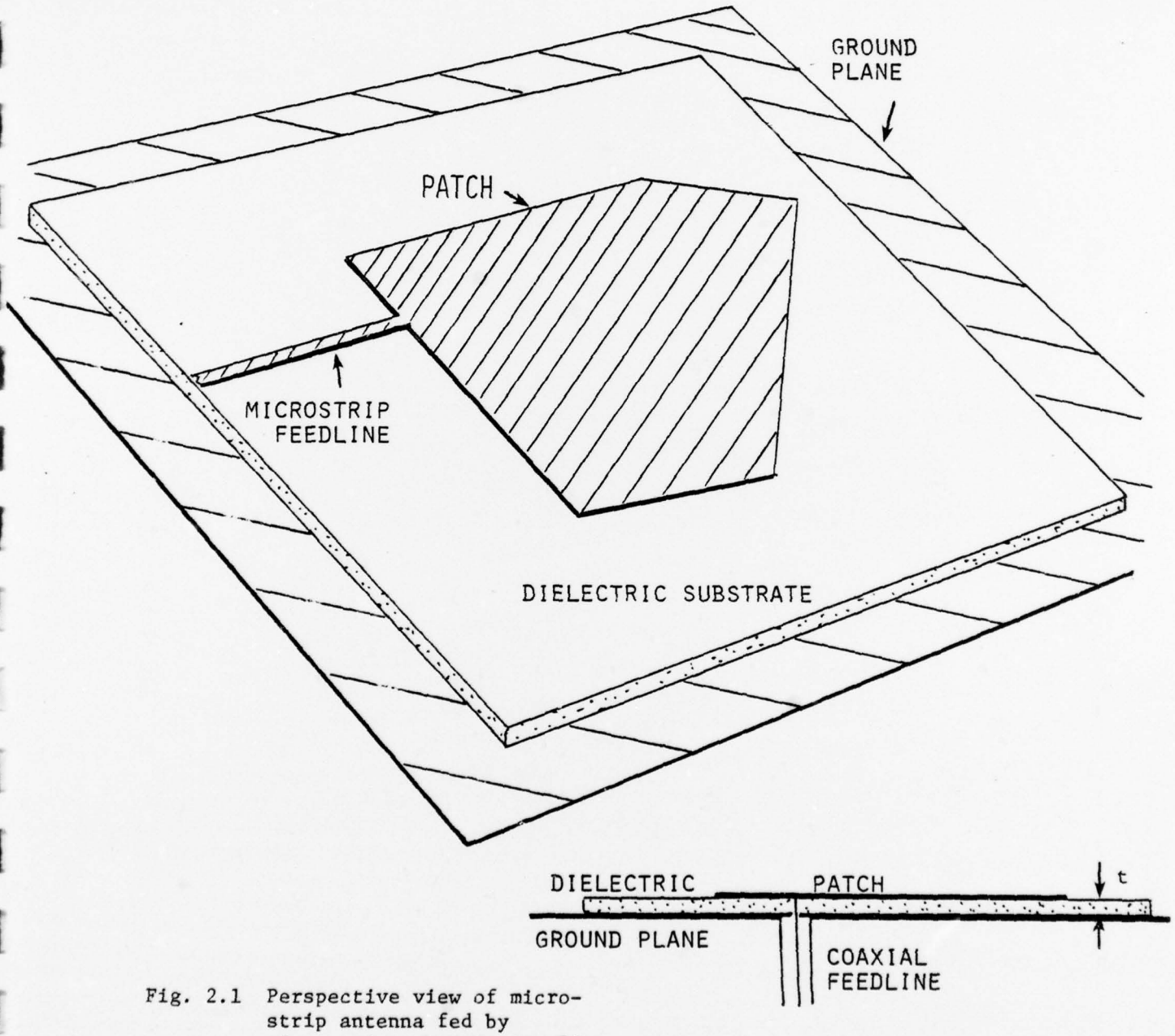

Fig. 2.1 Perspective view of microstrip antenna fed by microstrip transmission line; side view of microstrip ant. fed by coaxial line.

components of $\overline{E}$ and $\overline{H}$ at the radiating walls of the cavity. This is an extremely difficult problem and has not to date been solved.

2.2 Notation

A notation is needed which explicitly identifies both interior and exterior fields. If the distinction between interior and exterior fields is not obvious from context, the symbol i used as a superscript will identify an interior field, i.e., $\overline{E}^i$ or $\overline{H}^i$. Similarly, ($\overline{E}^e$, $\overline{H}^e$) are exterior fields.

Subscripts are then used to denote either mode indices (vide Section 3.0) or the value of a field at a particular location. In particular, the fields evaluated in the thin ribbon forming the radiating walls are denoted as ($\overline{E}_{rw}$, $\overline{H}_{rw}$). Fields evaluated on the exterior ground plane are denoted as ($\overline{E}_{gp}$, $\overline{H}_{gp}$) and exterior fields evaluated on the top of the radiating patch are denoted as ($\overline{E}_p$, $\overline{H}_p$).

As in most other published literature, primed coordinates are used to denote source point location and unprimed coordinates are used to denote field point location.

2.3 Formalism for the Interior Problem

Consider the interior region of a cavity with radiating side walls, as shown in Figure 2.2. Since $t \ll \lambda$, it may be assumed that the interior electric field is entirely z-directed and is independent of z.

The interior fields must satisfy the wave equation

$$\overline{\nabla} \times \overline{\nabla} \times \overline{E}^i - k^2 \overline{E}^i = - j\omega\mu_o \overline{J}^s - \overline{\nabla} \times \overline{M}^s \qquad (2.1a)$$

$$\overline{\nabla} \times \overline{\nabla} \times \overline{H}^i - k^2 \overline{H}^i = - j\omega\varepsilon \overline{M}^s + \overline{\nabla} \times \overline{J}^s \qquad (2.1b)$$

where

$$k^2 = \omega^2 \mu_o \varepsilon$$

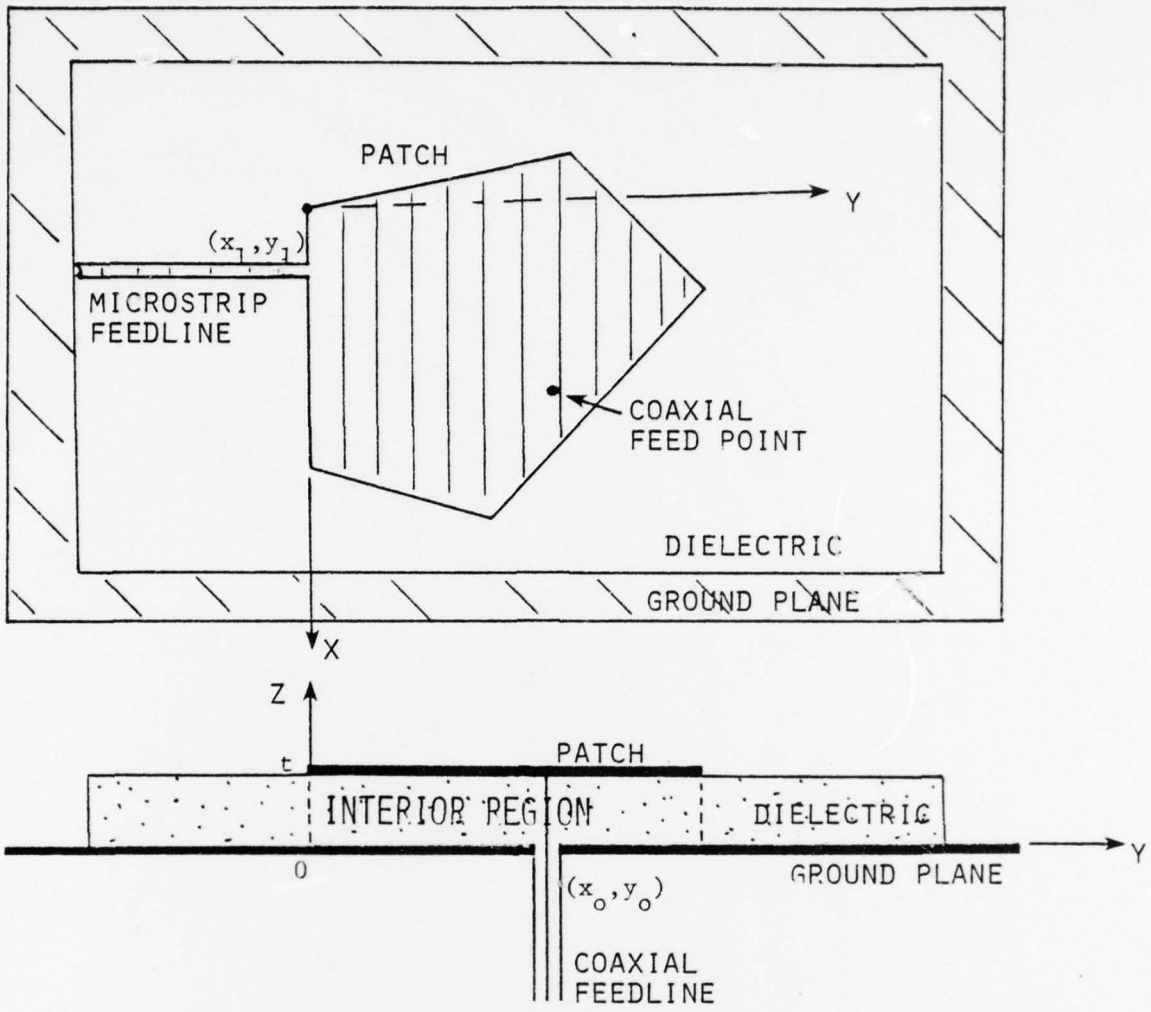

Fig. 2.2. Top and side views of a microstrip patch antenna showing both microstrip feedline and coaxial feedline methods of exciting patch; microstrip feedline point is (x_1, y_1) and coaxial feedline point is (x_o, y_o). Side view also shows interior region.

and

$$\varepsilon = \varepsilon' - j\varepsilon'' = \varepsilon_o(\varepsilon_r' - j\,\varepsilon_r'') \ . \tag{2.2}$$

$\overline{J}^s$ is the electric current density (A m^{-2}) due to the coaxial feedline source and may be written as

$$\overline{J}^s = \hat{z}\,\frac{I(z')}{a}\,\delta(x - x_o)\,\delta(y - y_o) \quad (o < z' < t) \tag{2.3}$$

where a is the cross-sectional area of the coaxial current element which is assumed to be electrically thin. $\overline{M}^s$ is the magnetic current density (V m^{-2}) due to the microstrip feedline source and may be written as

$$\overline{M}^s = \begin{cases} -\hat{x}\,\dfrac{V(x';o)}{tw}\,\delta(y) & (x_1 - \dfrac{w}{2} < x' < x_1 + \dfrac{w}{2}) \\ & (o < z' < t) \\ 0 & \text{otherwise} \end{cases} \tag{2.4}$$

where w is the width of the microstrip feedline and V(x';o) is the voltage between the patch and the ground plane evaluated at the feedline connection point.

For an antenna fed only by a microstrip feedline, $\overline{J}^s = 0$; similarly, for an antenna fed by a coaxial feeline, $\overline{M}^s = o$.

In addition to satisfying the wave equations (2.1), the fields must also satisfy the following boundary conditions*:

$$\hat{n} \times \overline{E}^i = o \qquad \text{(on top and bottom conductors)} \tag{2.5}$$

$$\left.\begin{aligned} \hat{n} \times \overline{E}^e_{rw} &= \hat{n} \times \overline{E}^e_{rw} \\ \hat{n} \times \overline{H}^i_{rw} &= \hat{n} \times \overline{E}^e_{rw} \end{aligned}\right\} \quad \text{(on radiating walls)} \tag{2.6}$$

*This first boundary condition assumes that the patch and the ground plane are perfect conductors. Since almost all practical microstrip antennas are fabricated from copper, this is an excellent assumption.

If the interior region were a non-radiating cavity, then $\overline{H}^e = o$ so that the tangential components of $\overline{H}^i$ at the radiating walls would be zero. In the language of classical boundary-value problems, this is known as a Neumann condition.

However, the practical problem must contend with radiating walls so that the interior fields must satisfy an impedance condition. A solution for the fields then requires a knowledge of the impedance presented by the radiating walls as a function of location on the wall.

The classical method for handling such cavities is to find a complete set of eigenvectors which can be used to expand the general field. This is not difficult for such simple geometries as rectangular and circular patches and has been discussed at some length by Lo, et. al. [1977]. If a complete basis cannot be found, approximation techniques such as the Ritz-Galerkin method, point matching, method of moments, etc., can be used to find the interior fields.

Section 3 of this report describes an approach to the interior problem using the method of finite elements. This method, which shows great promise, requires a knowledge of the impedance of the radiating walls or a reasonable approximation to it.

The balance of complex power for the interior region may be described by

$$P_{in} = P_R + P_d + 2j\omega (W_m - W_e) \tag{2.7}$$

where

P_{in} = complex power supplied by source
P_R = complex power radiated through edge walls
P_d = power dissipated by conducting walls and by the dielectric
ω = angular radian frequency
W_m = time-average magnetic energy stored in cavity
W_e = time-average electric energy stored in cavity

2.3.1 Complex Source Power

For microstrip antennas fed by coaxial lines, the input power may be computed by

$$P_{in}^{(c)} = - \iiint \bar{E}^i \cdot \bar{J}^* \, dv' \tag{2.8}$$

Using (2.3) for J and assuming $E^i = \hat{z} E^i$, (2.8) becomes

$$P_{in}^{(c)} = - \int_o^t E^i(x_o, y_o) \, I^*(z')dz' \tag{2.9}$$

If I(z') is a constant, then (2.9) becomes

$$P_{in}^{(c)} = V_{in} I_{in}^* \tag{2.10}$$

where

$$V_{in} = - \int_o^t E^i (x_o, y_o)dz' = - t \, E^i(x_o, y_o) \tag{2.11}$$

Because of the assumption that J^s was filamentary (c.f. eqn. 2.3) the reactive input power computed as the imaginary part of (2.9) will be in error. This will be discussed later.

For microstrip antennas fed by microstrip feedlines, the input power may be computed by

$$P_{in}^{(ms)} = - \iiint \bar{H}^{i*} \cdot \bar{M} \, dv' \tag{2.12}$$

Using (2.4) for $\bar{M}$ and assuming $\bar{H}^i = \hat{x} H_x^i + \hat{y} H_y^i$,

$$P_{in}^{(ms)} = \int_{x_1 - w/2}^{x_1 + w/2} \int_o^t (H_x^i)^* \frac{V(x';o)}{tw} \, dx' \, dz' \tag{2.13}$$

If the strip width is narrow, $V(x';o)$ is essentially constant and equal to V_{in} so that (2.10) becomes

$$P_{in}^{(ms)} = I_{in}^{*} V_{in} \tag{2.14}$$

where

$$I_{in} = \int_{o}^{t} H_{x}^{i} \, dz' \tag{2.15}$$

2.3.2 Dissipated Power

The power dissipated as heat can be subdivided into that associated with conductor losses (P_{dc}) and that associated with dielectric losses (P_{dd})

$$P_{d} = P_{dc} + P_{dd} \tag{2.16}$$

where [Kraus and Carver, 1973]:

$$P_{dc} = \text{Re } Z_{c} \iint_{\substack{\text{cond.} \\ \text{walls}}} |H_{tan}^{i}|^{2} \, ds \tag{2.17}$$

and

$$P_{dd} = w\varepsilon'' \iiint_{\text{cavity}} |E^{i}|^{2} \, dv \tag{2.18}$$

2.3.3 Radiated Power

The complex radiated power is obtained by integrating the complex Poynting vector over the radiating wall surface, i.e.

$$P_{R} = \iint_{\substack{\text{rad.} \\ \text{wall}}} (\bar{E}^{i} \times \bar{H}^{i*}) \cdot d\bar{s} \tag{2.19}$$

Since $\bar{E}^i$ is entirely z-directed, the only component of $\bar{H}^i$ which is of interest is that tangent to the radiating wall and parallel to the local edge of the patch; this component is designated as H_ℓ. Thus,

$$P_R = - \int_{\substack{\text{wall} \\ \text{perimeter}}} V_\ell \, H_\ell^* \, d\ell \tag{2.20}$$

where V_ℓ is the voltage across the radiating wall and H_ℓ is the parallel component of the magnetic field. H_ℓ is also related to the surface electric current density at the edge, as shown in Figure 2.3, by the boundary condition

$$\bar{J}_s = \hat{n} \times \bar{H}_\ell \tag{2.21}$$

where $\hat{n}$ is a unit normal directed away from the conducting surface. If $\bar{H}_\ell$ is entirely tangent to the radiating wall, then the current on the bottom side of the patch will flow around the edge and onto the top side of the patch, as shown. The electric field just exterior to the radiating wall will fringe and refract at the dielectric-air interface in accordance with Snell's Law.

2.3.4 Stored Energy

The total stored energy in the cavity is given by

$$W = W_m + W_e = \frac{1}{2} \iiint_{\text{cavity}} (\varepsilon |E^i|^2 + \mu_o |H^i|^2) dv \tag{2.22}$$

Since the interior fields are independent of z, this can be slightly simplified to

$$W_e = \frac{1}{2} \varepsilon \, t \iint_{\substack{\text{cavity} \\ \text{area}}} |E^i|^2 \, ds \tag{2.23}$$

$$W_m = \frac{1}{2} \mu_o \, t \iint_{\substack{\text{cavity} \\ \text{area}}} |H^i|^2 \, ds \tag{2.24}$$

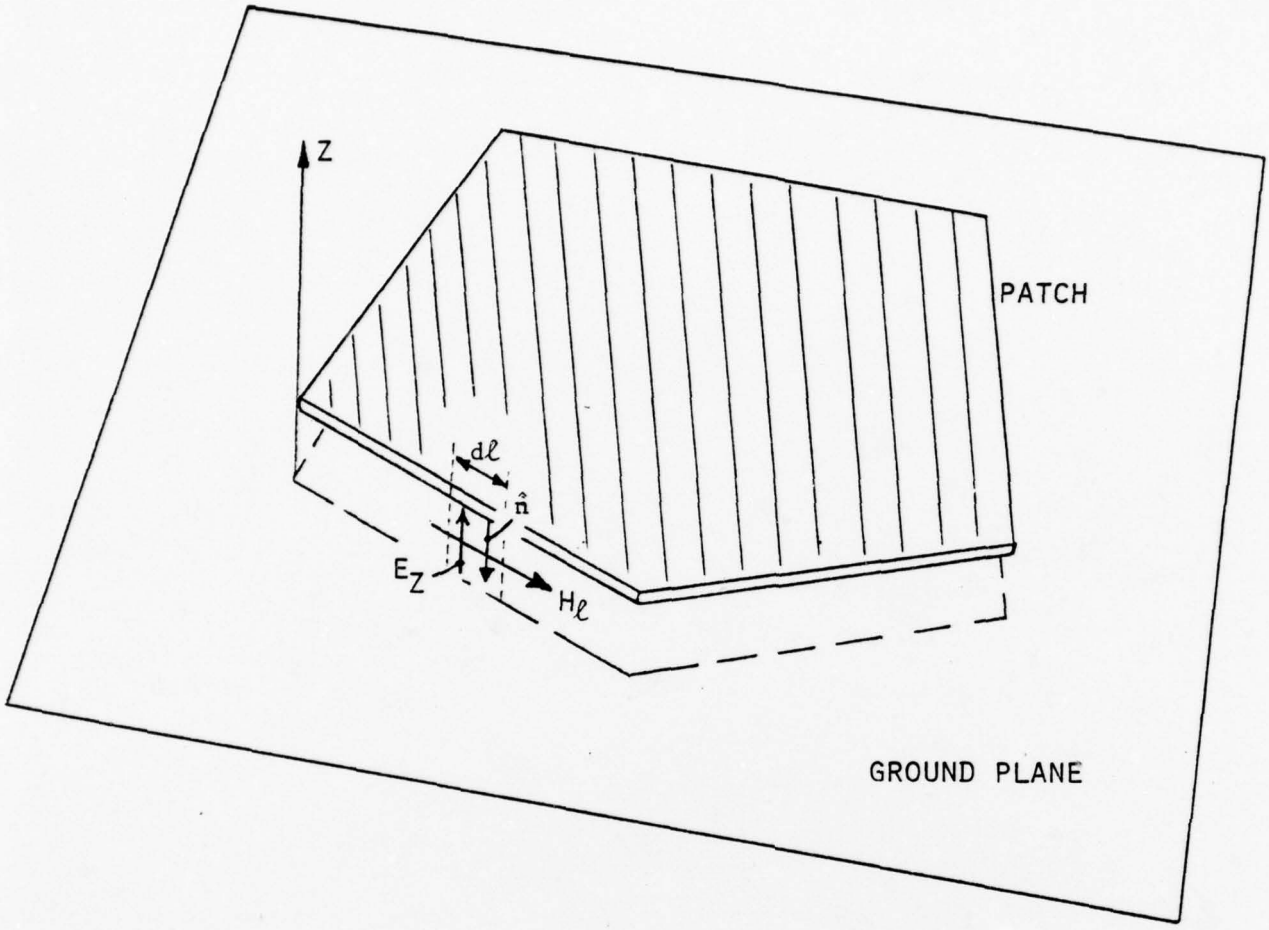

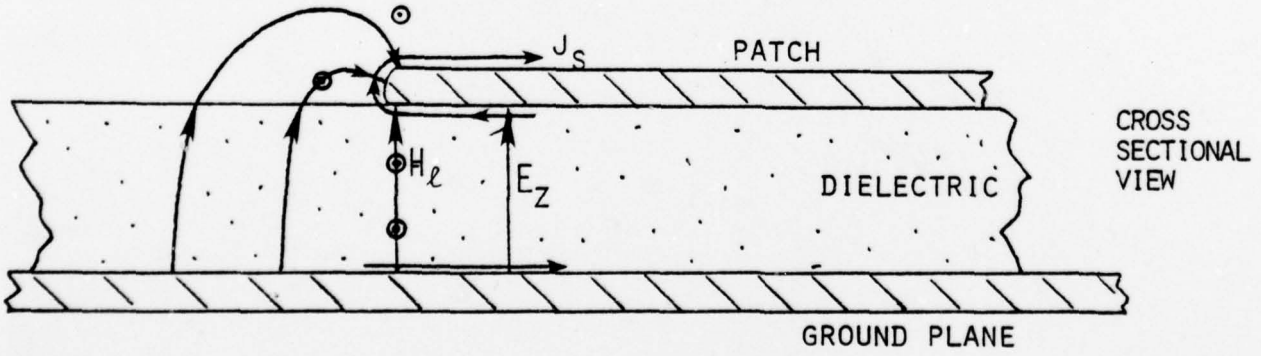

Fig. 2.3. Illustrating relationships between fields and electric current density at radiating wall.

2.3.5 Input Impedance

The input impedance to a coaxially-fed microstrip antenna can be computed by noting the $P_{in} = |I_{in}|^2 Z_{in}$ and using (2-9) to obtain

$$Z_{in} = -\frac{1}{|I_{in}|^2} \int_0^t E^i(x_o,y_o) I^*(z')\, dz' \qquad (2\text{-}25)$$

where a z-directed filamentary probe has been assumed. Similarly, the input admittance to a microstrip transmission line-fed microstrip antenna can be computed by noting that $P_{in} = |V_{in}|^2 Y_{in}$ and using (2-12) to obtain

$$Y_{in} = \frac{1}{|V_{in}|^2} \int_0^w [H^i(x_1,y_1)]_{\ell}^* V(\ell)\, d\ell \qquad (2\text{-}26)$$

where the feedline input has been modeled as a thin strip of magnetic surface current density $\bar{M}_s = (\hat{z} \times \hat{n})(V/t)$ where $\hat{n}$ is a unit vector normal to the thin radiating surface and pointing into the cavity. The strip is of width w. If the strip width is narrow, then $V(\ell)$ is essentially constant and equal to V_{in}. If t is small, then the input current on the lower side of the upper microstrip transmission-line conductor is $I_{in} = [H^i(x_1,y_1)]w$, so that

$$Y_{in} = (I_{in}/V_{in})^* \qquad (2\text{-}27)$$

Likewise, from (2-25), if a small value of t is assumed then both E^i and I(z') are constant so that

$$Z_{in} = V_{in}/I_{in} \qquad (2\text{-}28)$$

The usual procedure for a probe-fed cavity is to find $V_{in} = -tE_z(x_o,y_o)$ by expanding $E_z(x,y)$ in terms of a complete set of orthogonal modal vectors (eigenfunctions) $e_{mn}(x,y)$ and using the orthogonality property to find the coefficients of the expansion in terms of the input current. A similar procedure can be used for the microstrip-line fed cavity by

finding $I_{in} = [H^i(x_1,y_1)]w$ and expanding H^i.

In this classical eigenvalue problem, a denumerably infinite set of discrete eigenvectors and eigenvalues are found by imposition of either Dirichlet ($E_z = 0$ on boundaries) or Neumann ($\partial E_z/\partial n = 0$ on boundaries) boundary conditions. The mode vectors are customarily orthonormalized as follows:

$$\epsilon \iiint_{\substack{\text{cavity} \\ \text{volume}}} \bar{e}_{mn} \cdot \bar{e}_{pq} \, dv = \delta_{mn,pq} \tag{2-29}$$

where $\delta_{mn,pq} = 1$ if $m = p$ and $n = q$; $\delta = 0$ otherwise. Thus,

$$\epsilon \iiint |e_{mn}|^2 \, dv = 1 \tag{2-30}$$

is the electric stored energy in the mn^{th} mode. In a closed cavity, the time-average electric and magnetic energies are equal. Therefore, normalization of the $\bar{e}_{mn}$ vectors automatically normalizes the corresponding $\bar{h}_{mn}$ vectors.

When the cavity begins to radiate real and reactive power out the radiating walls, several differences are noted:

1. The time-average electric and magnetic energies are no longer equal.
2. The eigenvalues are no longer necessarily real or discrete.
3. Energy is cross-coupled between discrete modes.
4. Only a finite number of discrete eigenfunctions exist.
5. In addition to these discrete eigenfunctions, there will be added a continuously varying eigenfunction with a continuous range of eigenvalues.

The electric field $E_z(x,y)$ interior to a probe-fed cavity satisfies the inhomogeneous differential equation:

$$\frac{\partial^2 E_z}{\partial x^2} + \frac{\partial^2 E_z}{\partial y^2} + k^2 E_z = j\omega\mu_o I_{in} \delta(x - x_o) \delta(y - y_o) \tag{2-31}$$

along with the impedance-type boundary conditions:

$$\frac{\partial E_z}{\partial n} + \alpha E_z = 0 \qquad \text{(on radiating walls)} \tag{2-32}$$

The partial derivative $\partial/\partial n$ is with respect to an outward-directed coordinate and α is dependent on the impedance of the walls. The complete set of functions required to represent any arbitrary E_z consists now of both the discrete modes $\bar{e}_{mn}(x,y)$ plus a continuous spectrum $\bar{\underset{\sim}{e}}(x,y;k_x,k_y)$. Thus the solution is given by

$$E_z(x,y) = -j\omega\mu_o I_{in} \iint_{\text{cavity}} G(x,y;x',y')\,\delta(x'-x_o)\,\delta(y'-y_o)\,dx'\,dy' \tag{2-33}$$

or

$$E_z(x,y) = -j\omega\mu_o I_{in}\, G(x,y;x_o,y_o) \tag{2-34}$$

where G is the Green's function which satisfies the relation

$$\frac{1}{2\pi j}\iint_{C_1,C_2} G(x,y|x_o,y_o;k_x,k_y)\,dk_x\,dk_y = \sum_{m=0}^{M}\sum_{n=0}^{N} e_{mn}(x,y)e_{mn}(x_o,y_o) + \iint \underset{\sim}{e}(x,y;k_x,k_y)\,\underset{\sim}{e}(x_o,y_o;k_x,k_y)\,dk_x\,dk_y \tag{2-35}$$

where the contour over k_y is determined by that over k_x according to the separation condition $k_y = (k^2 - k_x^2)^{1/2}$. The contour C_1 (or C_2) is taken around all singularities of the Green's function. Equations (2-31) through (2-35) are developed in the context of a rectangular microstrip antenna; a similar development for circular patches can be carried out using cylindrical coordinates. For both of these cases, the two-dimensional Green's function is separable into a product of one-dimensional

Green's functions. However, for arbitrary microstrip patch shapes, this is not in general true.

Returning to (2-35), it is noted that for closed cavities, the complete set of mode vectors is represented by only the discrete sum. For open radiating cavities (waveguides) which satisfy a radiation condition at the walls, the complete set of modes is the continuous eigenfunction seen in the contour integral on the right-hand side of (2-35). For the most general case, however, both discrete modes and continuous modes will be present, along with discrete and continuous eigenvalues.

Practical microstrip antennas usually have impedance bandwidths which are small and of the order of 1%. This indicates a high-Q condition and that the interior fields are dominated by the discrete modes. However, the continuous spectrum $\underset{\sim}{e}(x,y;k_x,k_y)$ cannot be ignored since it is closely related to the radition admittance of the walls.

These impedance considerations will be applied to specific microstrip patch shapes in Section 4 of this report.

2.3.6 Impedance Bandwidth

The impedance bandwidth is given by

$$\Delta f = \frac{f_r}{Q} \tag{2-36}$$

where f_r is the resonant frequency and the total Q is given by

$$Q = \omega \frac{W}{\text{Re } P_{in}} \tag{2-37}$$

with $W = W_e + W_m$ being the total stored energy both in the cavity interior and the near-field region of the antenna. The real input power is either dissipated by the conductors or dielectric or is radiated as real power through the radiating walls. Thus

$$Q = \frac{1}{Q_r} + \frac{1}{Q_c} + \frac{1}{Q_d} \tag{2-38}$$

where

$$Q_r = \omega \frac{W}{\text{Re } P_r} \tag{2-39}$$

$$Q_c = \omega \frac{W}{\text{Re } Z_c \iint |H_{tan}|^2 \, ds} \tag{2-40}$$

$$Q_d = \frac{W}{\varepsilon'' \iiint |E^i|^2 \, dv} \tag{2-41}$$

The total stored energy (both in the cavity and in the radiated field) can by computed by

$$W = \frac{1}{2} \iiint (\varepsilon |E^i|^2 + \mu |H^i|^2) \, dv + \frac{2\pi}{\omega} \text{Im } P_r \tag{2-42}$$

where P_r is given by (2-20).

2.3.7 Antenna Efficiency

The antenna efficiency is the ratio of real radiated power to real input power, i.e.

$$\eta = \frac{\text{Re } P_r}{\text{Re } P_{in}} \tag{2-43}$$

Thus,

$$\eta = Q/Q_r \tag{2-44}$$

Also, using (2-20), (2-43) can be written as

$$\eta = \frac{R_w (R_{in}^2 + X_{in}^2)}{R_{in} (R_w^2 + X_w^2)} \times \frac{1}{t |V_{in}|^2} \times \int |V_\ell|^2 \, d\ell \tag{2-45}$$

where $V_\ell = -E_z \, t$ evaluated at the radiating wall, and where $Z_w = R_w + jX_w$ is the wall impedance, assumed independent of perimeter position.

2.4 Formalism for the Exterior Problem

The two objectives of the exterior problem are to find the far-field radiation pattern (including gain and polarization) and to describe the near-field coupling behavior of the microstrip patch. The exterior fields may be found from the equivalence principle if the tangential fields in the radiating walls of the cavity and/or the tangential magnetic fields on the exterior conductors are known; the equivalent magnetic surface currents in the gap are given by

$$\overline{M}_s = \overline{E}_z \times \hat{n} \tag{2-46}$$

where E_z is evaluated in the gap (radiating wall) and $\hat{n}$ is a unit vector which is normal outward from the gap. The equivalent electric surface currents on the top of the patch and on the ground plane are given by

$$\overline{J}_s = \hat{z} \times \overline{H} \tag{2-47}$$

where $\overline{H}$ is evaluated on either the patch or the ground plane.

The exterior fields are then found by the formalism

$$\overline{E}^e = \frac{1}{j\omega\varepsilon}(\nabla\times\nabla\times\overline{A} - \overline{J}) - \nabla\times\overline{F} \tag{2-48}$$

$$\overline{H}^e = \frac{1}{j\omega\varepsilon}(\nabla\times\nabla\times\overline{F} - \overline{M}) + \nabla\times\overline{A} \tag{2-49}$$

where $\overline{A}$ is the vector magnetic potential given by

$$\overline{A} = \frac{1}{4\pi} \int\int \frac{\overline{J}_s(\overline{r}')\ e^{-jk|\overline{r} - \overline{r}'|}}{|\overline{r} - \overline{r}'|}\, ds' \tag{2-50}$$

and $\overline{F}$ is the vector electric potential given by

$$\overline{F} = \frac{1}{4\pi} \int\int \frac{\overline{M}_s(\overline{r}')\ e^{-jk|\overline{r} - \overline{r}'|}}{|\overline{r} - \overline{r}'|}\, ds' \tag{2-51}$$

When the exact current densities are known and if the conductivities of the patch and ground plane are infinite, the fields satisfy the boundary conditions:

$$\left.\begin{aligned} \hat{z} \times \overline{E}^e &= 0 \\ \hat{z} \times \overline{H}^e &= \overline{J}_s \end{aligned}\right\} \quad \text{on patch and on ground plane} \tag{2-52}$$

$$\left.\begin{aligned} \hat{n} \times \overline{H}^e &= \hat{n} \times \overline{H}^i \\ \overline{E}^e \times \hat{n} &= \overline{M}_s \end{aligned}\right\} \quad \text{on radiating wall} \tag{2-53}$$

$$\lim_{r\to\infty} |rE^e| \quad \text{is finite}$$

$$\lim_{r\to\infty} |rH^e| \quad \text{is finite} \qquad \text{radiation condition} \tag{2-54}$$

The formalism of (2-48) - (2-51) requires a knowledge of <u>both</u> $\overline{J}_s$ and $\overline{M}_s$, as shown in Fig. 2.4a. The fields can also be found from $\overline{J}_s$ alone (Fig. 2.4c) or $\overline{M}_s$ alone (Fig. 2.4b).

For the $\overline{M}_s$ formulation, a perfect conductor is placed over the surface bounding the interior region. Since a tangential $\overline{J}_s$ over a perfect conductor produces a zero net field in the exterior region, the field is calculated from $\overline{M}_s$ alone in the presence of the conductor. The exterior field is then found as

$$\overline{E}^e(r) = -\nabla\times \int_{\substack{\text{rad.}\\ \text{wall}}} \int \frac{E_z(\overline{r}')(\hat{z}\times\hat{n})}{4\pi\,|\overline{r}-\overline{r}'|}\, e^{-jk|\overline{r}-\overline{r}'|}\, ds' \tag{2-50}$$

subject to the boundary condition

$$\hat{n} \times \overline{E}^e = 0 \qquad \text{on perfect conductors} \tag{2-51}$$

This is an awkward equation to solve because of blockage introduced by the conducting step jump.

In Fig. 2.5, additional equivalent sources are shown which produce the same field in the half-space above the plane of the patch and a null field below this plane. Fig. 2.5c shows an equivalence which takes advantage of image theory; in this case, the perfect conductor is removed and

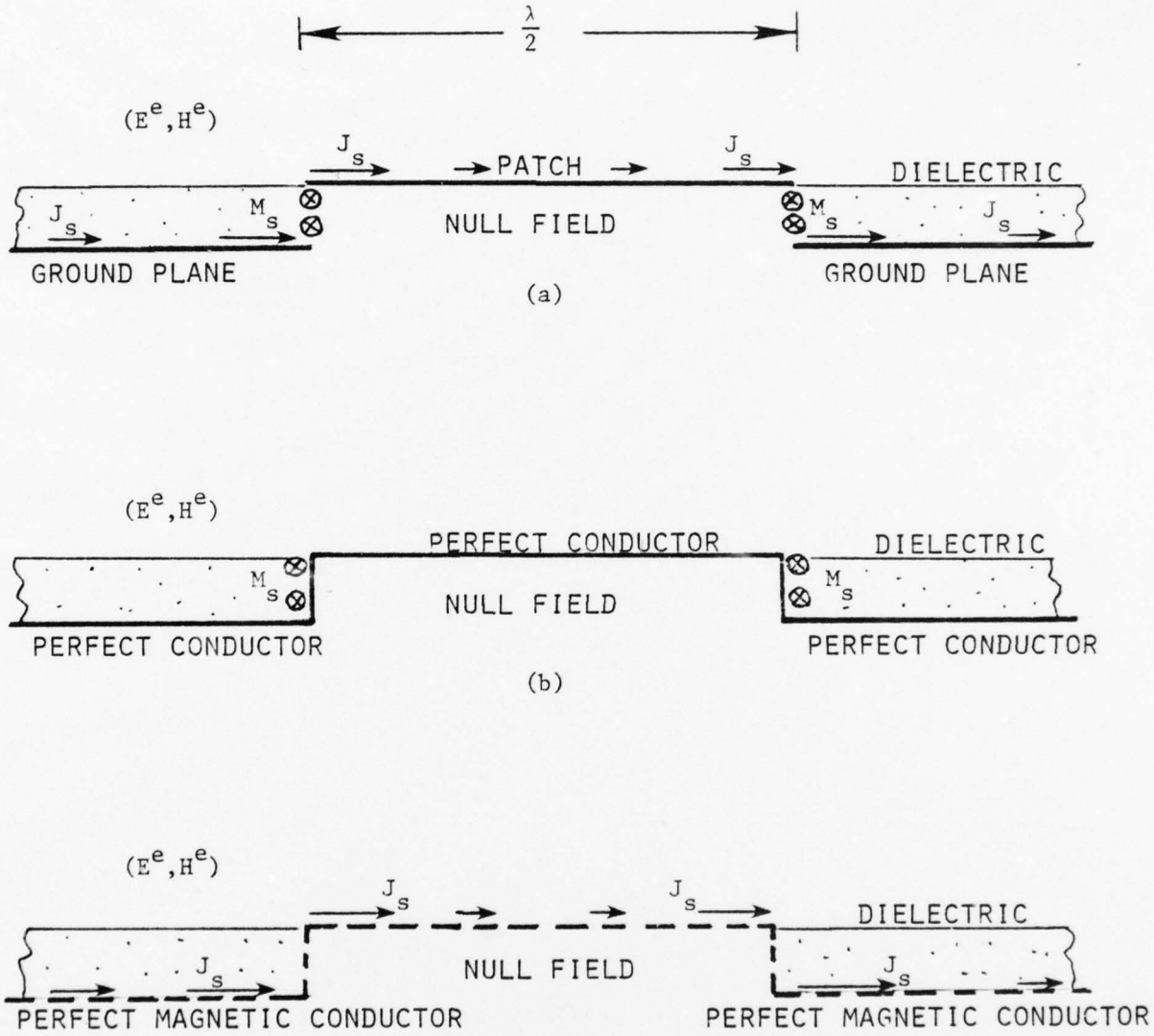

Fig. 2.4. Three source formulations which produce the same exterior field. (a) J_s and M_s; (b) M_s alone plus perfect electric conductor; (c) J_s along plus perfect magnetic conductor. The exterior region includes the half-space above the patch as well as the region interior to the dielectric.

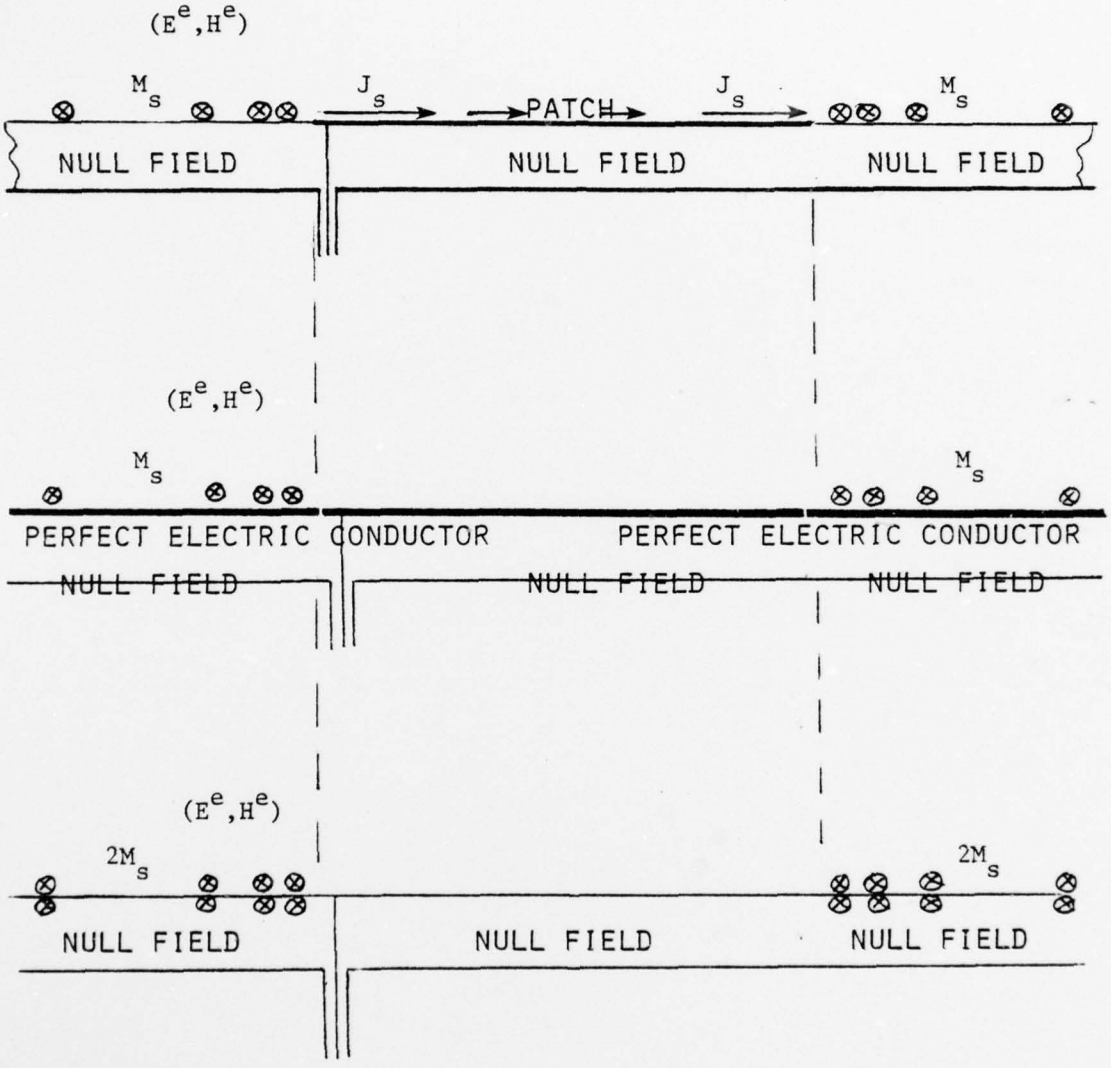

Fig. 2.5. Three additional equivalent source formulations which produce the same field above the plane of the patch. (a) J_s and M_s; (b) M_s alone plus perfect conductor; (c) $2M_s$ alone (magnetic image).

the magnetic surface current density is doubled. Thus,

$$\overline{E}^e(r) = -\nabla\times \int\int_{S-S_o} \frac{(\overline{E}_{ap} \times \hat{z})\, e^{-jk|\overline{r} - \overline{r}'|}}{2\pi\, |\overline{r} - \overline{r}'|}\, ds' \qquad (2\text{-}52)$$

where the aperture plane is S and the portion of S which represents the patch is S_o.

Finding an exact relationship between the tangential electric fields in the aperture plane and those in the radiating wall of the cavity is not a simple task, as is illustrated in Fig. 2.6 where the electric field lines have been determined by graphical field mapping procedures for the d.c. case. In the immediate vicinity of the edge, these d.c. field lines will be similar to those of a radiating cavity. Due to the dielectric/air discontinuity, the field lines will refract according to Snell's Law and the electric field in air will be larger than that of the same line in the dielectric. Furthermore, the tangential component of $\overline{E}_{ap}$ is appreciable only very near the edge of the patch.

An approximate relation between the field $\hat{z}\, E_{rw}$ in the radiating wall of the cavity and the tangential field $\overline{E}_{ap}$ in the aperture plane may be found by first assuming that the region of the aperture plane over which effective magnetic currents exist is a thin strip of width w extending from the edge of the patch outward. Over this region, z-components of $\overline{E}_{ap}$ tend to cancel, leaving only a tangential component. Let ℓ_d be the length of a field line from the ground plane to the dielectric surface and let ℓ_a be the remaining length of the line from the dielectric to the patch. Then assuming the patch to be an equipotential surface,

$$V_p = -(E_d\, \ell_d + E_a\, \ell_a) \qquad (2\text{-}53)$$

where E_d is the electric field in the dielectric and E_a is the electric field in air, both evaluated on the same line. Furthermore, the electric flux density is constant over any one line so that

$$D = \varepsilon_o \varepsilon_r E_d = \varepsilon_o E_a \qquad (2\text{-}54)$$

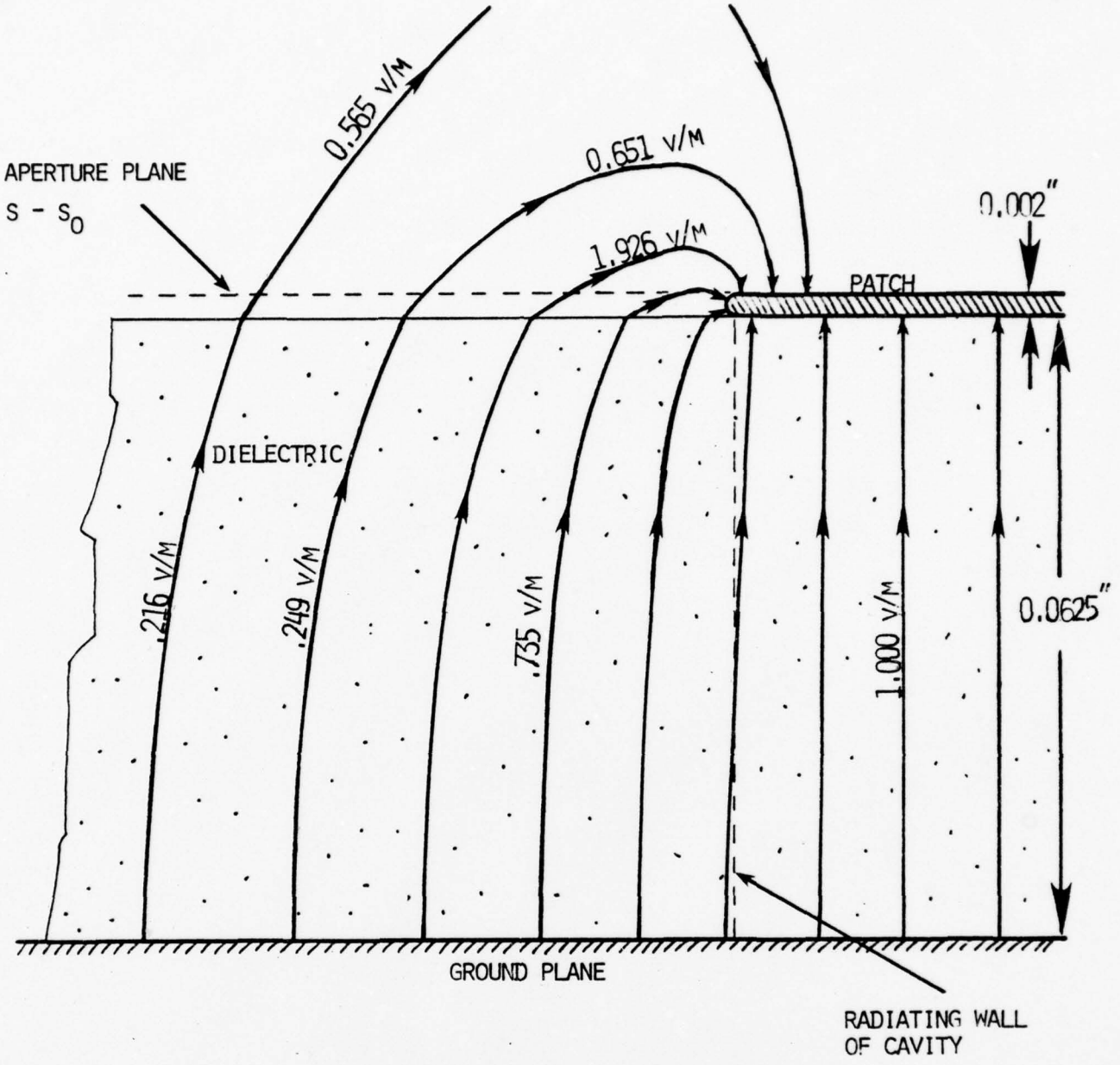

Fig. 2.6. Illustrating the d.c. fringing field distribution for the edge of a microstrip patch with $\varepsilon_r = 2.6$, t = 0.0625" and a patch conductor thickness of 0.002".

where ε_r is the dielectric constant of the patch. Combining (2-54) and (2-53),

$$E_a = V_p \left(\frac{\ell_d}{\varepsilon_r} + \ell_a \right)^{-1} \tag{2-55}$$

At the edge of the patch, ℓ_a is zero and E_a is entirely tangential so that

$$E_{ap}(\text{edge}) = \varepsilon_r \frac{V_p}{\ell_d} = \varepsilon_r E_{rw} \tag{2-56}$$

This is the maximum tangential field in the aperture plane. The effective tangential field is less than this. For an aperture plane of effective strip width w = t, the tangential field at the outer edge of the strip is essentially zero*, so that the effective aperture tangential field is approximately half that given by (2-56):

$$\overline{E}_{ap} = -\hat{n}_p \frac{\varepsilon_r}{2} E_{rw} \qquad \text{(over aperture strip of width t)} \tag{2-57}$$

where $\hat{n}_p$ is a unit vector lying in the aperture plane and extending outward from the patch edge.

The far fields may now be computed by letting $|\overline{r} - \overline{r}'| = r$ in the denominator of (2-52) and by letting $|\overline{r} - \overline{r}'| = r - r' \cos \phi'$ in the exponential of (2-52) ; these coordinates are shown in Fig. 2.7. Then, the far electric fields are given by

$$\overline{E}(\theta,\phi) = \hat{\theta}\, E_\theta(\theta,\phi) + \hat{\phi}\, E_\phi(\theta,\phi) \tag{2-58}$$

where

$$E_\theta = -jk\, F_\phi \qquad ; \qquad E_\phi = jk\, F_\theta \tag{2-59}$$

---

*This is based on field maps for the static case and assumes that ε_r is less than about 6.

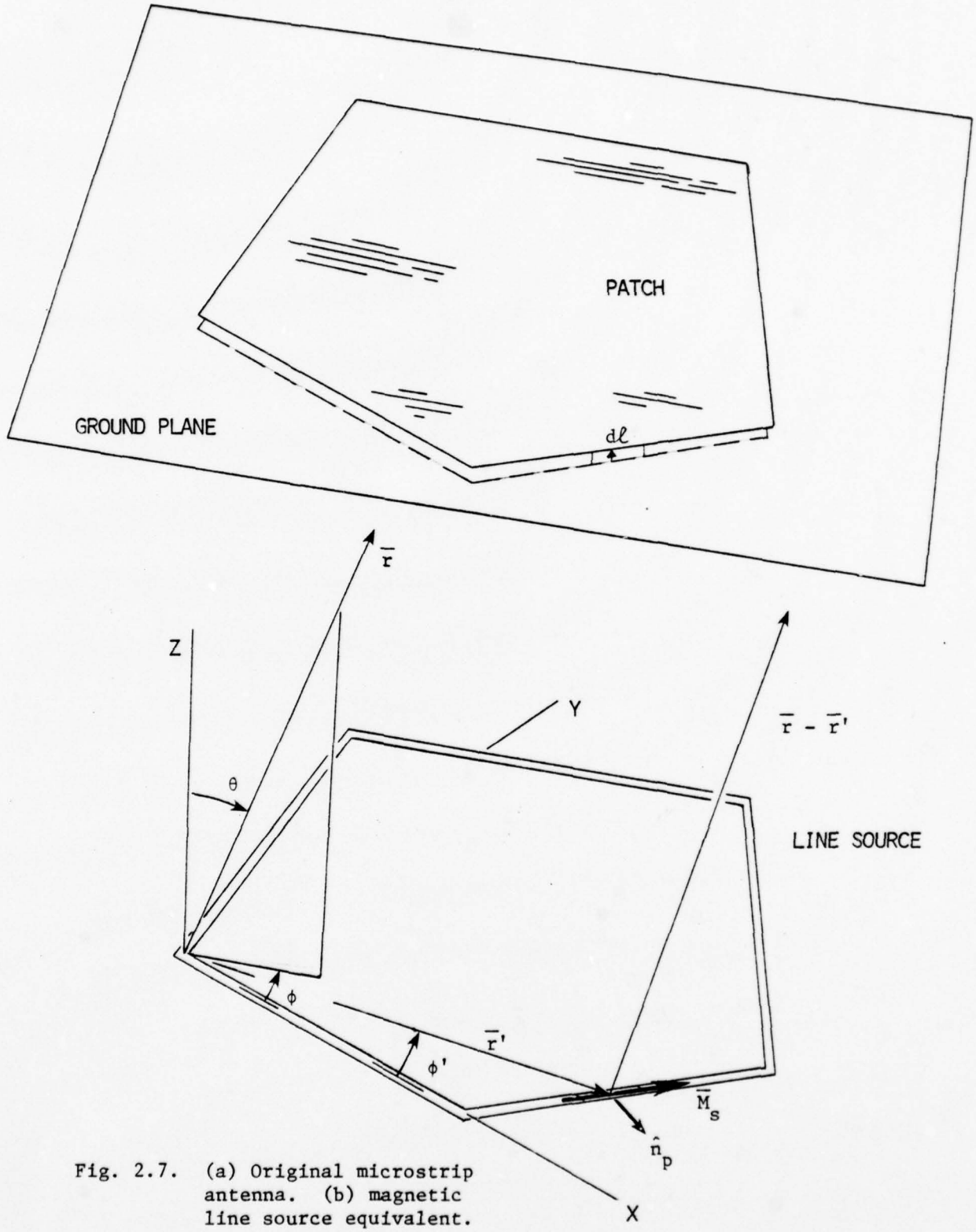

Fig. 2.7. (a) Original microstrip antenna. (b) magnetic line source equivalent.

$$\bar{F} = \frac{e^{-jkr}}{2\pi r}\, t \int_{\text{perimeter}} \bar{M}_s(r',\phi')\, e^{jkr'\cos\phi'}\, d\ell' \qquad (2\text{-}60)$$

and where

$$\bar{M}_s \simeq (\hat{z} \times \hat{n}_p)\, \frac{\varepsilon_r}{2}\, E_{rw} \qquad (2\text{-}61)$$

It is emphasized that the magnetic surface current density in (2-61) is approximate; more work is required to obtain better relationships between the magnetic surface current density in the aperture plane and the z-directed field in the radiating wall of the cavity.

The corresponding far-zone magnetic fields are given by

$$H_\phi = \frac{E_\theta}{Z_o} \quad ; \quad H_\theta = -\frac{E_\phi}{Z_o} \qquad (2\text{-}62)$$

where $Z_o = 376\ \Omega$ is the free-space impedance.

Finally, it is observed that the real radiated power obtained by integrating the real part of the power density around the radiating wall of the cavity (eqn. 2-20) will be equal to the real radiated power obtained by integrating the Poynting vector over a far-field hemisphere minus the real power appearing in the surface wave traveling in the dielectric.

3.0 NUMERICAL TECHNIQUES FOR THE INTERIOR PROBLEM

It was proposed originally that the most efficient numerical method for solving the interior problem was the Unimoment-Monte Carlo Method [Coffey, 1976; Coffey & Carver, 1977] implemented on a medium-size hybrid computer. This technique was tested during the period 10 April, 1978 - 30 June, 1978 and was found to perform quite well on simple boundary value problems [Coffey & Carver, 1978]. However, it has been decided to abandon this unique method in favor of more traditional techniques because (1) the hybrid computer at NMSU was being repaired during the period 30 June, 1978 - 15 September, 1978 and was unavailable for research, and (2) one of the principal investigators (ELC) terminated employment with NMSU and a more traditional technique seemed to be required which would not depend on his expertise in the hybrid computer/Unimoment-Monte Carlo area. During the period 15 Sept. to 1 Nov., 1978 a search for alternative computational methods was undertaken with the goal of finding a method which would allow the goals of this study to be fulfilled while overcoming the difficulties listed above. Three techniques were considered:

1. The method of moments [Harrington, 1968], which would be used to calculate electric currents induced on the surface of the patch, from which the far fields could be found using the magnetic vector potential method.
2. The finite difference method, in which differential equations are approximated by difference equations. These are solved for the electric field at the perimeter of the patch, and the far field may be obtained by using the electric vector potential.
3. The finite element method [Strang & Fix, 1973], a variational method in which the minimization process automatically seeks out the solution which is "closest" to the true analytical solution. The far field is calculated by the same method as in (2).

Of these three, the finite element method was chosen mainly because of the generality of the technique (many different patch shapes may be

considered) and the mathematical integrity inherent in the method (unlike the method of moments, which only may converge - and sometimes to the wrong solution).

3.1 Mathematical Development and Numerical Implementation

Maxwell's two curl equations may be combined to form the Helmholtz equation (with zero charge density):

$$\nabla^2\overline{E} + k_o^2 \overline{E} = j\omega\mu\overline{J} \tag{3-1}$$

where $k_o^2 = 2\pi/\lambda_o = \omega\sqrt{\mu_o\varepsilon_o}$ in free space. The Helmholtz equation itself does not couple together the rectangular components of $\overline{E}$, i.e.

$$\begin{aligned}
\nabla^2 E_x + k_o^2 E_x &= j\omega\mu J_x \\
\nabla^2 E_y + k_o^2 E_y &= j\omega\mu J_y \\
\nabla^2 E_z + k_o^2 E_z &= j\omega\mu J_z
\end{aligned} \tag{3-2}$$

However, the boundary conditions may couple the rectangular components. For example the radiation condition requires that the radially directed component of $\overline{E}$ (E_r) vanish properly at infinity. Since E_r is composed of $(\sin\theta\cos\phi)E_x + (\sin\theta\sin\phi)E_y + \cos\theta E_z$, the components of $\overline{E}$ are coupled through the radiation condition. If a vector problem is to be avoided, then the boundary conditions specified in the problem must contain only one rectangular component of $\overline{E}$. The report by Lo, et. al. [1977] assumed that $\partial E_z/\partial n = 0$ (open circuit at radiating edges, or Neumann boundary value problem) and obtained fairly good results for a variety of patch shapes. This present work assumes an impedance boundary condition on E_z (Robbin boundary value problem):

$$\frac{\partial E_z}{\partial n} + \alpha E_z = 0 \tag{3-3}$$

Finally, it is assumed that E_z does not vary with z. This is a fairly safe assumption for the lower-order modes, but is risky for higher-order modes. By making this assumption, it is possible to reduce the original three-dimensional problem to a two-dimensional problem

of a partial differential equation (PDE) plus boundary conditions (BC):

$$\frac{\partial^2 u}{\partial x^2} + \frac{\partial^2 u}{\partial y^2} + k^2 u = j\omega\mu J_z \qquad \text{(PDE)}$$

$$\frac{\partial u}{\partial n} + \alpha\, u = 0 \qquad \text{(BC on patch perimeter)} \tag{3-4}$$

where for simplicity, the variable u has been substituted for E_z.

The equivalent variational formulation of (3-4) is to minimize the functional [Strang & Fix, pp. 70-71, 1973]:

$$I(v) = \int\int_{\text{interior}} (v_x^2 + v_y^2 - k^2 v^2 + 2j\omega\mu J_z v)\, dA + \oint_{\text{perimeter}} \alpha\, v^2\, d\ell \tag{3-5}$$

for all permissible functions v(x,y). The particular function $v^*(x,y)$ which minimizes (3-5) is the "best" solution to (3-4). Details of this development may be found in Strang & Fix [1973].

Three tasks remain in order to solve the problem. First, a set of "permissible" v functions must be determined. The goal is to choose trial functions $\psi_1, \psi_2, \ldots \psi_N$, and from among their linear combinations $\sum_j q_j \psi_j$ to find the one which minimizes (3-5). In theory, there always exists a set of trial functions which is complete, but it may be difficult or even impossible to compute with them. The underlying idea of the finite element method is this: divide the patch into smaller pieces such as triangles or rectangles. Then within each piece the trial functions are given a simple form: all trial functions are zero except one which is usually a polynomial. Boundary (continuity) conditions are imposed locally, along the edge of a triangle or rectangle rather than globally as in the classical Ritz method. The approximation of the solution may be refined, if necessary, not by including more complex trial functions, but by further subdivision of the patch. A digital computer is ideally suited to this task.

Second, the integrals in (3-5) must be computed for each trial function in terms of still-to-be-determined parameters. For the case at hand these

parameters are the nodes of the subdivisions, but for other physical problems, the parameters may represent other quantities. The integrals in (3-5) are particularly easy to compute since each ψ_j is zero except within one subdivision.

Finally, the problem must be put into a form that can be solved by a computer, as hand calculation is too tedious and time-consuming. This form is given symbolically by [Strang & Fix, 1973, p. 32]:

$$\underline{Q}^T \underline{K} \underline{Q} - 2 \underline{Q}^T \underline{F} = 0 \tag{3-6}$$

where $\underline{Q}$ is the column matrix of coefficients (the solution), $\underline{K}$ is the finite element matrix arising from (3-5), and $\underline{F}$ is the forcing function column matrix, the linear (in v) term of (3-5). Equation (3-6) has a minimum for

$$\underline{K} \underline{Q} = \underline{F} \tag{3-7}$$

and (3-7) is the matrix problem to be solved.

The eigenvalue problem (with the eigenvalue $\Lambda = -k^2$) may be set up as

$$\underline{K}_1 \underline{Q} = \Lambda \underline{K}_2 \underline{Q} \tag{3-8}$$

where $\underline{K}_1$ is obtained from

$$\int\int_{\text{interior}} (v_x^2 + v_y^2)\, dA + \oint_{\text{perimeter}} \alpha\, v^2\, d\ell \tag{3-9}$$

and $\underline{K}_2$ is obtained from

$$\int\int_{\text{interior}} v^2\, dA \tag{3-10}$$

Notice that the impedance boundary value α does play a role in the eigenvalue determination while the forcing term $j\omega\mu J_z$ does not. The eigenvalues and eigenvectors of (3-8) may be obtained by using standard subroutine libraries (SSP or IMSL for example - see list of references).

The calculation of the $\underline{K}_1$ and $\underline{K}_2$ matrices for a general polygonal

microstrip antenna has been implemented in the computer program MICRO, a listing of which can be obtained from the authors . The important inputs to this program are (1) the number of triangular subdivisions made to the original patch, (2) the numbers of the three nodes which define each triangle, (3) the total number of nodes, and (4) the x-y coordinates of each node. From this data, the program calculates the $\underline{K}_1$ and $\underline{K}_2$ matrices for the Neumann problem. If certain nodes are constrained to a field of zero (Dirichlet condition) these node numbers are also entered. The eigenvalues of the resulting generalized matrix problem are computed and checked by IMSL subroutine EIGZF and printed.

3.2 Numerical Difficulties Overcome or to be Overcome

3.2.1 Matrix Calculation for Irregular Polygon Patches

To utilize the full power of the finite element method, the computer programs written to implement the technique must be general enough to handle a variety of geometries. For regular geometries such as the rectangle, circle, etc., it is simple enough to devise computer programs that will automatically partition the regular region into appropriate subdivisions. On the other hand, for general polygonal microstrip antennas, such a program would be unwieldy at best and not general enough at worst. This is particularly important in the case of patch antennas because it is the unusual geometry that is often so interesting. For example, there is a five-sided polygon patch which can be excited at a single feed point to give right circular polarization, at a second point to give left circular polarization, and at a third point to given linear polarization [Weinschel, 1975]. To make the MICRO program as general as possible the so-called area method [Strang & Fix, 1973, pp. 90-97] was used rather than the node method more familiar to those who work with moment methods.

The area method works as follows. Each triangular subdivision area is taken, one at a time, and the three nodes which define the triangle are determined. The integrals in (3-5) are performed with these three unknown node values as parameters. The resultant expression is a quadratic and may be put into the form of (3-6) to determine what is called $\underline{K}_e$, the elemental $\underline{K}$ matrix. $\underline{K}_e$ is different for each area and contains at most nine non-zero entries. The sum of all $\underline{K}_e$ matrices is the $\underline{K}$ matrix of (3-6).

As an example, suppose one triangular area is bounded by nodes 1, 2, and 4. Then $\underline{K}_e$ has the form:

$$\underline{K}_e = \left[\begin{array}{cccc|c} x & x & 0 & x & \\ x & x & 0 & x & 0 \\ 0 & 0 & 0 & 0 & \\ x & x & 0 & x & \\ \hline & 0 & & & 0 \end{array}\right] \qquad (3\text{-}11)$$

In this matrix, only $k_{ij} \neq 0$ for i,j = 1,2, or 4. A detailed comparison between the area method and the nodal method is given in Strang & Fix [1973].

The second matrix computational difficulty was the evaluation of the integrals of (3-5). These integrals are of the form

$$P_{rs} = \iint_{\text{triangle}} x^r \, y^s \, dA \qquad (3\text{-}12)$$

Holand and Bell [1969] have given explicit formulas for these integrals, keeping the origin of the local (x,y) system at the centroid of the triangle. For $r + s < 6$,

$$P_{rs} = c_{r+s} \, A \, (X_1^r Y_1^s + X_2^r Y_2^s + X_3^r Y_3^s) \qquad (3\text{-}13)$$

where (X_1,Y_1), (X_2,Y_2), (X_3,Y_3) are the vertices of the triangle in the centroid system, A is the area, and $c_o = 1$, $c_1 = 0$, $c_2 = 1/12$, $c_3 = c_4 = 1/30$, $c_5 = 2/105$. Other possible coordinate systems and formulas are found in Strang and Fix [1973., pp. 90-96].

3.2.2 Impedance Boundary Conditions

The impedance boundary condition is easy to handle numerically once the impedance parameter $\alpha(x,y)$ of equation (3-4) has been determined theoretically. This is related to the wall admittance per unit length.

Computationally, terms are added to the $\underline{K}$ matrix corresponding to that portion of (3-5) containing α. If the patch antenna has been divided into sufficiently many sections then α may be assumed constant over any one section, and the integration is trivial. Otherwise the integration may be handled numerically.

One significant problem must be dealt with whenever α is imaginary or complex (indicating that energy is being radiated from the cavity walls): the $\underline{K}$ or $\underline{K}_1$ matrices become complex. For the radiation problem this presents no difficulty since complex arithmetic may be used in the matrix inversion routine. However, for the eigenvalue/eigenvector problem, only real arithmetic routines have been found. Hence, a conversion from an N x N complex problem to a 2N x 2N real problem must be performed. Mathematically, this is trivial but such an increase in matrix size may require over times as much computer time.

3.2.3 Eigenvalue/Eigenvector Computation

Up to this point all eigenvalues and/or eigenvector calculations have been made by using IMSL subroutine EIGZF. However, to increase the size of the problems now being solved or to include complex matrices in the subsequent work under this grant, a different approach must be taken. The most promising technique thus far found is called "subspace iteration." It is possible to compute the first p eigenvalues/vectors in about 8 iterations if the subspace dimension ℓ was

$$\ell = \min(2p, p+8) \tag{3-14}$$

Since only the lower few modes are of importance in microstrip antenna work (and the higher modes are just numerical garbage) this technique seems to be the most promising. Briefly, to solve $\underline{A}\,\underline{X} = \lambda\,\underline{M}\,\underline{X}$, start with an eigenvector guess of $\underline{X}_{n-1}$, which is a matrix with ℓ orthonormal columns. Solve $\underline{K}\,\underline{Y}_n = \underline{M}\,\underline{X}_{n-1}$. Then solve the eigenvalue problem

$$(\underline{Y}_n^T\,\underline{K}\,\underline{Y}_n)\,\underline{Q} = \nu\,(\underline{Y}_n^T\,\underline{M}\,\underline{Y}_n)\,\underline{Q} \tag{3-15}$$

The ν_i are the approximate eigenvalues and the new matrix $\underline{X}_n$ of approximate eigenvectors is formed by multiplying $\underline{Y}_n$ with the $\ell x \ell$ matrix of eigenvectors of (3-15). Since equation (3-15) is of only dimension ℓ, subroutine EIGZF

may be used efficiently here. For example, suppose the first four modes are needed in a microstrip problem. Then by (3-14), $\ell = 12$, and only about eight 12 x 12 eigenvalue problems need be solved.

3.2.4 Size of Matrices versus Core Memory

At PSL only about 140K bytes of computer storage are avilable for matrices $\underline{K}_1$ and $\underline{K}_2$. This limits the size of $\underline{K}_1$ and $\underline{K}_2$ to about 132 x 132 four-byte words. However, most of the entries in either matrix are zero. For example, in a regular triangular partition there are at most seven entries per row regardless of the size of the problem to be solved. To utilize more effectively the available storage area, a linked list sparse matrix routine has been written following the guidelines of Wexler [1978] and Zollenkopf and Reid [1971]. This routine has been tested for the simple case of the static Dirichlet problem within the rectangle. The test, while verifying the integrity of the program, also illustrates the tremendous savings in computer memory that can be obtained. For the test case, a ten-to-one reduction in memory was achieved.

One of the advantages of using a sparse matrix program is the ease with which the program may be combined with subspace iteration. Subspace iteration requires only $\ell x \ell$ matrices (see 3.2.3) where ℓ is small. Thus the $\underline{K}_1$ and $\underline{K}_2$ data may be kept in a linked list rather than in a full dense matrix, and the storage requirements may be kept to on the order of $\ell x \ell$.

As an example, consider the finite element solution of the rectangular interior problem for which one hundred (10 x 10) interior nodes have been specified. The lowest three modes are desired. Using traditional matrix techniques, two 100 x 100 matrices would have been needed to solve for the eigenvectors and eigenvalues of the problem, or about 80K bytes of memory. However, all but 460 entries in either matrix are zero. Sparse matrix techniques utilize algorithms in which none of the zero entries need be stored. Instead, two auxiliary tables are used. For the above example, less than 7.6 K bytes of matrix space plus 3.8 K bytes of table space would be required, a savings of 86%. (In addition, solution times are generally more rapid, offering further savings in computer resources.) The use of subspace iteration gives a great reduction in computer time

because only the lowest three modes are needed in this example. Using equation (3-14), $\ell = 11$. Hence, eight 11 x 11 eigen-problems need be solved versus one 100 x 100 eigen-problem. Since solution times vary at least on the order of N^2, this represents a savings of 90%. On the PSL IBM computer this represents a savings of 14 minutes for a 51 x 51 problem.

Finally, it should be noted that the method of moments generates in general full, dense matrices, and sparse matrix techniques cannot be used. This is because most moment method problems arise from integral equations whereas most finite element method problems arise from partial differential equations.

At this writing neither the sparse matrix routine nor the subspace iteration program have been implemented per se into the MICRO program.

3.3. Handling the Feedpoint

A microstrip antenna is usually fed in one of two ways: (1) coaxially from beneath the ground plane, or (2) on the edge of the patch by a microstrip transmission line. Each method of feeding may be handled within the framework of the present mathematics.

The coaxial feed may be modeled as a point current source at (x_o, y_o) [vide Sec. 2.3.5]:

$$J_z(x,y) = J_o \, \delta(x - x_o) \, \delta(y - y_o) \tag{3-16}$$

and may be treated as a forcing term in equations (3-4) and (3-5). The integrals for the F-matrix of (3-7) are simplified because of the Dirac delta functions. It has been assumed that J_z has no z-dependence due to the relatively small spacing (much less than a wavelength) between patch and ground plane on most microstrip antennas. This assumption may not be valid for feeds placed near an edge or horizontal metallic struction. In these cases, a more rigorous feedpoint attachment theory must be used [Newman, 1978].

The microstrip line feed may be handled via the boundary conditions. Over the width of the line, assume that

$$E_z(x,y) = E_o \tag{3-17}$$

and elsewhere use the impedance boundary condition discussed in Sec. 3.1. The effect of (3-17) is to constrain one or more unknowns to the value E_o; this has been discussed previously in Sec. 2.3.5. These node values are then removed from the $\underline{K}$ matrices and transferred to the $\underline{F}$ matrix as equivalent constants (knowns). While this formulation requires that the boundary conditions be mixed (a rather intractable theoretical problem), mixed boundary conditions are not at all difficult to handle numerically.

4.0 NUMERICAL RESULTS

4.1 The Rectangular Patch

4.1.1 Closed Cavity Formulation (Neumann Boundary Condition)

Consider a rectangular microstrip cavity of length a and width b, as shown in Fig. 4.1. If there is no radiation out the side walls, the H_x component of the magnetic field will be zero on the y = 0 and y = b walls; the H_y components of the magnetic field will be zero on the x = 0 and x = a walls. The mode vectors (c.f. Sec. 2.3.5) are TM to z and for this Neumann boundary condition are given by

$$\bar{e}_{mn} = \hat{z} \frac{\chi_{mn}}{\sqrt{\varepsilon abt}} \cos \frac{m\pi y}{b} \cos \frac{n\pi x}{a} \tag{4-1}$$

$$\bar{h}_{mn} = \frac{1}{j\omega\mu} \frac{\chi_{mn}}{\sqrt{\varepsilon abt}} \left(\hat{x} \frac{m\pi}{b} \sin \frac{m\pi y}{b} \cos \frac{n\pi x}{a} - \hat{y} \frac{n\pi}{b} \cos \frac{n\pi y}{b} \sin \frac{n\pi x}{a} \right) \tag{4-2}$$

where

$$\chi_{mn} = \begin{cases} 2 & \text{if } m \neq 0 \text{ and } n \neq 0 \\ \sqrt{2} & \text{if } m = 0 \text{ or } n = 0 \end{cases} \tag{4-3}$$

which satisfies the orthonormality condition (2-29). The corresponding resonant wavenumbers k_{mn} are given by

$$k_{mn} = \sqrt{(m\pi/b)^2 + (n\pi/a)^2} \tag{4-4}$$

from which the resonant frequencies may be obtained by

$$f_{mn} = \frac{k_{mn}}{2\pi\sqrt{\mu\varepsilon}} \tag{4-5}$$

The magnetic current distribution at the four edges is computed from (c.f. eqn. 2-46):

$$\bar{M}_s = \hat{z} E_z \times \hat{n} \tag{4-6}$$

where E_z is the z-directed electric field at the radiating wall.

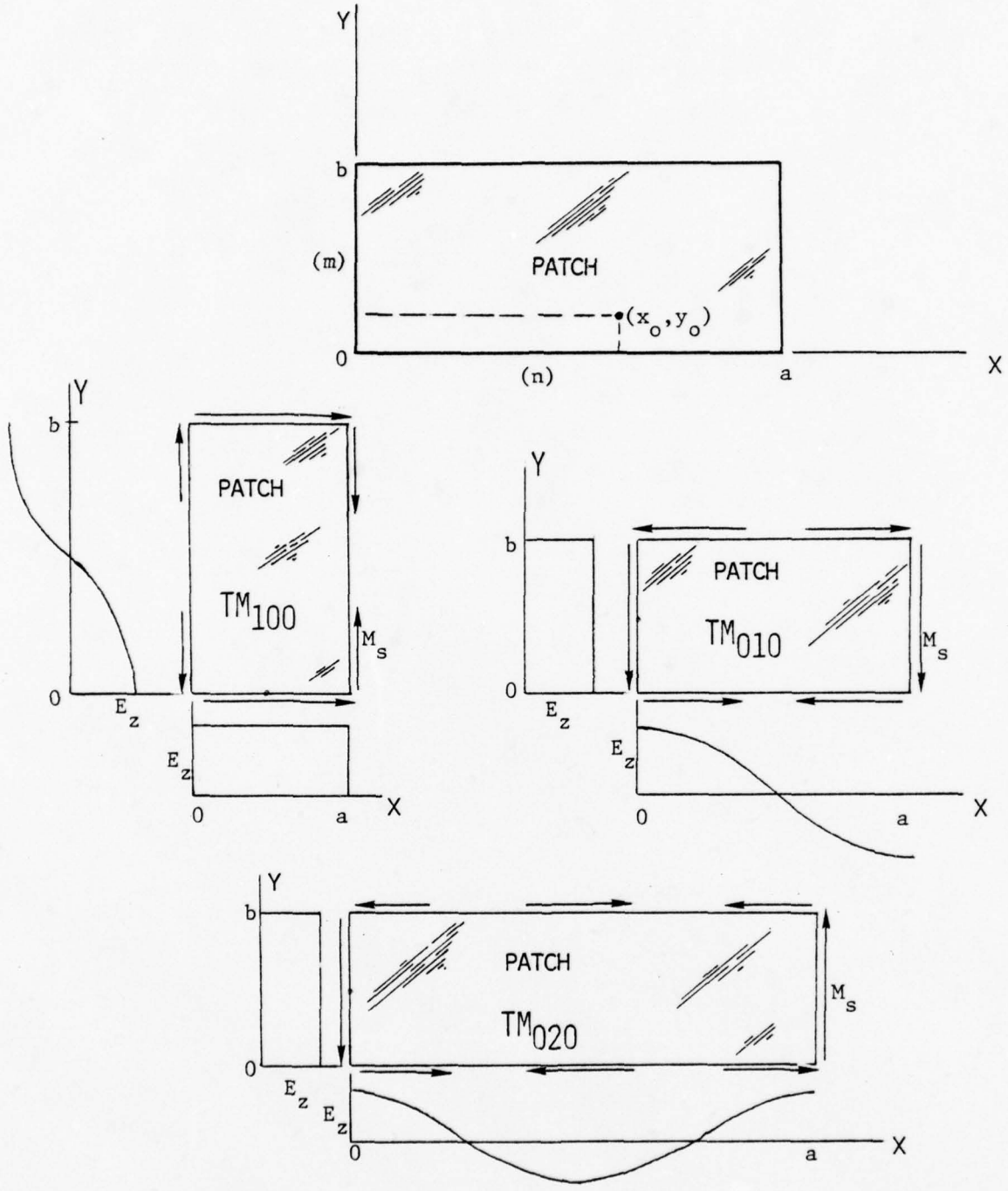

Fig. 4.1. Rectangular microstrip patch geometry showing electric fields and magnetic surface current distributions in walls for TM_{100}, TM_{010} and TM_{020} modes.

The resonant wavenumber k_{mn} may also be computed numerically, using the finite element method outlined in Section 3 of this report. To illustrate the comparison, consider a rectangular microstrip cavity with a = 10 cm and b = 20 cm; the interior dielectric is assumed to be air. Table 4-1 compares the resonant frequencies calculated using (4-5) to that computed from the method of finite elements using 100 square subdivisions. Two points are noted:

1. The resonant frequencies computed by finite elements are greater than the true values.
2. As the mode number becomes higher, the error becomes greater.

Table 4-1

Comparison of Computed and Theoretical Resonant Frequencies for Rectangular Microstrip Cavity with b = 2a = 20 cm.

Mode Number (m,n)	Resonant Frequency	
	True	Finite Elements Approx.
(0,0)	0	0
(1,0)	750.00 MHz	750.48 MHz
(0,1)	1500.00	1502.26
(2,0)	1500.00	1503.76
(1,1)	1677.05	1720.83
(2,1)	2121.32	2211.62
(0,2)	3000.00	3268.77

Both phenomena are characteristic of the finite elements method. However, for the microstrip antenna problem, neither is of concern because (1) sufficient subdivisions can be taken to insure that the computed resonant frequency is precise enough [Strang & Fix, 1973, Ch. 2] and (2) only the first three or four modes are of practical interest.

Since there is no radiation, the mode vectors (4-1) form a complete orthonormal set of discrete eigenfunctions (c.f. Sec. 2.3.5) which can be used to represent any arbitrary interior electric field, i.e.

$$\bar{E}_z = \sum_{m=0}^{\infty} \sum_{n=0}^{\infty} A_{mn} \bar{e}_{mn} \tag{4-7}$$

This double Fourier series has coefficients which may be found using the orthonormality property of the modal vectors; since this is a straightforward exercise in mathematical physics, only the result will be given. Assuming the cavity is fed by a z-directed filamentary current located at (x_o, y_o), the total interior electric field is given by

$$\bar{E}^i = \sum_{m,n} \frac{j\omega \bar{e}_{mn}}{\omega^2 - \omega_{mn}^2} \int_0^t I(z') \bar{e}_{mn}(x_o, y_o)\, dz' \tag{4-8}$$

If the cavity thickness is small, $I(z') = I_{in}$; furthermore, the input voltage is $V_{in} = -t\, E^i(x_o, y_o)$ so that the input impedance may be calculated from (2-28):

$$Z_{in} = \frac{V_{in}}{I_{in}} = -j\omega t^2 \sum_{m,n} \frac{e_{mn}^2(x_o, y_o)}{\omega^2 - \omega_{mn}^2} \tag{4-9}$$

Thus, for the rectangular cavity

$$Z_{in} = -j \frac{\omega t}{\varepsilon ab} \sum_{m=0}^{\infty} \sum_{n=0}^{\infty} \chi_{mn}^2 \frac{\cos^2 \frac{m\pi y_o}{b} \cos^2 \frac{n\pi x_o}{a}}{\omega^2 - \omega_{mn}^2} \tag{4-10}$$

The input impedance is purely reactive since no allowance for dissipated or real radiated power has yet been made. This will be considered in the next section.

It should be remarked that the shape and polarization of the far-field pattern can be fairly accurately predicted using only the magnetic line source model, i.e. eqns. (2-58) through (2-61), with magnetic surface currents computed from (4-6) and (4-1). This simple approach works well for predicting the pattern shape for discrete modes, as has been pointed out by Lo, et. al. [1977].

4.1.2 Radiating Cavity Formulation (Impedance Boundary Condition)

Since the microstrip antenna cavity radiates real and reactive power, the interior fields must satisfy an impedance-type boundary condition at the radiating walls. If the wall admittance is purely susceptive, then the eigenvalues k_x (similar to $n\pi/a$ for the discrete case) and k_y (similar to $m\pi/b$) will still be real-valued and discrete. However, for the radiative condition, the wall admittance is complex. It may be shown that the eigenvalues are given by the coupled transcendental equations:

$$\tan k_x a = \frac{2 k_x \alpha_x}{k_x^2 - \alpha_x^2} \tag{4-11}$$

$$\tan k_y b = \frac{2 k_y \alpha_y}{k_y^2 - \alpha_y^2} \tag{4-12}$$

where

$$k^2 = \omega^2 \mu\varepsilon = k_x^2 + k_y^2 \tag{4-13}$$

and

$$\alpha_x = j \frac{2\pi Z_o}{\lambda_o} Y_{wx} \frac{t}{b} \tag{4-14}$$

$$\alpha_y = j \frac{2\pi Z_o}{\lambda_o} Y_{wy} \frac{t}{a} \tag{4-15}$$

with Y_w being the wall admittance taken on the appropriate wall; $Z_o = 376\ \Omega$ and λ_o is the free-space wavelength.

In the dominant TM_{100} mode, effectively only the y = 0 and y = b walls radiate; furthermore, the electric field in the radiating walls is essentially independent of x so that the wall conductance may be approximated by that of a parallel-plate TEM waveguide opening onto a large ground plane; the resulting conductance is given by [Harrington, 1961, p. 183]:

$$G_w = \frac{\pi}{376} [1 - 1.645(t/\lambda_o)^2][a/\lambda_o] \quad (\mho) \tag{4-16}$$

For electrically small substrate thicknesses, this becomes

$$G_w = 0.00836\ (a/\lambda_o) \qquad (\mho) \tag{4-17}$$

This is plotted in Fig. 4.2 along with the conductance of a slot antenna radiating into half-space (Derneryd, 1976); it is seen that the conductance computed from (4-17) is roughly double that used by Derneryd for a slot antenna.

The wall susceptance may be computed from an expression for the capacitance of an open microstrip circuit [Hammerstad, 1975; Derneryd, 1976] and may be written in the convenient form

$$B_w = 0.01668 \frac{\Delta\ell}{t} \frac{a}{\lambda_o} \varepsilon_e \qquad (\mho) \tag{4-18}$$

where

$$\frac{\Delta\ell}{t} = 0.412 \left[\frac{\varepsilon_e + .300}{\varepsilon_e - .258}\right]\left[\frac{\frac{a}{t} + .262}{\frac{a}{t} + .813}\right] \tag{4-19}$$

and where ε_e is the effective dielectric constant given by [Schneider, 1972]:

$$\varepsilon_e = \frac{\varepsilon_r + 1}{2} + \frac{\varepsilon_r - 1}{2}\left[1 + \frac{10t}{a}\right]^{-1/2} \tag{4-20}$$

Fig. 4.3 is a graph of both the susceptance computed from (4-18) and that of the parallel-plate waveguide radiating into a half-space; both are for an assumed air dielectric.

For the TM_{100} mode, $k_x = 0$ and the resonant frequency may be computed from

$$f_r = 4.775 \frac{k_y}{\sqrt{\varepsilon_e}} \quad (GHz) \tag{4-21}$$

where k_y (in cm^{-1}) is obtained from a solution to the transcendental equation (4-12) and where α_y is computed from (4-15). The effect of the impedance boundary condition is to produce a dependence of the resonant frequency on the dimension a; this is not found in the Neumann condition (c.f. eqns. 4-4 and 4-5 with n = 0). This theory produces good agreement with experimentally-

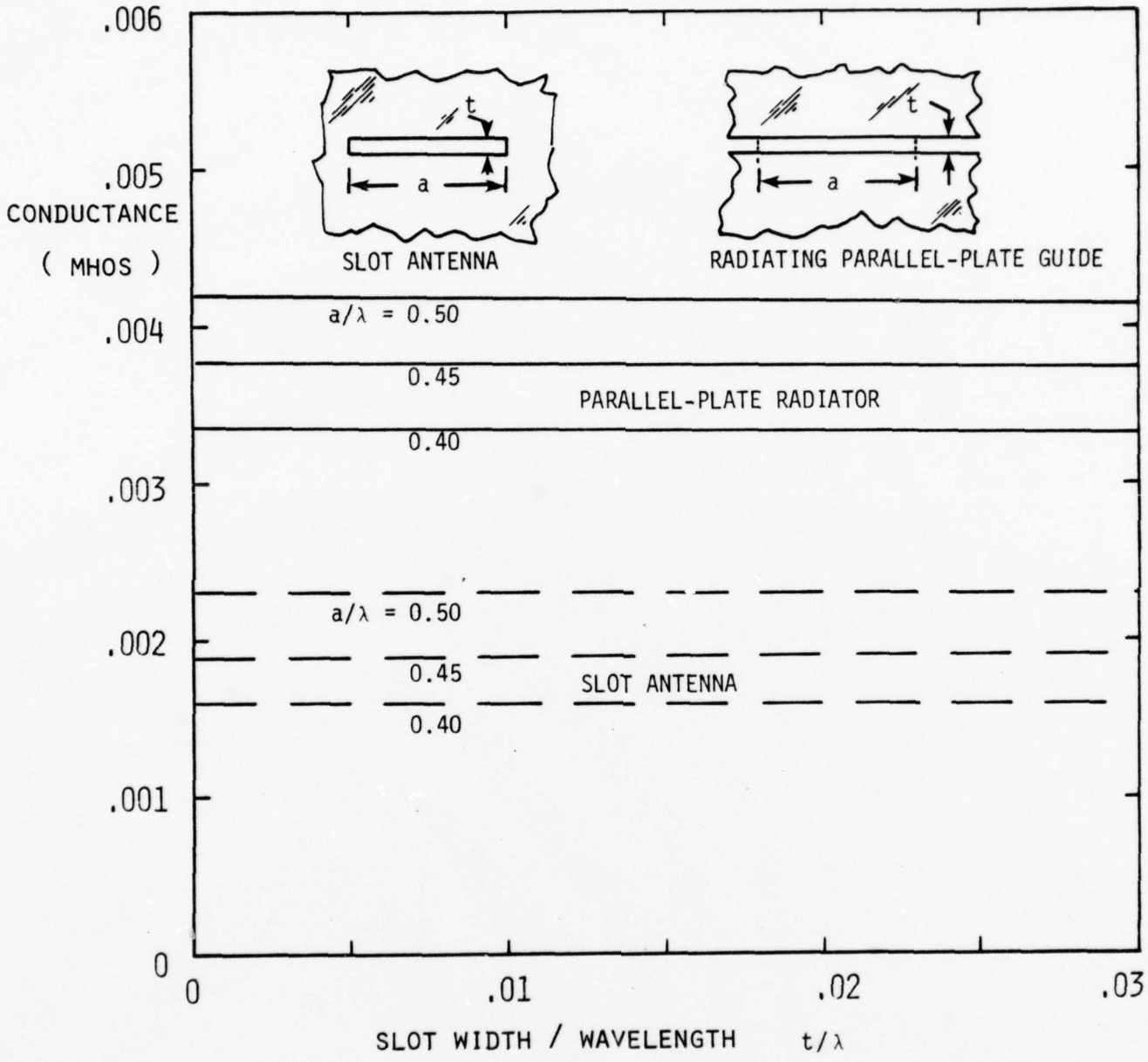

Fig. 4.2 Conductance as a function of slot width for a slot antenna radiating into a half-space (Derneryd,]976) and for a parallel-plate TEM waveguide radiating into a half-space (Harrington, 1961).

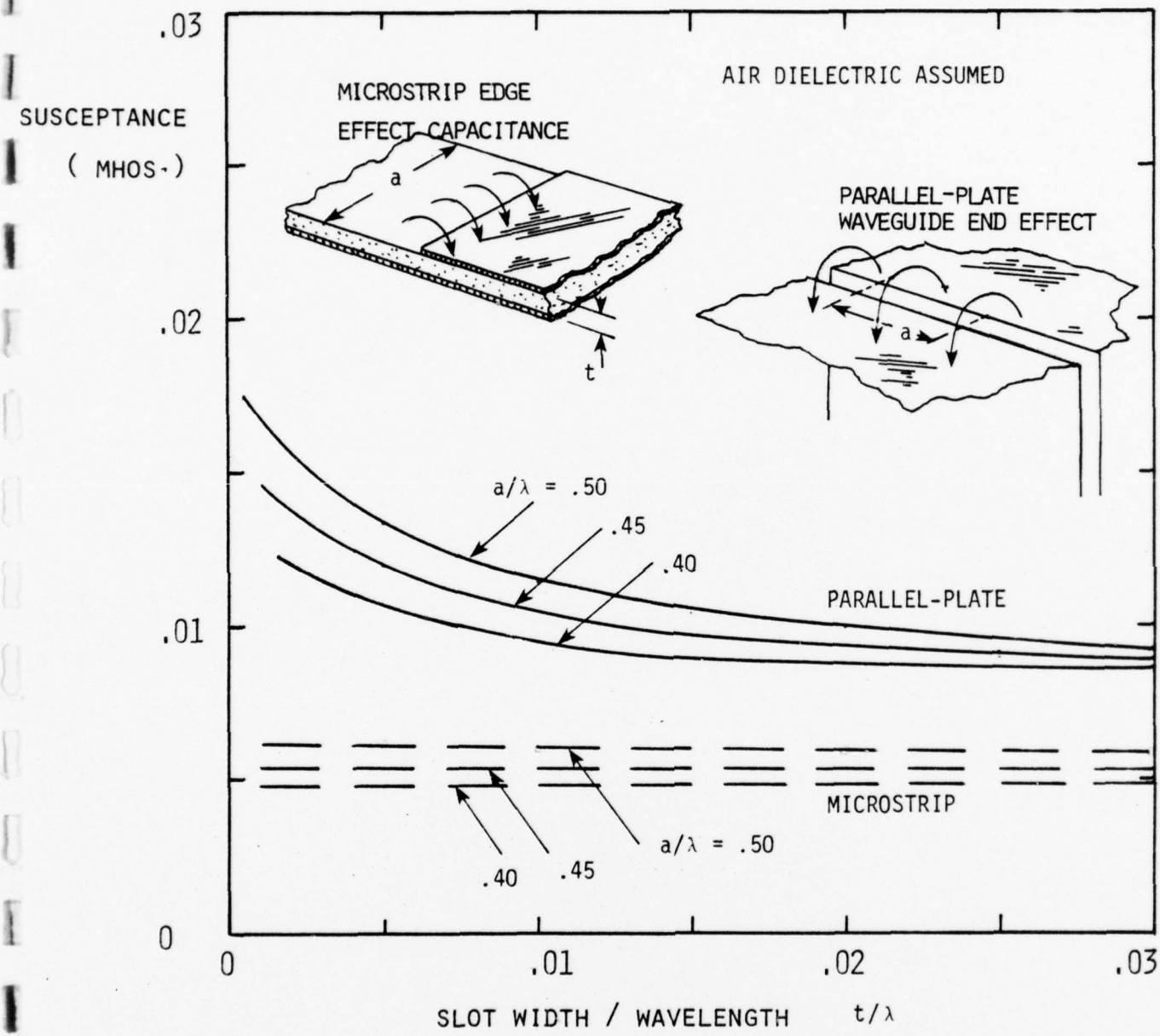

Fig. 4.3 Susceptance as a function of slot width for a microstrip open circuit and for a parallel-plate waveguide radiating into half-space. An air dielectric is assumed for both cases.

measured resonant frequencies at both L-band [Lo, et.al., 1977] and S-band, as is shown in Figs. 4.4 and 4.5. In both cases, it is noted that as the dimension a is increased the resonant frequency decreases; this can be seen more clearly in Fig. 4.6 which is a graph of both left- and right-hand sides of (4-12). The solution for the TM_{100} mode in the Neumann condition is $k_y b = \pi$; however, with an impedance condition, this becomes slightly less, typically 96% to 98% of π.

The values of α are complex, although the real part is normally much larger than the imaginary part (because of the susceptance being larger than the conductance). Thus, in solving (4-15), only the real part of α is used and the eigenvalues are approximately real.

The interior fields and input impedance may be calculated using a modification of the Fourier series expansion presented in Sec. 4.1.1 by letting the resonant frequencies become complex [Harrington, 1961, p. 435]:

$$\omega^2_{mn} = \omega_r^2 \left(1 + \frac{j}{Q}\right) \tag{4-22}$$

where ω_r is the TM_{mno} resonant frequency. In the vicinity of resonance, (4-10) becomes*

$$Z_{in} = j X_L - j \frac{\omega t \chi^2_{mn}}{\varepsilon ab} \frac{\cos^2 \frac{m\pi y_o}{b} \cos^2 \frac{n\pi x_o}{a}}{\omega^2 - \omega^2_{mn}\left(1 + \frac{j}{Q}\right)} \tag{4-23}$$

where X_L is the series inductance of the probe feed connected to the microstrip patch, i.e.

$$X_L = \frac{376}{\sqrt{\varepsilon_r}} \tan \frac{2\pi t}{\lambda_o} \qquad (\Omega) \tag{4-24}$$

The second term of (4-23) is of the same form as the input impedance to a parallel RLC circuit as shown in Fig. 4.7; thus,

$$R = \frac{Q}{\omega_{mn}} \frac{\chi^2_{mn} t}{\varepsilon ab} \cos^2 \frac{m\pi y_o}{b} \cos^2 \frac{n\pi x_o}{a} \tag{4-25}$$

$$L = \frac{1}{\omega^2_{mn}} \frac{\chi^2_{mn} t}{\varepsilon ab} \cos^2 \frac{m\pi y_o}{b} \cos^2 \frac{n\pi x_o}{a} \tag{4-26}$$

* It is assumed here that only one resonant mode is excited, i.e. no closely-spaced modes or degeneracies.

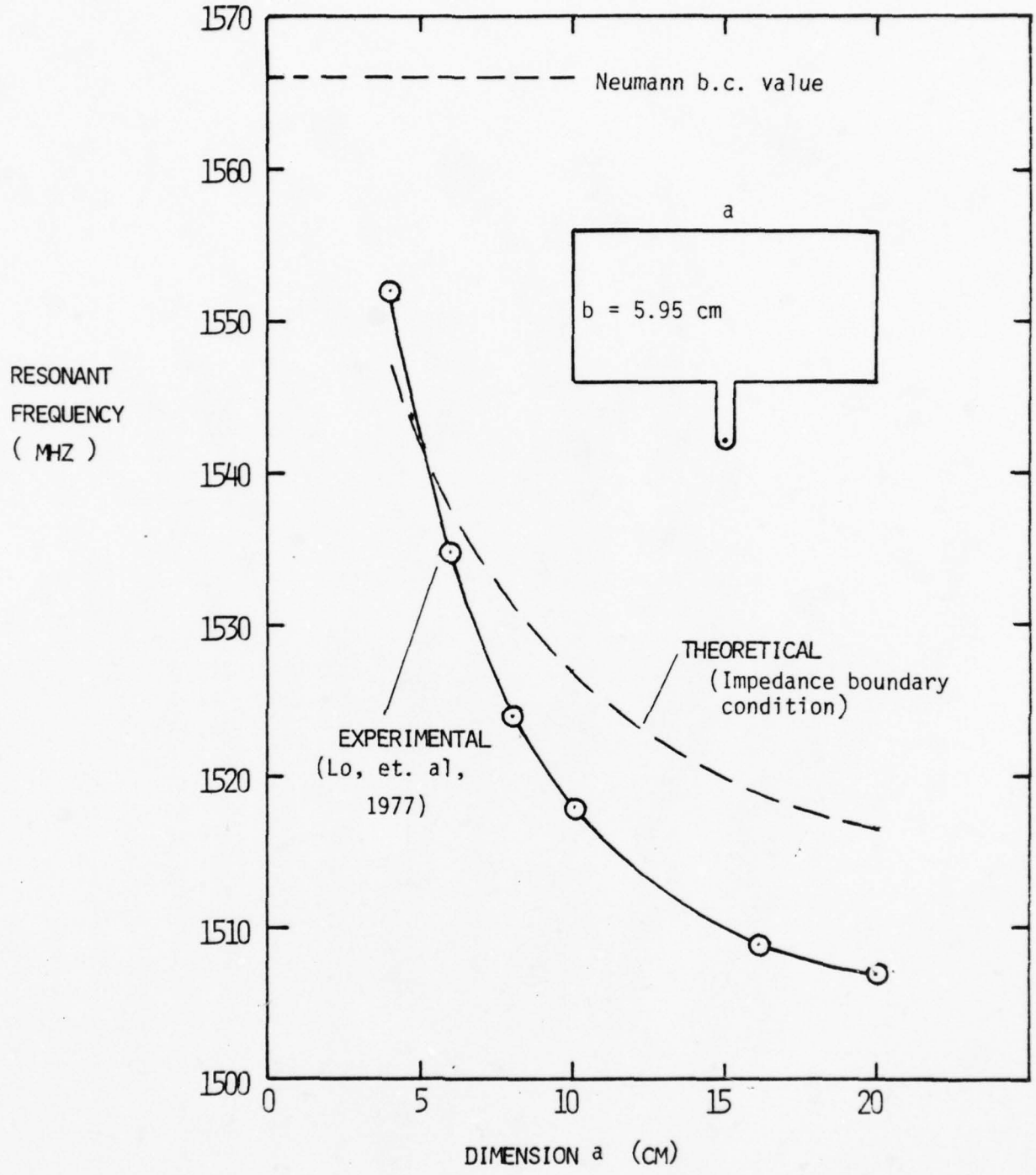

Fig. 4.4 A comparison between experimentally-determined resonant frequencies and theoretical values based on an impedance boundary condition. L-band microstrip patch fed by microstrip transmission line [Lo, et. al., 1977].

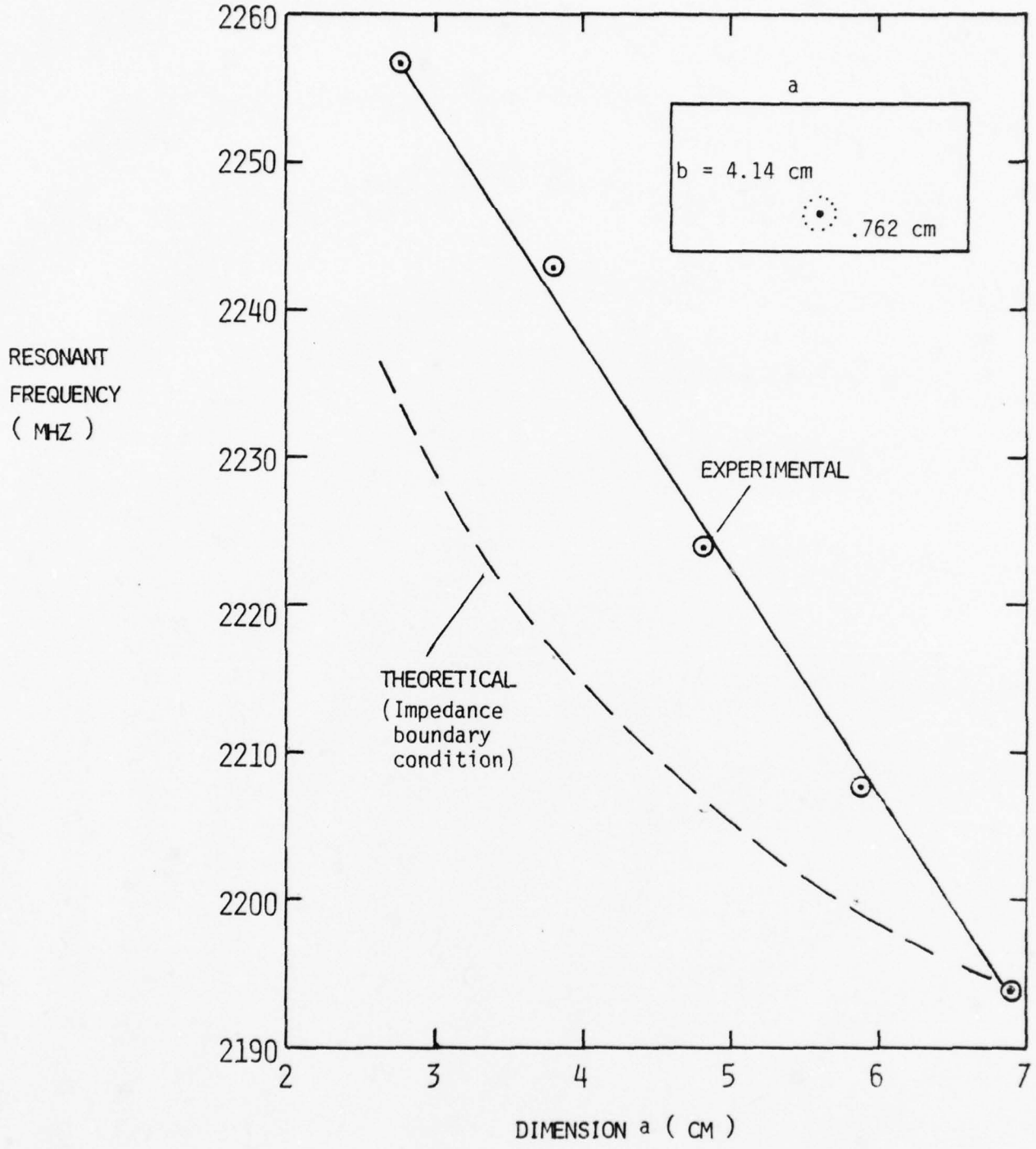

Fig. 4.5 A comparison between experimentally-determined resonant frequencies and theoretical values based on an impedance boundary condition. S-band microstrip patch fed coaxially; experimental values include compensation for probe series inductance effect.

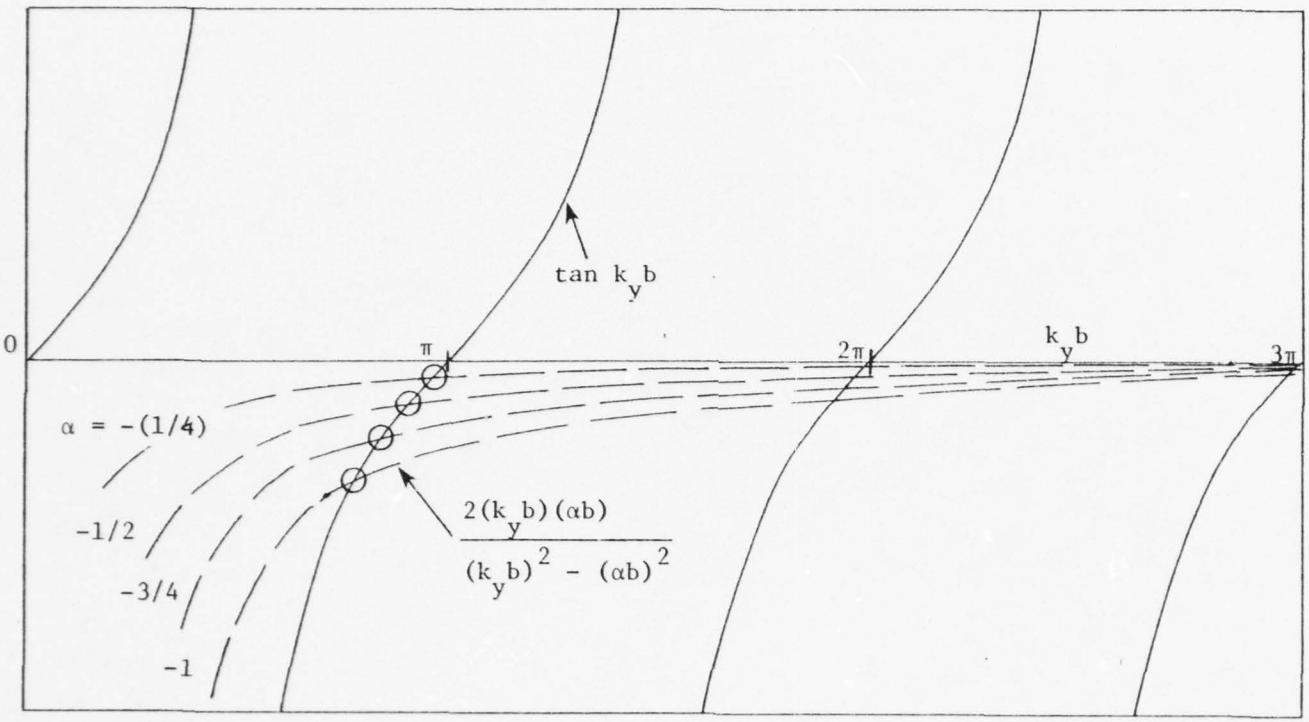

Fig. 4.6 Illustrating the effect of the wall admittance on the downshift of the resonant frequency for the TM_{100} mode. Note that the impedance parameter α has less effect on higher-order modes.

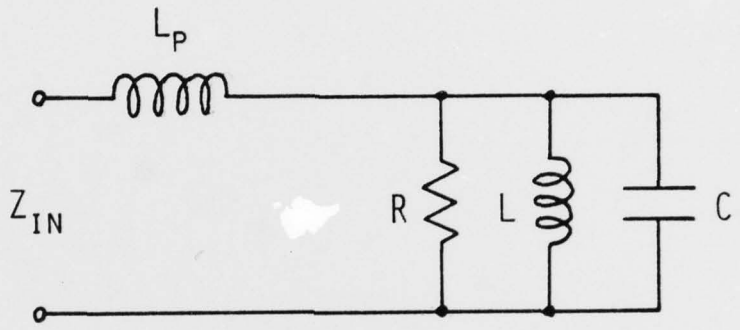

L_P = SERIES INDUCTANCE ASSOCIATED WITH PROBE FEED

R = RESISTANCE ASSOCIATED WITH RADIATION AND HEAT LOSSES

L = INDUCTANCE ASSOCIATED WITH ENERGY STORAGE IN CAVITY

C = CAPACITANCE ASSOCIATED WITH ENERGY STORAGE IN CAVITY

Fig. 4.7 Equivalent circuit model of microstrip cavity fed by coaxial probe.

$$C = \frac{\varepsilon ab}{t}\left[\chi_{mn}^2 \cos^2\frac{m\pi y_o}{b} \cos^2\frac{n\pi x_o}{a}\right]^{-1} \qquad (4\text{-}27)$$

Also it is noted that

$$\omega_{mn}^2 = \frac{1}{L\,C} \qquad (4\text{-}28)$$

and

$$Q = \omega_{mn}\, R\, C \qquad (4\text{-}29)$$

The resistance may be computed by noting that at the resonant frequency (where the second term in 4-23 becomes purely real), the input resistance is

$$R_{in} = R_c + R_d + R \qquad (4\text{-}30)$$

where R_c is the equivalent resistance associated with dissipative losses in the conductors (c.f. eqn. 2-17) and R_d is the equivalent resistance associated with dissipative losses in the dielectric; R is then the reciprocal of twice the conductance of one slot (eqn. 4-17), i.e. for the dominant mode

$$R = 59.8\ (\lambda_o\ /\ a) \qquad (\ \Omega\ ) \qquad (4\text{-}31)$$

The first term in (4-27) will be recognized as the d.c. capacitance of a parallel-plate capacitor of area ab and thickness t.

It is emphasized that in (4-23) the series inductance term is associated with the coaxial probe and results from coupling to the TM field. For a microstrip antenna fed by a microstrip feedline this term is not present, and the input impedance is given by the second term of (4-23).

Fig. 4-8 compares the input impedance of the present model with the transmission-line model of Derneryd [1976] for a microstrip-fed patch with a = 6.858 cm, b = 4.140 cm, t = 0.1588 cm and ε_r = 2.62. Two significant differences are noted. First, the input resistance at resonance from (4-23) is 118 Ω whereas that from the Derneryd model is 220 Ω; this results from the different models used for the slot conductance. Second, the resonant

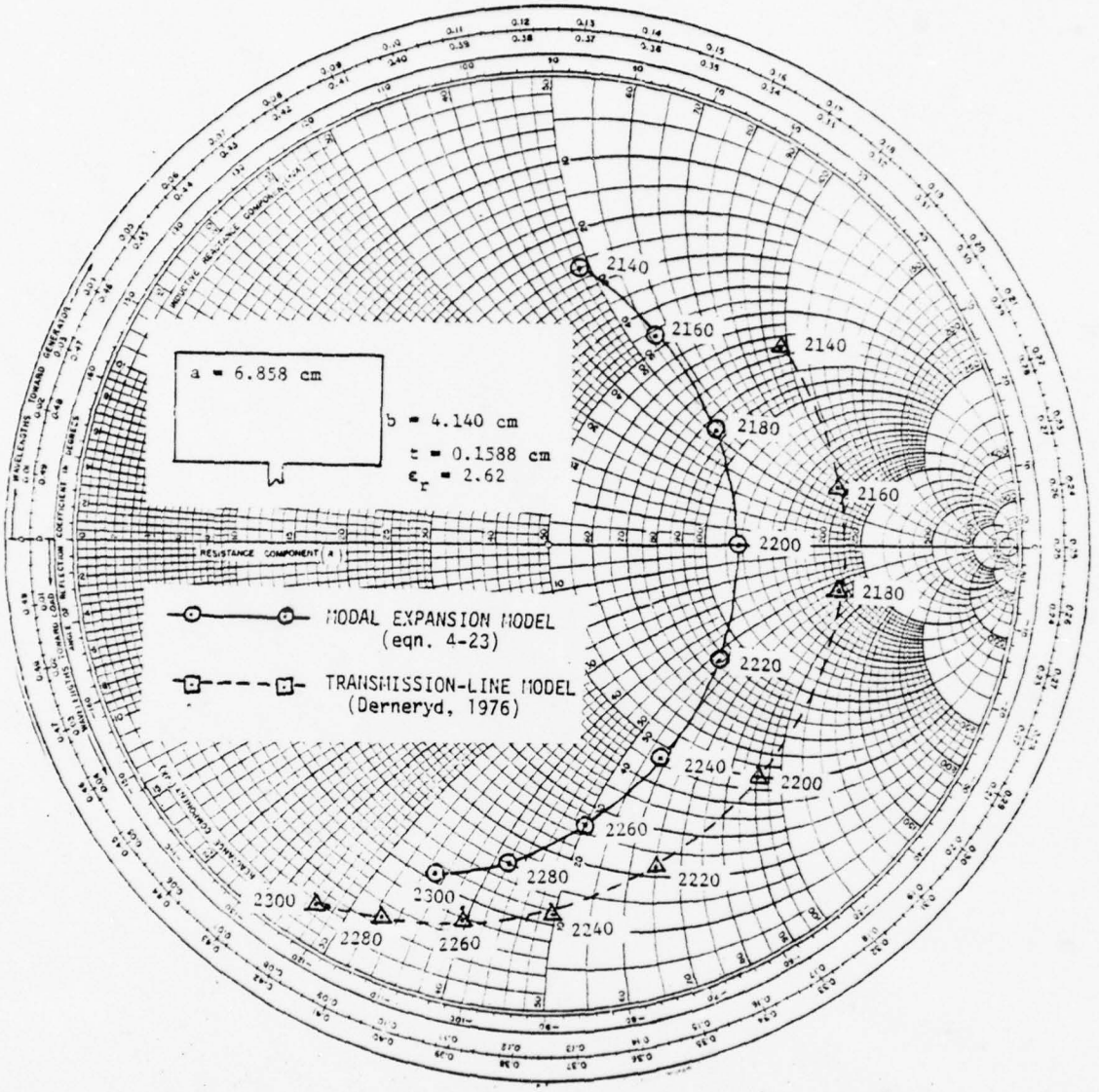

Fig. 4.8 Comparison of Modal Expansion Model and Transmission Line Model for a microstrip-fed patch with a = 6.858 cm, b = 4.140 cm, t = .1588 cm, and ϵ_r = 2.62.

frequency for the modal expansion model is predicted to be 2194 MHz, whereas the Derneryd model predicts 2172 MHz. The measured resonant frequency for this antenna was 2195 MHz, in nearly perfect agreement with the modal expansion model.

For the TM_{100} mode, the impedance is predicted to be independent of the probe position x_o; this is verified by experimental data [Weinschel & Lanphere, 1973] for feed points ranging from the center to near the corner.

When the patch is fed by a probe (coaxially), the inductive term must be retained in (4-23), which has the effect of moving the impedance circle toward the inductive side of the Smith Chart. For a typical substrate with $\varepsilon_r = 2.62$ and $t = 0.1588$ cm, $X_L = 7.7\ \Omega$ at 1 GHz, 15.5 Ω at 2 GHz, and 80.1 Ω at 10 GHz. Since practical impedance measurements are often made with coaxially-fed patches, it is important to correct such measurements for the inductive effect, particularly at S-band or higher.

As the feed-point y_o is moved inward toward the center of the element, the resistance decreases in accordance with (4-25); the capacitance increases but the inductance decreases in such a way as to maintain the same resonant frequency and the same Q.

Figs. 4.9 - 4.12 compare measured impedance data with theoretical values (based on 4-23) for a patch with a centered feedpoint at several inset distances ranging from 0 cm (edge) to 1.524 cm. The agreement is quite good, and seems to validate many of the preceding assumptions. Fig. 4.13 compares experimental [Dunn, 1978] and theoretical impedances for an edge-fed L-band patch and again the agreement is good.

One restriction on the present formulation, which assumes a single well-isolated resonant mode, is that it becomes less accurate as the dimension a becomes less than b. Thus, the second term in (4-23) includes only one mode; future formulations will include multiple modes and provisions for estimating the effect of feed probe slight positioning errors on degenerate modes (e.g. TM_{010} and TM_{100} for a square or nearly-square patch).

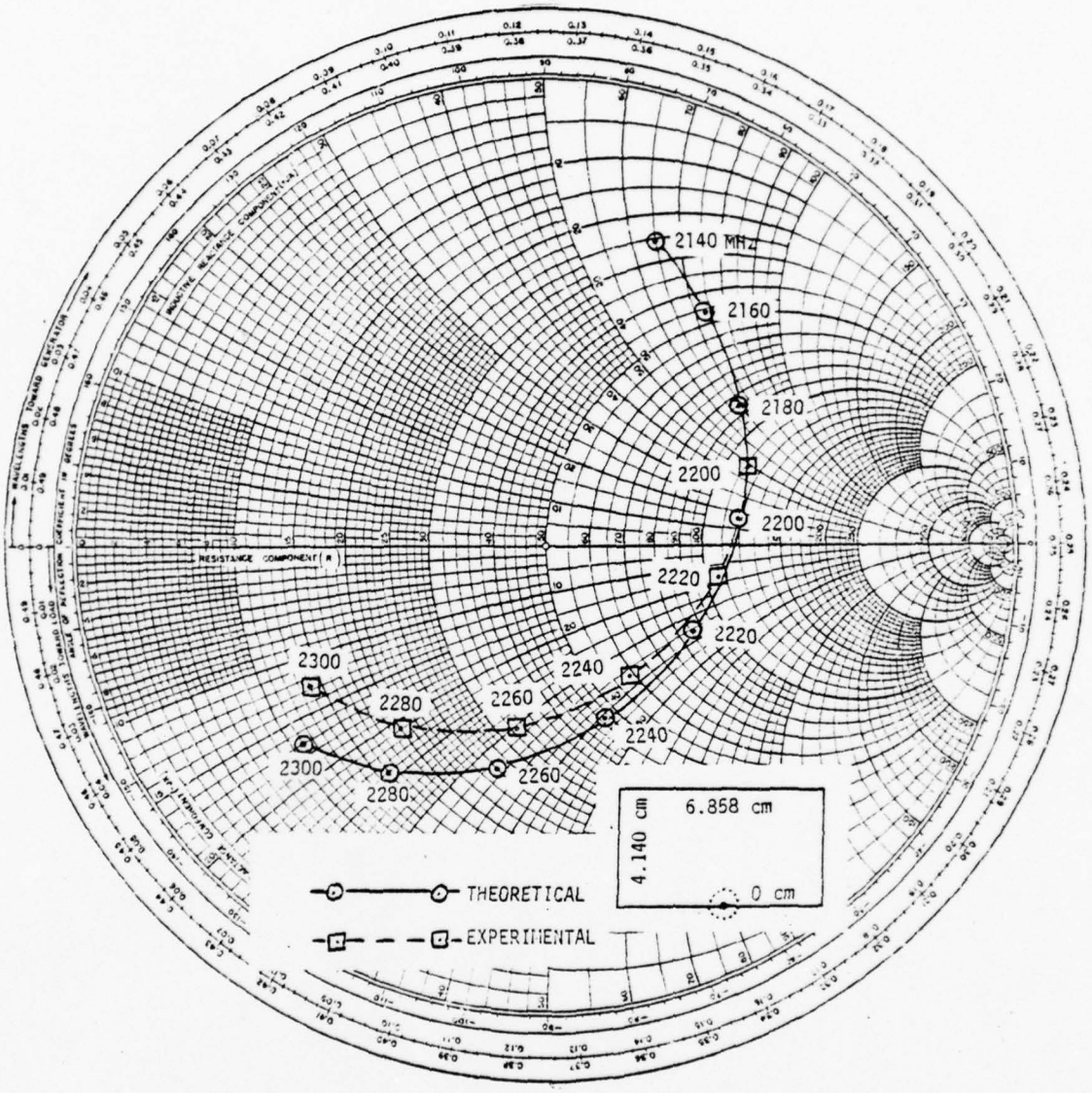

Fig. 4.9 Comparison between theoretical and experimental values of impedance for S-band patch fed at the edge.

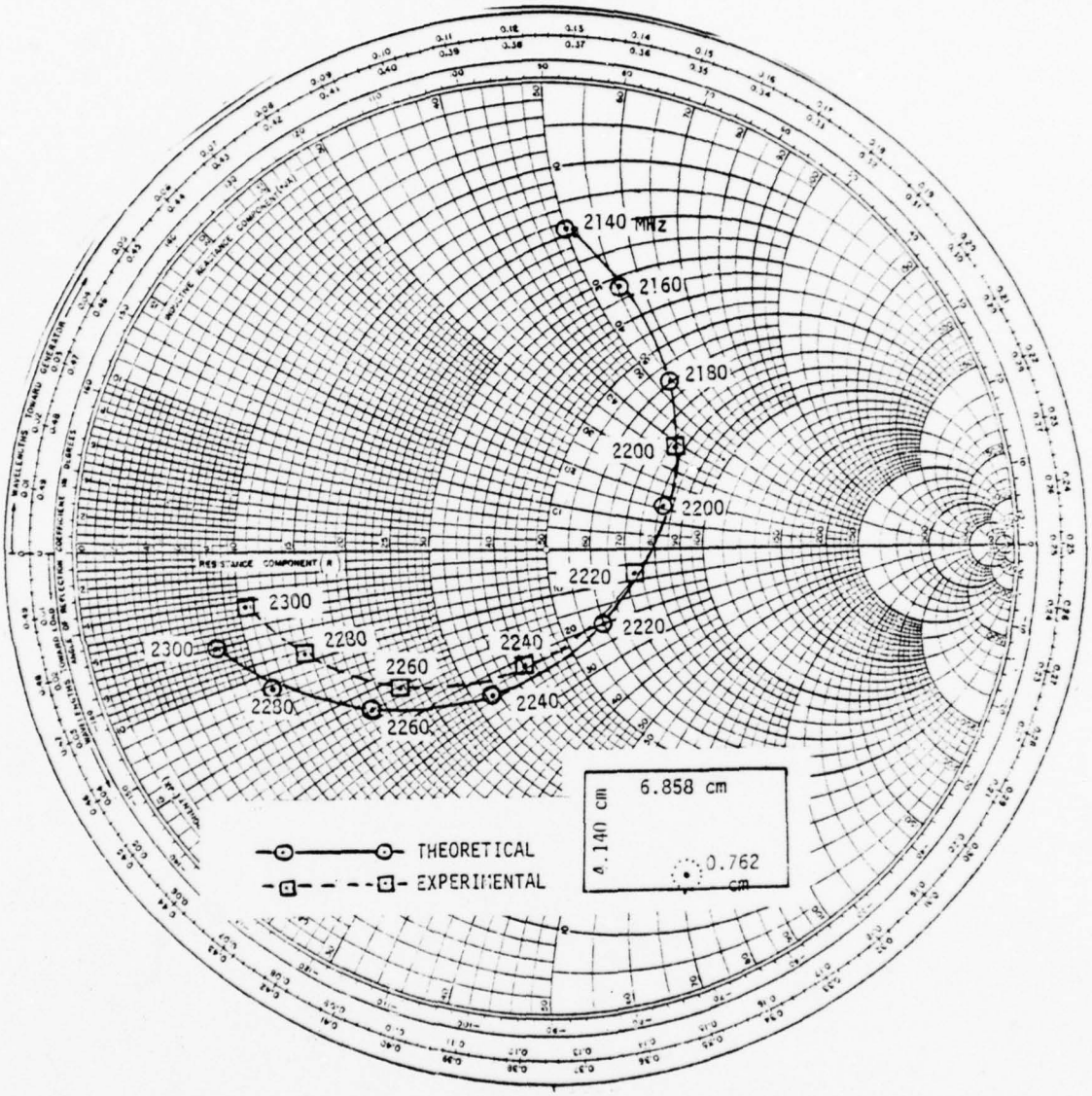

Fig. 4.10 Comparison between theoretical and experimental values of impedance for S-band patch fed at 0.762 cm in from edge.

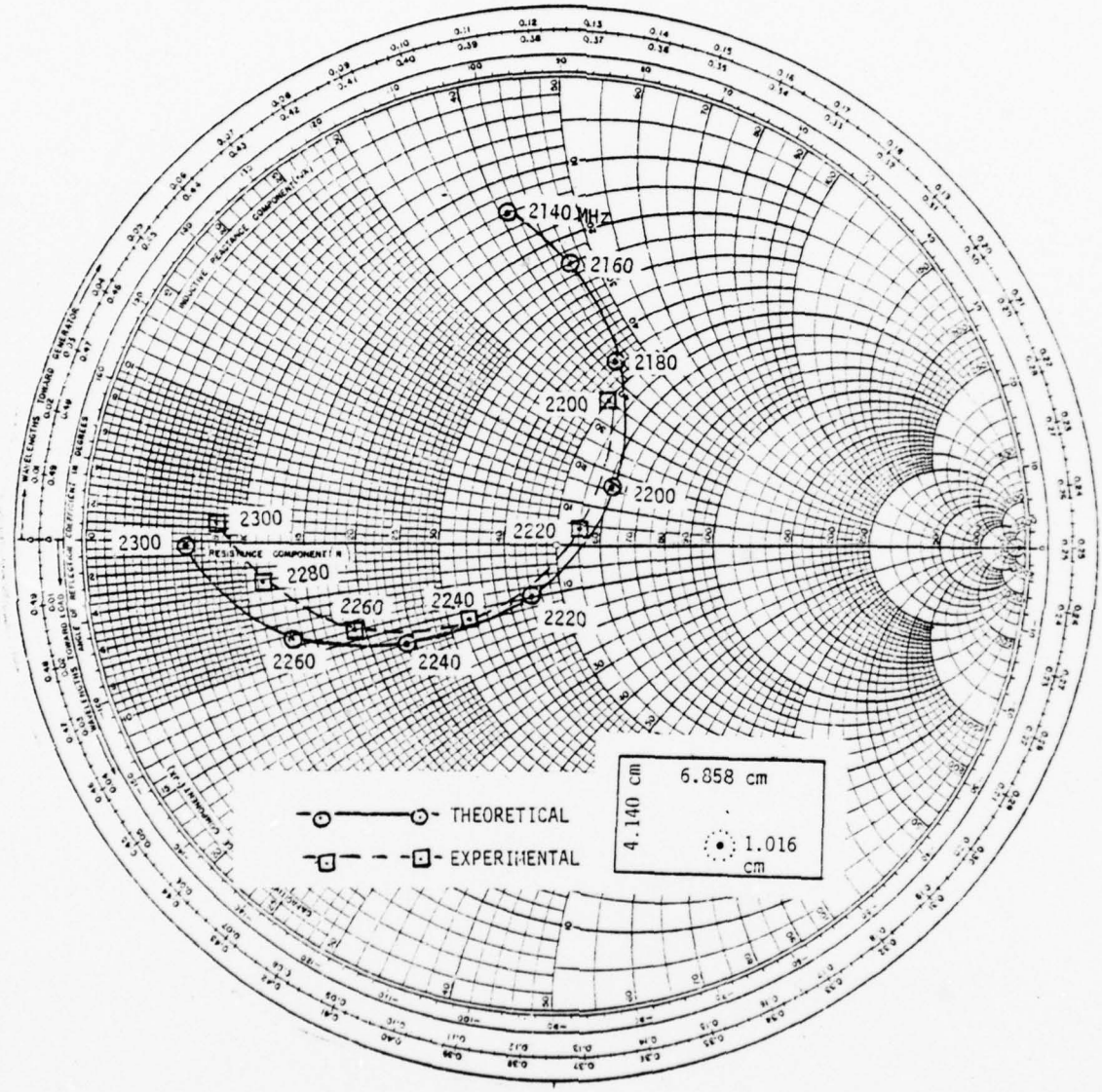

Fig. 4.11 Comparison between theoretical and experimental values of impedance for S-band patch fed at 1.016 cm in from edge.

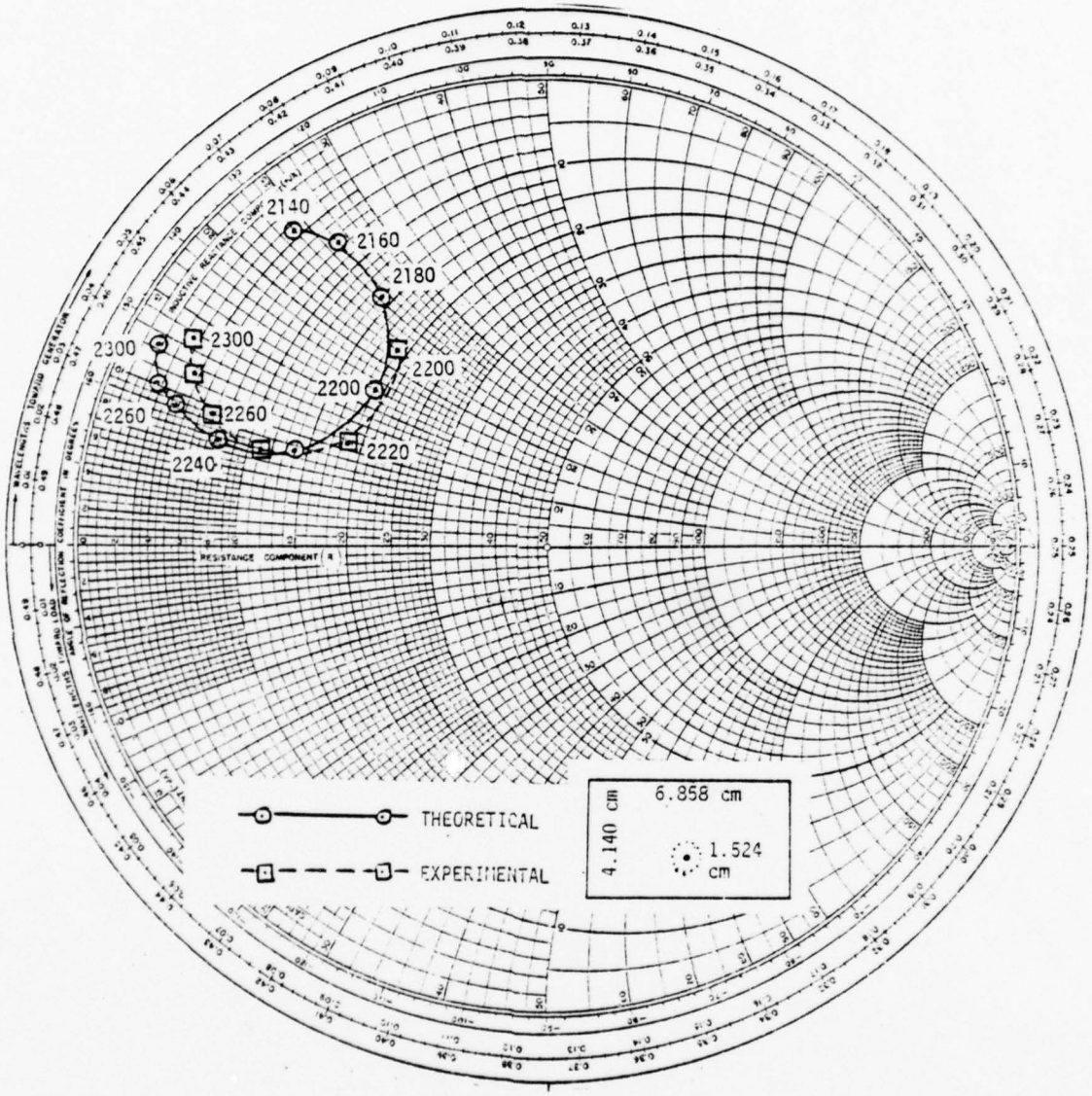

Fig. 4.12 Comparison between theoretical and experimental values of impedance for S-band patch fed at 1.524 cm in from edge.

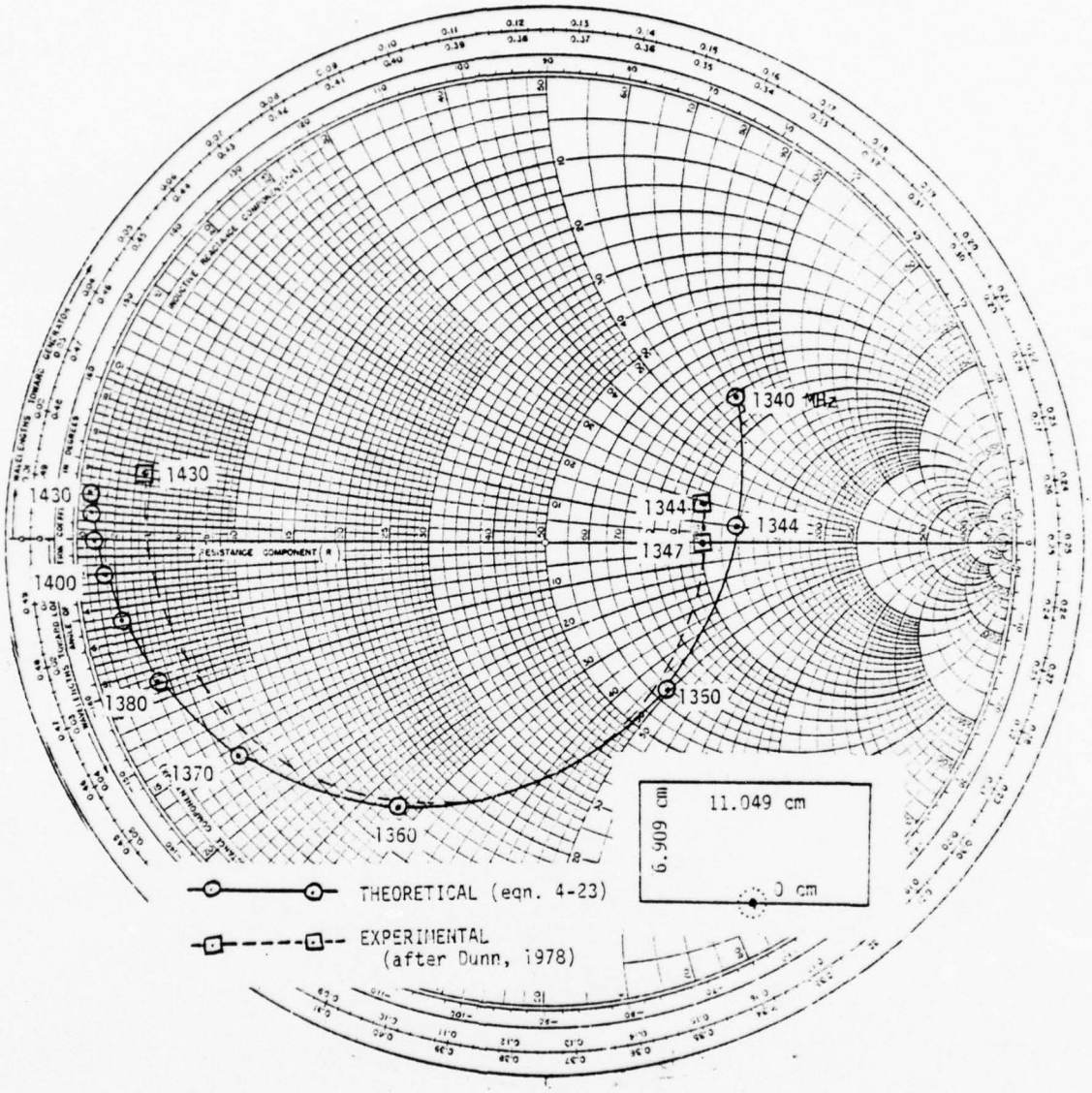

Fig. 4.13 Comparison between theoretical and experimental values of impedance for L-band patch fed at edge.

The power dissipated in the rectangular patch may be divided into a portion associated with conductor losses and the remainder caused by dielectric losses, as described in eqns. (2-16) - (2-18). By using the preceding modal expansions, it is easy to show that at a well-isolated resonant frequency, the power lost as heat in the conducting walls (assumed to be copper) is*:

$$P_{dc} = |I_{in}|^2 R_c \tag{4-32}$$

where

$$R_c = 0.00027\sqrt{f}\ \frac{b}{a}\ Q^2 \quad (\Omega) \qquad (f = \text{frequency in GHz}) \tag{4-33}$$

The power lost as heat in the dielectric is

$$P_{dd} = |I_{in}|^2 R_d$$

where

$$R_d = 30\ \frac{\tan\delta}{\varepsilon_r'}\ \frac{t\lambda_o}{ab}\ Q^2 \quad (\Omega) \tag{4-35}$$

where ε_r' is the real part of the relative permittivity and $\tan\delta$ is the loss tangent. The input power is

$$P_{in} = |I_{in}|^2 R_{in} \tag{4-36}$$

The radiation resistance referred to the input is therefore

$$R = R_{in} - R_c - R_d \tag{4-37}$$

where

$$R = 59.8\ (\lambda_o/a) \quad (\Omega) \tag{4-38}$$

Also, $Q \simeq Q_r = \omega W/(\text{Re}\ P_r)$ where $\text{Re}\ P_r = G_w|V|^2$ and $W = \frac{1}{2}C_T|V|^2$ and where C_T includes both the patch and edge-effect capacitance. This gives

$$Q = (\varepsilon_r b/2t) + (2\varepsilon_e \Delta\ell/t) \tag{4-39}$$

Thus, the antenna efficiency is

$$\eta = 1 - \frac{P_{dc} + P_{dd}}{P_{in}} = 1 - \frac{R_c + R_d}{R_{in}} \tag{4-40}$$

*It is assumed that the patch is fed on the edge and in the TM_{100} mode.

As a numerical example, let a = 6.858 cm, b = 4.140 cm, t = .1588 cm, $\varepsilon_r' = 2.62$ and $\lambda_o = 13.6$ cm. Then, from (4-33), $R_c = .38\ \Omega$ and from (4-38), we get Q = 37, R = 119 Ω. Table 4-2 shows the effect of various loss tangents on both R_d and the antenna efficiency .

Table 4-2

Antenna Efficiencies for Microstrip Patch

Loss Tangent tan δ	Equiv. Diel. Resistance R_d	Efficiency (Loss) - η
0.0001	0.12 Ω	99.58 % (.02 dB)
0.0005	0.60	99.18 (.04)
0.001	1.19	98.68 (.06)
0.005	5.96	94.67 (.24)
0.01	11.92	89.66 (.47)

Fig. 4.13-1 is a graph of the antenna efficiency as a function of substrate thickness for several loss tangents and for the microstrip patch in the above example.

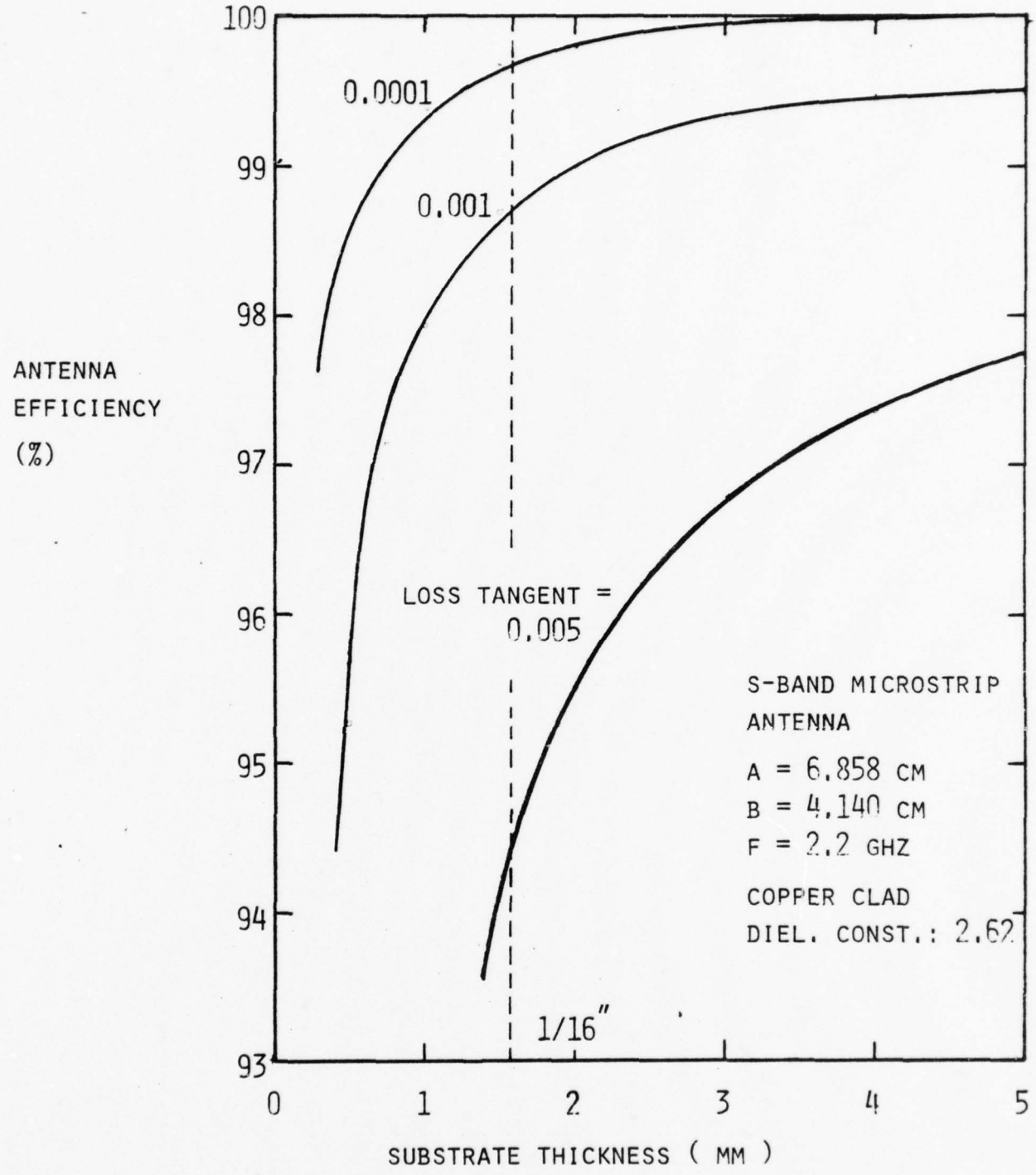

Fig. 4.13-1 Antenna efficiency (gain/directivity) vs. substrate thickness for a rectangular patch S-band microstrip antenna.

4.1.3 Multiple Mode Effects

In the preceding formulation of (4-23) for the impedance of a rectangular patch, it was assumed that there was essentially one resonant mode whose bandwidth was much less than the frequency separation to the next adjacent modes. However, for some microstrip antenna designs, this is not necessarily the case; for example, a square patch fed at a corner can excite both the TM_{100} and TM_{010} modes in phase and at the same resonant frequency.

Consider a corner-fed rectangular patch where the dimensions a and b are approximately the same. The total input impedance is the sum of the impedances of each mode; neglecting the inductive reactance of the probe and using only the second term of (4-23) with $x_o = y_o = 0$, the input impedance is

$$Z_{in} = Z_{100} + Z_{010} \tag{4-40a}$$

where

$$Z_{100} = \frac{-2j\omega t}{\varepsilon ab\ [\omega^2 - \omega_{10}^2(1 + \frac{j}{Q_{10}})]} \tag{4-40b}$$

$$Z_{010} = \frac{-2j\omega t}{\varepsilon ab\ [\omega^2 - \omega_{01}^2(1 + \frac{j}{Q_{01}})]} \tag{4-40c}$$

It is assumed that all other modes are short-circuited.

This model raises the possibility of increasing the bandwidth of the patch by stagger-tuning the modes. The resonant frequency ω_{10} is determined primarily by the dimension b and the resonant frequency ω_{01} is determined primarily by the dimension a.

Figs. 4-14 a,b, and c show this effect by comparing the impedance behavior of square and nearly-square patches, all with a = 4.14 cm, t = 0.1588 cm and $\varepsilon_r = 2.62$. Fig. 4-14a shows the plot for b = a = 4.14 cm (square patch), which is the degenerate case. Fig. 4-14b is for b = 4.328 cm and shows a loop which is associated with the frequency band where Z_{100} and Z_{010} are about the same. Fig. 4-14c is for b = 4.500 cm and the loop is seen to become larger at the same time the resonant frequency decreases. This multiple-mode excitation technique may hold promise for some improvement in bandwidth.

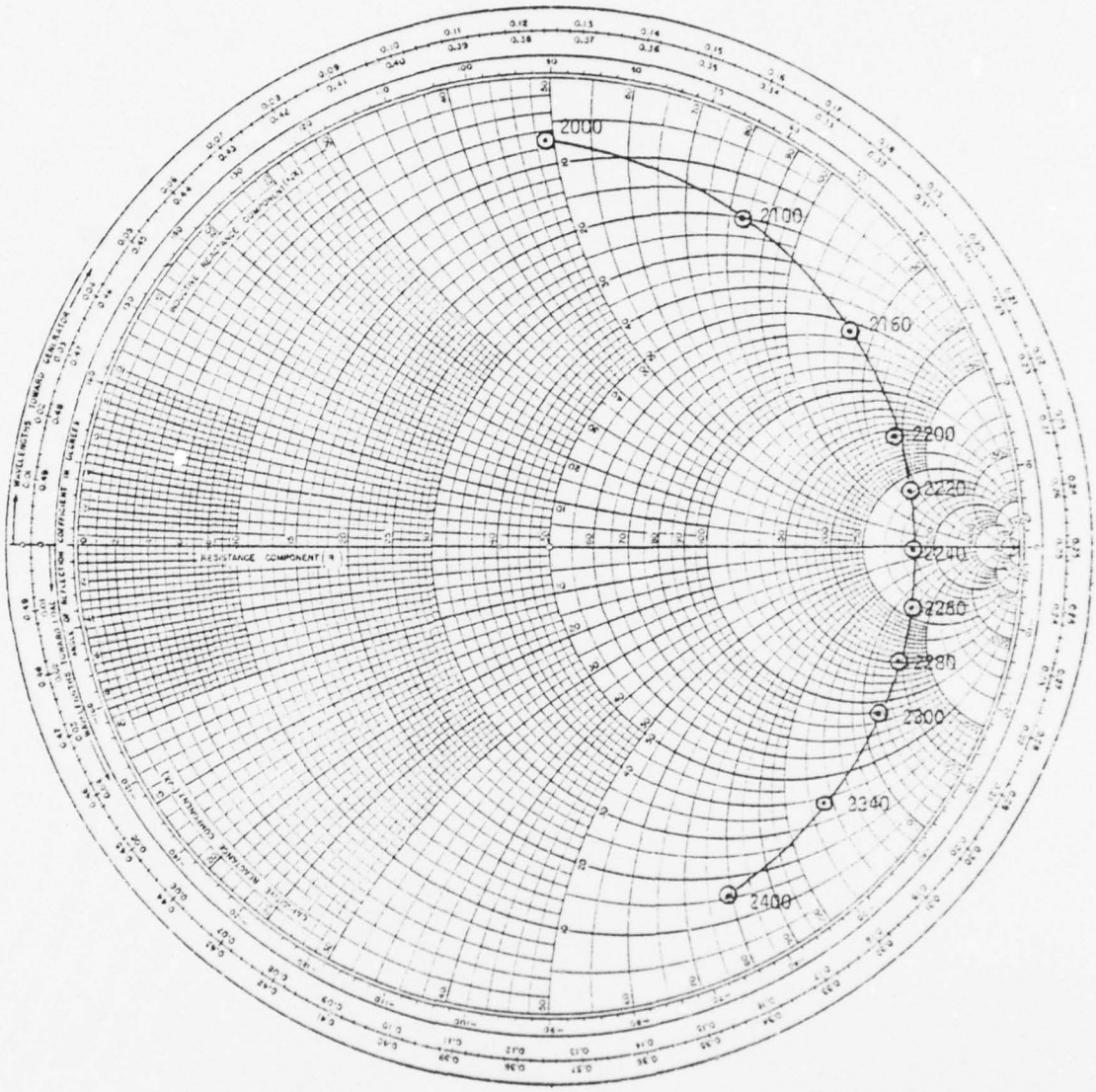

Fig. 4-14a. Calculated impedance diagram for a square microstrip patch with a = b = 4.14 cm.

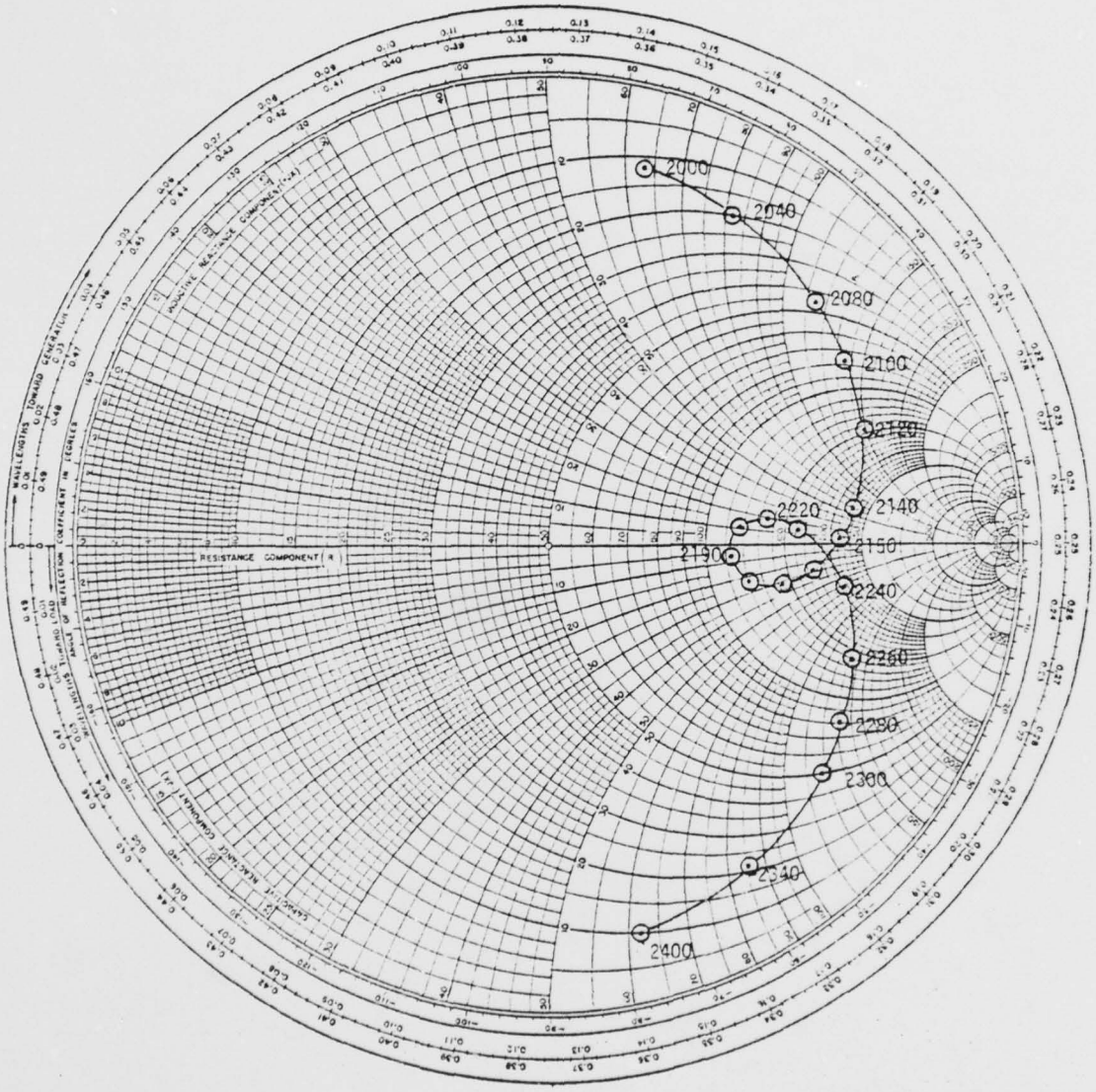

Fig. 4-14b. Calculated impedance diagram for a rectangular microstrip patch with a = 4.14 cm, b = 4.328 cm.

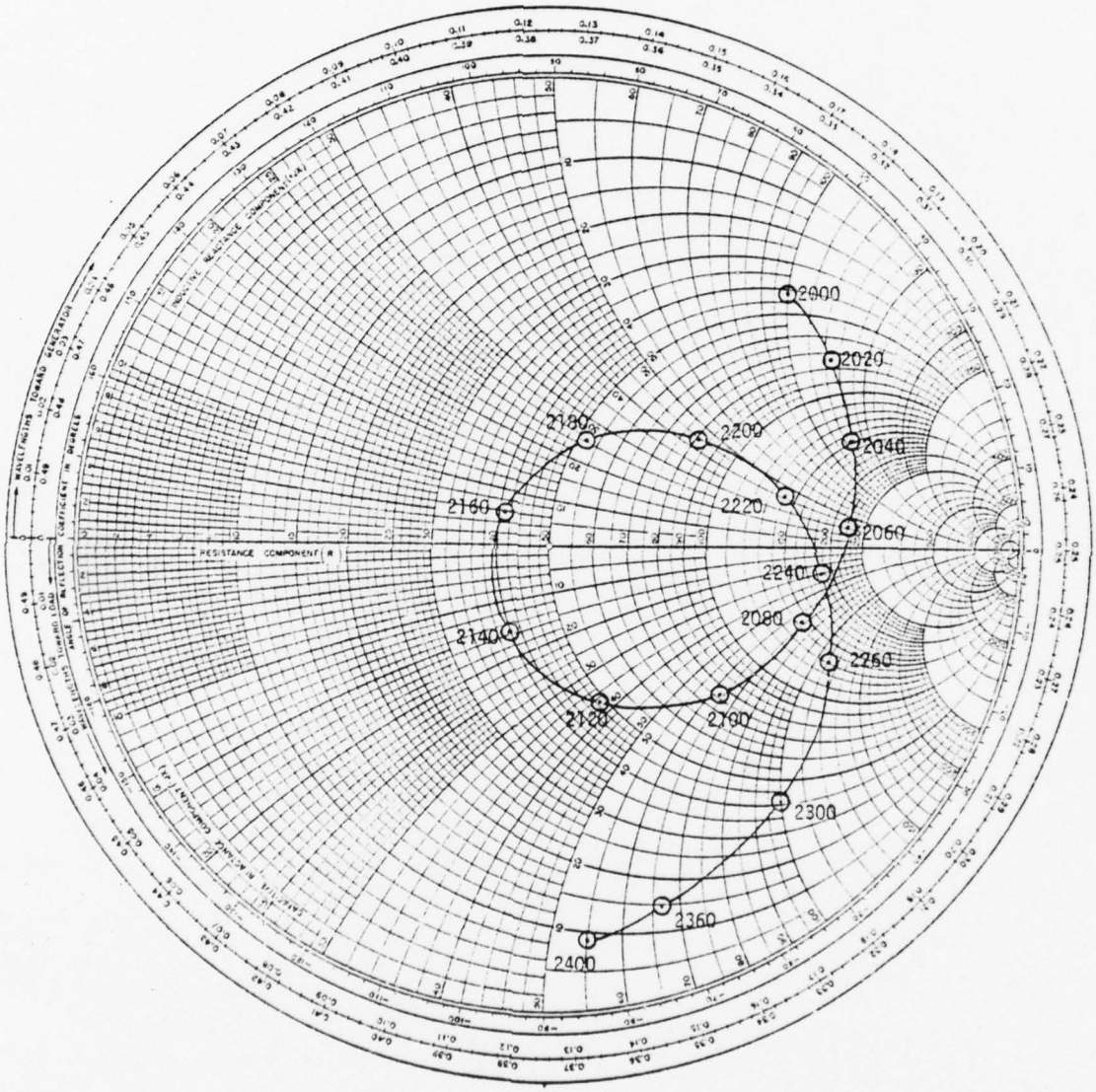

Fig. 4-14c. Calculated impedance diagram for a rectangular microstrip patch with a = 4.14 cm, b = 4.50 cm.

Multiple-mode excitation can also produce various polarization states of the antenna. For a square corner-fed patch, the polarization is linear with the E-plane oriented along the diagonal containing the feed. For corner-fed rectangular patches with a ≠ b, however, the possibility exists of producing circular polarization with a single feedpoint.

By using (4-8) and (4-122), the interior fields of a corner-fed rectangular patch may be written as

$$\bar{E}(x,y) = \hat{z}\,\frac{j\omega I_{in}}{\varepsilon ab}\sum_{m,n}\frac{\cos\frac{m\pi y}{b}\cos\frac{n\pi x}{a}}{\omega^2 - \omega_{mn}^2\left(1+\frac{j}{Q_{mn}}\right)} \tag{4-40d}$$

For a patch with dimension a slightly less than b, the TM_{100} and TM_{010} modes will have closely-spaced resonant frequencies so that only two terms of the series are retained:

$$\bar{E}(x,y) = \hat{z}\,\frac{j\omega I_{in}}{\varepsilon ab}\left\{\frac{\cos\frac{\pi y}{b}}{\omega^2 - \omega_{10}^2\left(1+\frac{j}{Q_{10}}\right)} + \frac{\cos\frac{\pi x}{a}}{\omega^2 - \omega_{01}^2\left(1+\frac{j}{Q_{01}}\right)}\right\} \tag{4-40e}$$

The magnetic surface current on the y = 0 wall is thus given by

$$\bar{M}_{sx} = \hat{x}\,\frac{j\omega I_{in}}{\varepsilon\, ab}\left\{\frac{1}{\omega^2 - \omega_{10}^2\left(1+\frac{j}{Q_{10}}\right)} + \frac{\cos\frac{\pi x}{a}}{\omega^2 - \omega_{01}^2\left(1+\frac{j}{Q_{01}}\right)}\right\} \tag{4-40f}$$

and the magnetic surface current on the x = 0 wall is given by

$$\bar{M}_{sy} = \hat{y}\,\frac{j\omega I_{in}}{\varepsilon\, ab}\left\{\frac{\cos\frac{\pi y}{b}}{\omega^2 - \omega_{10}^2\left(1+\frac{j}{Q_{10}}\right)} + \frac{1}{\omega^2 - \omega_{01}^2\left(1+\frac{j}{Q_{01}}\right)}\right\} \tag{4-40g}$$

The second term in (4-40f) and the first term in (4-40g) have no net effect on the polarization in the broadside direction.

To achieve circular polarization, $|M_{sx}| = |M_{sy}|$ and their phases must differ by 90°.

By using (4-40f) and (4-40g) it is found through trial-and-error numerical evaluation that a corner-fed patch with b/a = 1.029 should produce

approximately circular polarization in the broadside direction. A similar prediction has been made by Kaloi [1978] although no ratio of b/a was given and no computed or measured axial ratios were presented. The numerical procedure for the prediction of circular polarization is to enforce the above conditions, i.e.

$$|\omega^2 - \omega_{10}^2(1 + \frac{j}{Q_{10}})| = |\omega^2 - \omega_{01}^2(1 + \frac{j}{Q_{01}})| \qquad (4\text{-}40h)$$

and

$$\tan^{-1} \frac{-j\omega_{10}^2/Q_{10}}{\omega^2 - \omega_{10}^2} - \tan^{-1} \frac{-j\omega_{01}^2/Q_{01}}{\omega^2 - \omega_{01}^2} = \pm (\pi/2) \qquad (4\text{-}40i)$$

As an approximation to the resonant frequencies ω_{10} and ω_{01}, the Neumann boundary condition can be used so that $\omega_{10} \simeq \pi/b\sqrt{\mu\varepsilon}$ and $\omega_{01} \simeq \pi/a\sqrt{\mu\varepsilon}$. Then $Q_{10} = \omega_{10}R_{10}C_{10}$ where $R_{10} \simeq 59.8\lambda_o/a$ and $C_{10} = \varepsilon ab/2t$; similarly, $Q_{01} = \omega_{01}R_{01}C_{01}$ where $R_{01} \simeq 59.8\lambda_o/b$ and $C_{01} = C_{10}$. These equations are easily solved by iterative means using a programmable calculator.

As an example, let a = 4.14 cm and b = 4.26 cm. The predicted on-axis axial ratio vs. frequency is shown in Fig. 4-15. If the patch is fed at the $x_o = 0$, $y_o = 0$ corner, the polarization is left circular; if the patch is fed at the $x_o = 0$, $y_o = b$ corner, the polarization is right circular. The computed polarization bandwidth (defined as the frequency spread between axial ratio values 3 dB greater than the minimum) is 22 MHz.

A corner-fed nearly-square patch with the above dimension was constructed to test the validity of the above theory. The dielectric constant was 2.62, the thickness was 1.588 mm and the patch was fed at the $x_o = 0$, $y_o = 0$ corner by a coaxial probe (SMA connector). The measured axial ratio vs. frequency is shown in Fig. 4.15. The measured impedance diagram is shown in Fig. 4.15-1

First, the agreement between theoretical and experimental axial ratios is very good. Second, it is observed that the excitation of the two modes is in evidence from the presence of the cusp (small loop) at 2200 MHz. It is also noted that the cusp occurs where the axial ratio is minimum. The extensi of this principle relating polarization and impedance for multi-mode microstrip patches is straightforward.

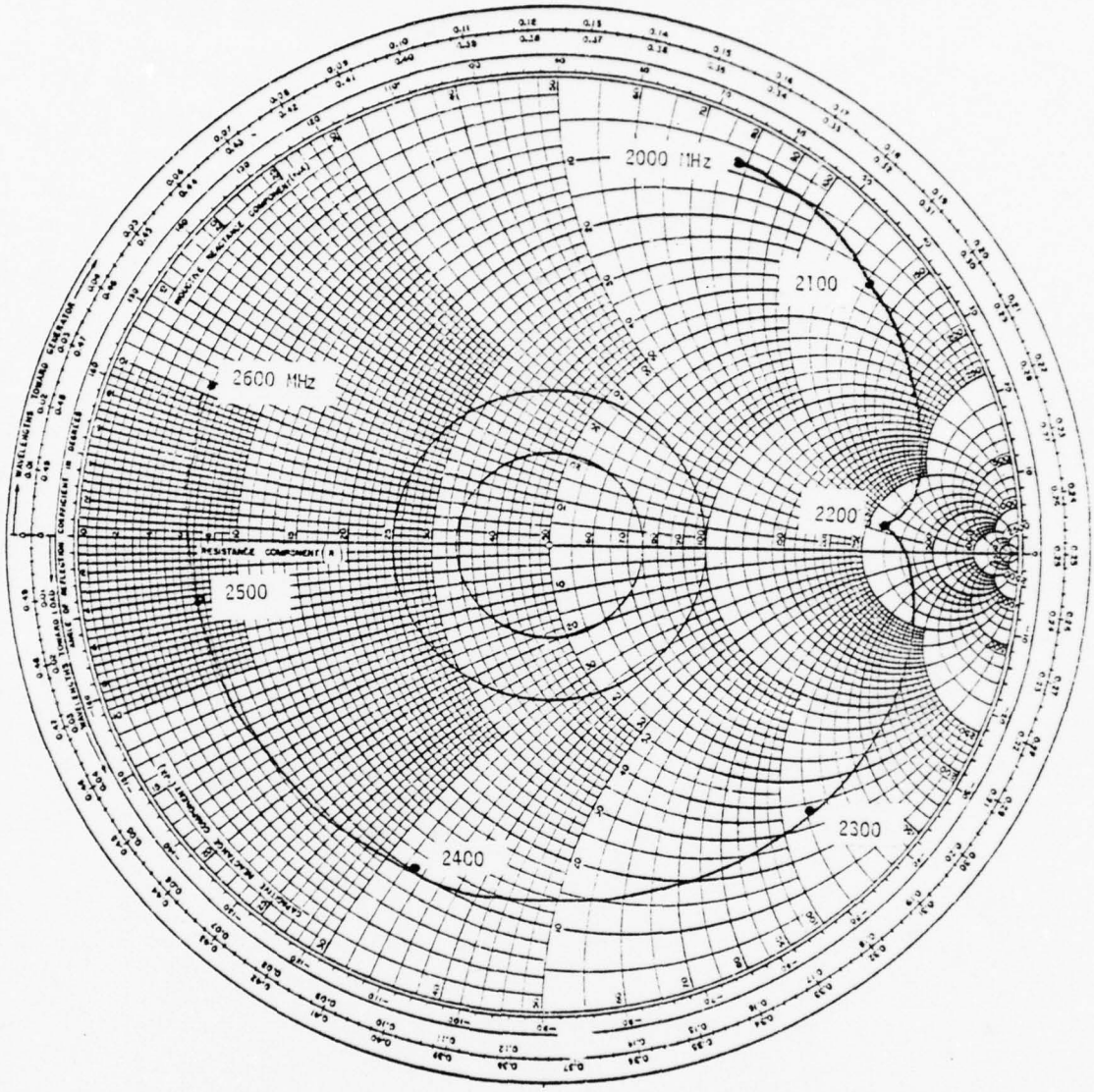

Fig. 4.15-1. Impedance diagram for S-band corner-fed nearly-square microstrip antenna producing circular polarization at 2200 MHz.

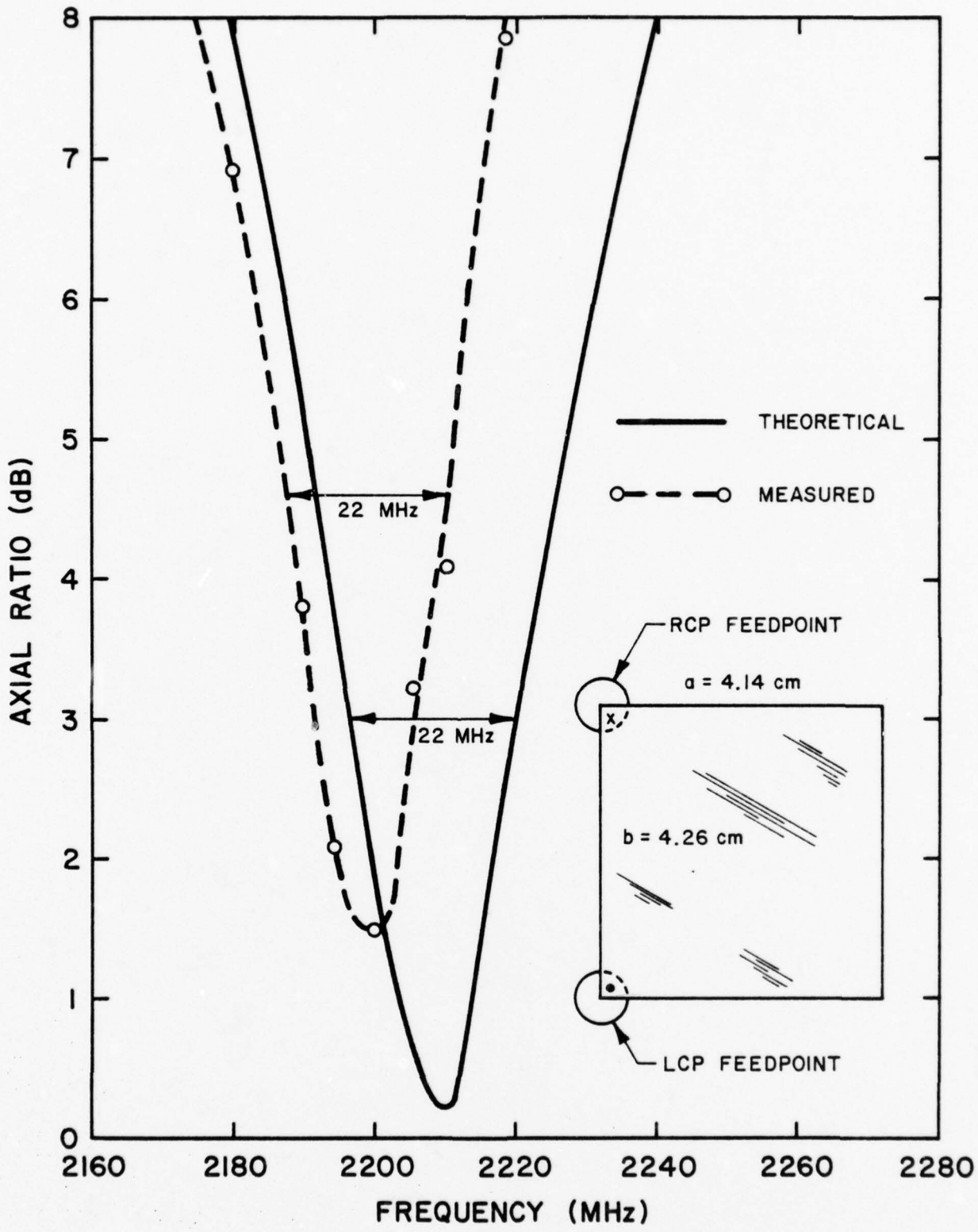

Fig. 4.15 On-axis axial ratio vs. frequency for a corner-fed microstrip patch with a = 4.14 cm and b = 4.26 cm. Solid line is theoretical and dashed line is measured.

4.2 The Circular Patch

Consider a circular microstrip cavity of radius a and substrate thickness t, assumed to be electrically small. The orthonormal electric field mode vectors, which are again assumed TM to z, satisfy the Neumann condition for a non-radiating cavity and are given by

$$\bar{e}_{nr}(\rho,\phi) = \hat{z}\,\frac{\chi_n}{a\sqrt{2\varepsilon\pi t}\;A_{nr}}\;J_n(k'_{nr}\,\frac{\rho}{a})\,\cos n\phi \tag{4-41}$$

where

$$\chi_n = \begin{cases} \sqrt{2} & \text{if } n = 0 \\ 1 & \text{if } n = 1 \end{cases} \tag{4-42}$$

and

$$A_{nr} = \begin{cases} J_o(k'_{or}) & \text{if } n = 0 \\ \dfrac{1}{k'_{nr}}\left[\sum_{k=0}^{\infty} (n+1+2k)\; J^2_{n+1+2k}(k'_{nr})\right]^{1/2} & n \neq 0 \end{cases} \tag{4-43}$$

and where the eigenvalue k'_{nr} is the r^{th}-ranked root of the Neumann condition

$$J'_n\,(k'_{nr}) = 0 \tag{4-44}$$

Table 4-3 lists in ascending order of frequency the eigenvalues for a few of the lower-order modes [Abramowitz and Stegun, 1964].

Table 4-3

Eigenvalues of $J'_n(k'_{nr}) = 0$

Mode (n,r)	Eigenvalue k'_{nr}
0,0	0
1,0	1.84118
2,0	3.05424
0,1	3.83170
2,1	4.20119
1,1	5.33144
2,1	6.70613
0,2	7.01558

The resonant wavelengths are then calculated by

$$\lambda_o = \frac{2\pi\sqrt{\varepsilon_r}\, a}{k'_{nr}} \tag{4-45}$$

Radiation patterns for the TM_{010} mode have been measured and calculated by Carver [1976] and more recently and completely by Lo, et. al. [1977]. The dominant TM_{100} mode has a resonant frequency given by

$$f_r = \frac{c\ (1.84118)}{2\pi a\ \sqrt{\varepsilon_r}} \tag{4-46}$$

where c is the speed of light in vacuum. The normalization constant A_{10} for this mode is computed numerically from (4-43) to be 0.33887. The $\bar{e}_{10}$ mode is zero at the center of the patch and has a maximum amplitude at $\phi = 0$ and $\phi = \pi$; however, the electric fields in the edge walls are 180° out of phase at these diametrically opposite points. Such a mode produces a broadside pattern at the resonant frequency and has been used successfully in practical array designs [Parks & Bailey, 1977]. This mode may be excited by either a probe or a microstrip transmission line feed at the edge.

As before, the total field of a probe-excited cavity can be expanded in terms of the mode vectors. For a radiating cavity with a finite Q, this becomes

$$E_z(\rho,\phi) = - I_{in}\ (j\omega) \sum_{n=0}^{\infty} \sum_{r=0}^{\infty} \frac{t\ e_{nr}(\rho_o,\phi_o)\ e_{nr}(\rho,\phi)}{\omega^2 - \omega_{nr}^2(1 + \frac{j}{Q})} \tag{4-47}$$

where (ρ_o,ϕ_o) is the feed-point location. The input impedance is then

$$Z_{in} = j\omega \sum_{n=0}^{\infty} \sum_{n=r}^{\infty} \frac{t\ e_{nr}^2(\rho_o,\phi_o)}{\omega^2 - \omega_{nr}^2(1 + \frac{j}{Q})} \tag{4-48}$$

In the vicinity of a resonant frequency, this becomes

$$Z_{in} = j\ X_L - j\omega \frac{t\ e_{nr}^2(\rho_o,\phi_o)}{\omega^2 - \omega_{nr}^2(1 + \frac{j}{Q})} \tag{4-49}$$

Using $A_{10} = 0.33887$ along with eqns. (4-41) and (4-42), the mode vector for this dominant mode is

$$e_{10}(\rho_o, \phi_o) = \frac{1.6658}{a\sqrt{\varepsilon t}} \; J_1(1.84118 \frac{\rho_o}{a}) \cos \phi_o \tag{4-50}$$

The first term in (4-49) is the series inductive reactance associated with the probe and is computed from eqn. (4-24). For a circular patch fed by a microstrip transmission line this first term is not present. The second term is of the same form as the impedance of an RLC circuit, i.e.

$$Z = \frac{j\omega/C}{\omega^2 - \omega_{nr}^2(1 + \frac{j}{Q})} \tag{4-51}$$

where

$$\omega_{nr}^2 = 1/(LC) \tag{4-52}$$

$$Q = R/(\omega L) \tag{4-53}$$

Thus, substituting (4-50) into (4-49) and noting the analogies (4-51) - (4-53), the following relationships are obtained:

$$R = \frac{Q}{\omega_{nr}} \frac{2.775t}{\varepsilon a^2} \; J_1^2(1.84118 \frac{\rho_o}{a}) \tag{4-54}$$

$$L = \frac{1}{\omega_{nr}} \frac{2.775t}{\varepsilon a^2} \; J_1^2(1.84118 \frac{\rho_o}{a}) \tag{4-55}$$

$$C = \frac{\varepsilon a^2}{2.775t} \; J_1^{-2}(1.84118 \frac{\rho_o}{a}) \tag{4-56}$$

At resonance, the input resistance is equal to the reciprocal of the total effective wall conductance G_w. An exact solution to this theoretical problem of the wall admittance for this geometry has not been found by the author; however, an approximate form will be given in a subsequent paragraph.

For a radiating cavity, the Neumann condition is not satisfied; the impedance boundary condition means that (1) the eigenvalues and eigenvectors

are no longer purely real, and (2) the resonant frequencies will be slightly less than those obtained for the closed cavity case. The transcendental equation for the eigenvalue of the TM_{100} mode can be shown to be

$$J_1'(k_{10}') = - \alpha J_1(k_{10}') \tag{4-57}$$

where

$$\alpha = j \frac{Z_o Y_w t}{\lambda_o a} \tag{4-58}$$

and where differentiation is with respect to ρ, $Z_o = 376\ \Omega$, and Y_w is the wall admittance. If $Y_w = 0$, then (4-57) reduces to the Neumann condition (4-44) for n = 1. By use of a recursion relationship, (4-57) can be written in a more convenient form as

$$k_{10}' J_o(k_{10}') = (1 - \alpha a) J_1(k_{10}') \tag{4-59}$$

To solve this equation for the eigenvalue k_{10}', it is convenient to use the polynomial approximations for J_o and J_1 as given in Abramowitz and Stegun [1961]; the appropriate value will be slightly less than the Neumann condition value, i.e. 1.84118. Table 4-4 lists both the eigenvalues and the fractional reduction in resonant frequency for several values of αa.

Table 4-4

Eigenvalues for Impedance Boundary Condition and Fractional Reduction in Resonant Frequency

αa	k_{10}'	f_r / f_{ro}
0 (Neumann condition)	1.84118	1.00000
-.01	1.83345	0.99580
-.02	1.82567	0.99158
-.02025	1.82567	0.99145
-.03	1.81780	0.98730
-.04	1.80988	0.98300
-.05	1.80190	0.97867

The relationship of the values from (4-58) to the values tabulated can be made directly if it is assumed that the wall susceptance is much greater than the wall conductance; this is usually the case.

Since the power in the radiating walls varies as $\cos^2\phi$ for the TM_{100} mode, the effective radiating length is half the circumference. Thus, if a is not too small, the relationships for a planar parallel-plate TEM guide radiating into a half-space (eqns. 4-17 and 4-18) may be adapted to the circular patch, replacing a (in the previous equations) with πa in the present case, so that the wall conductance is

$$G_w \simeq 0.00836 \frac{\pi a}{\lambda_o} \quad (\mho) \tag{4-60}$$

The wall susceptance is adapted from the open ended microstrip capacitor (eqns. 4-18) and is thus

$$B_w \simeq 0.00834 \frac{\pi a}{\lambda_o} \varepsilon_r \quad (\mho) \tag{4-61}$$

where $\Delta\ell/t$ has been taken as 0.5.

As a numerical example, consider a circular patch with a = 6.75 cm, t = 0.1588 cm, and $\varepsilon_r = 2.65$. The resonant frequency for the Neumann condition can be found from (4-46) as 800.0 MHz. From (4-61), $B_w = .0125\,\mho$ and from (4-60), $G_w = 0.00178\,\mho$. From (4-58), $\alpha = -.003$ cm^{-1}. A solution to the impedance boundary condition, with $\alpha a = -.02025$, gives $k'_{10} = 1.82567$ as shown in Table 4-4. This corresponds to a 99.145% reduction in the resonant frequency, so that the predicted resonance is 793.2 MHz.

This example was chosen to correspond to measured data for a patch of the same size [Lo, et. al., 1977, p. 36]. The measured resonant frequency was 794 MHz, which is in nearly perfect agreement with the above calculation. This appears to confirm that (4-61) is a good approximation. Fig. 4.16 is a comparison between the theoretical input impedance, based on eqns. 4-49 (without the probe inductance) through 4-61, and experimental values measured by Lo, et. al. There is generally good agreement, except that the measured input resistance at resonance is slightly larger than the theoretical value.

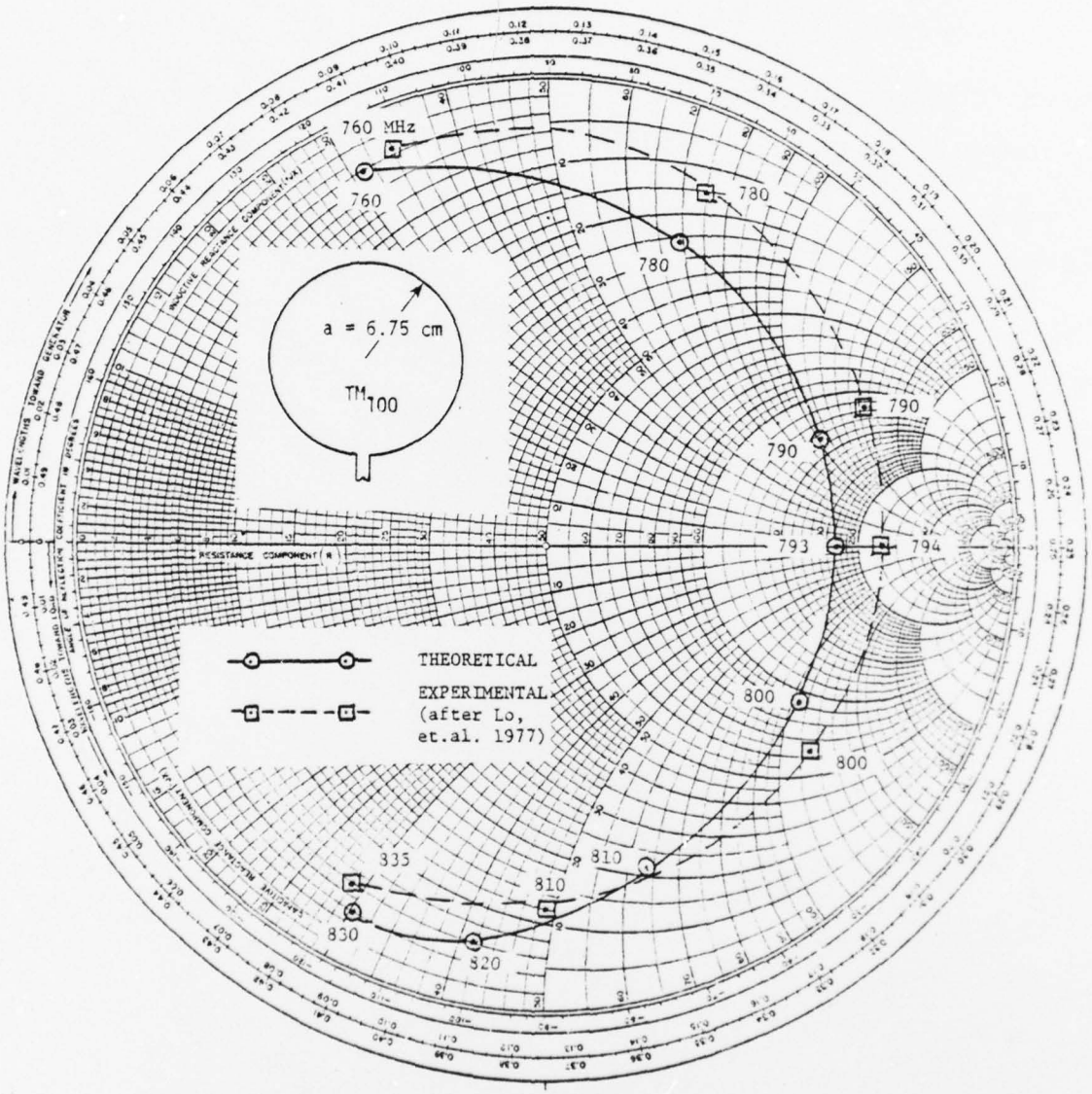

Fig. 4.16 Comparison between theoretical and experimental input impedances to a circular microstrip patch with a = 6.75 cm, t = 0.1588 cm, and ε_r = 2.65.

4.3 The Pentagon Patch

In Sec. 4.1.3, it was pointed out that circular polarization is theoretically possible from a microstrip antenna with a single feedpoint, if two spatially orthogonal modes were excited in phase quadrature.

A practical example of such an antenna has been reported by Weinschel [1975] who obtained circular polarization over a 1% bandwidth from a five-sided microstrip patch, shown in Fig. 4.17. This antenna has been used in an S-band cylindrical array producing circular polarization [Weinschel, 1975] and in a UHF scanning array for buoy or ship communication to a satellite [Weinschel and Carver, 1976].

A typical impedance plot for an S-band pentagon microstrip patch is shown in Fig. 4.18. The loop at 2279 MHz is evidence of the existence of two modes, as discussed previously in Sec. 4.1.3.

The modal expansion for the interior fields of such a polygon cannot be carried out by the classical technique of separation of variables since the boundary conditions cannot be imposed in a simple fashion. The method of finite elements can be used, however, by application of the principles discussed in Sec. 3.0. In fact, this antenna serves as an illustration of the true power of the finite element method.

Table 4-5 lists the computed eigenvalues (using program MICRO) for the first eight modes of a UHF pentagon patch whose first non-zero resonant frequency was measured to be 469 MHz. The grid and nodes used for computational purposes is shown in Fig. 4.19.

Table 4-5

Results of Finite Elements Computed Values of Lower Eight Eigenvalues and Resonant Frequencies for Pentagon Microstrip Antenna

n	K_n	f_n
1	0	0
2	0.1046 cm^{-1}	499 MHz
3	0.1112	531
4	0.2902	1384.4
5	0.4595	2062.2
6	0.4799	2153.6
7	0.7733	3470.2
8	0.8672	3891.3

The resonant frequencies were computed assuming a Neumann boundary condition (open circuit at walls) so that the computed values are expected to be a few percent high. The measured f_1 resonance is 0.94 times the calculated value.

Fig. 4.20 is a graph of three of the computed modal $\bar{e}_z$ fields (eigenfunctions) in the radiating walls of the pentagon patch. Since the open-circuit wall impedance condition was used, the mode vectors are entirely real. The eigenvalues and eigenvectors for modes 27, 28 and 31 are shown. It is noted that eigenvalues $\lambda_{28} = k_{28}^2 = 0.1203$ and $\lambda_{27}^2 = k_{27}^2 = 0.13605$ are closely spaced, indicating the possibility of a multiple-mode condition being produced by a single feed.

Fig. 4.21 illustrates the individual magnetic currents in each wall for modes 27 and 28. The net effect is that mode 28 is vertically polarized and mode 27 is horizontally polarized. The relative amplitudes and phases of modes 27 and 28 would be determined by the feedpoint location and the frequency. However, these preliminary results point strongly toward a theoretical prediction of circular polarization for the pentagon patch, if the feedpoint and frequency are properly chosen.

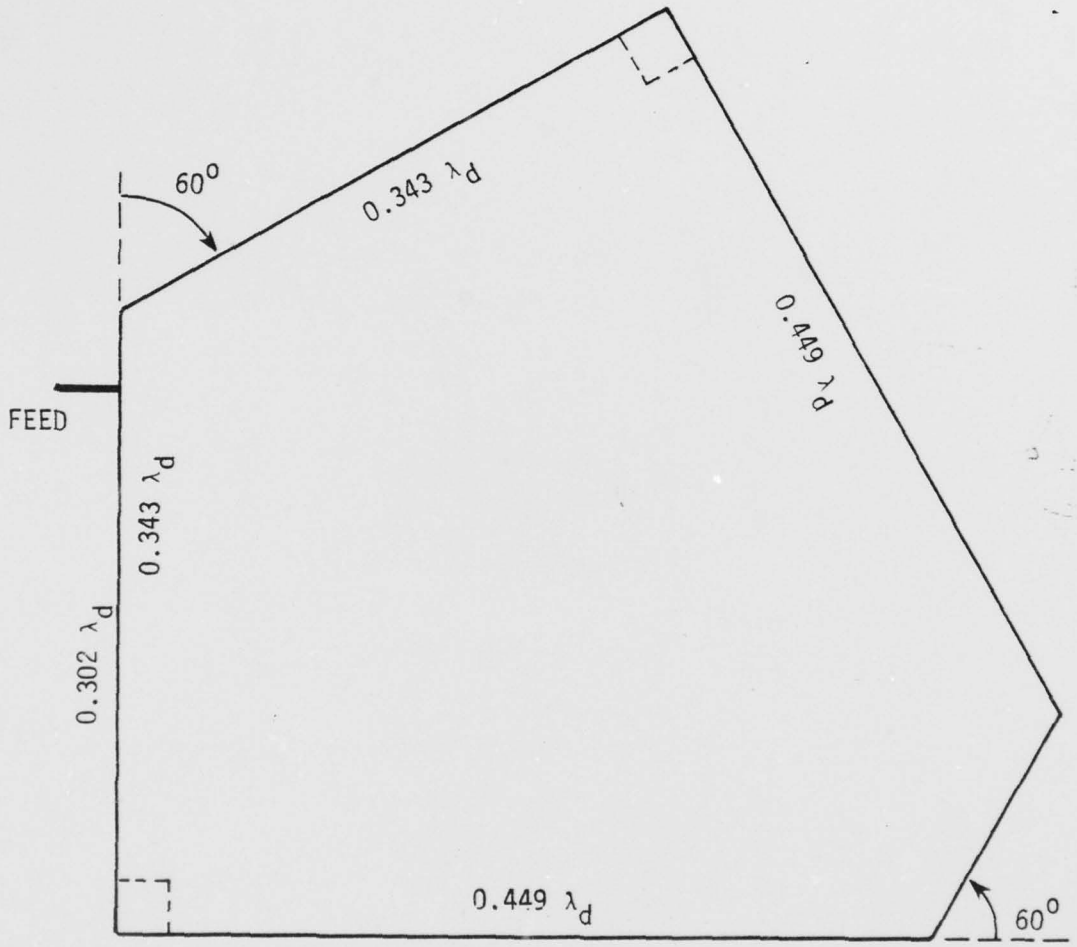

Fig. 4.17 Pentagon microstrip antenna element which produces circular polarization (after Weinschel, 1975).

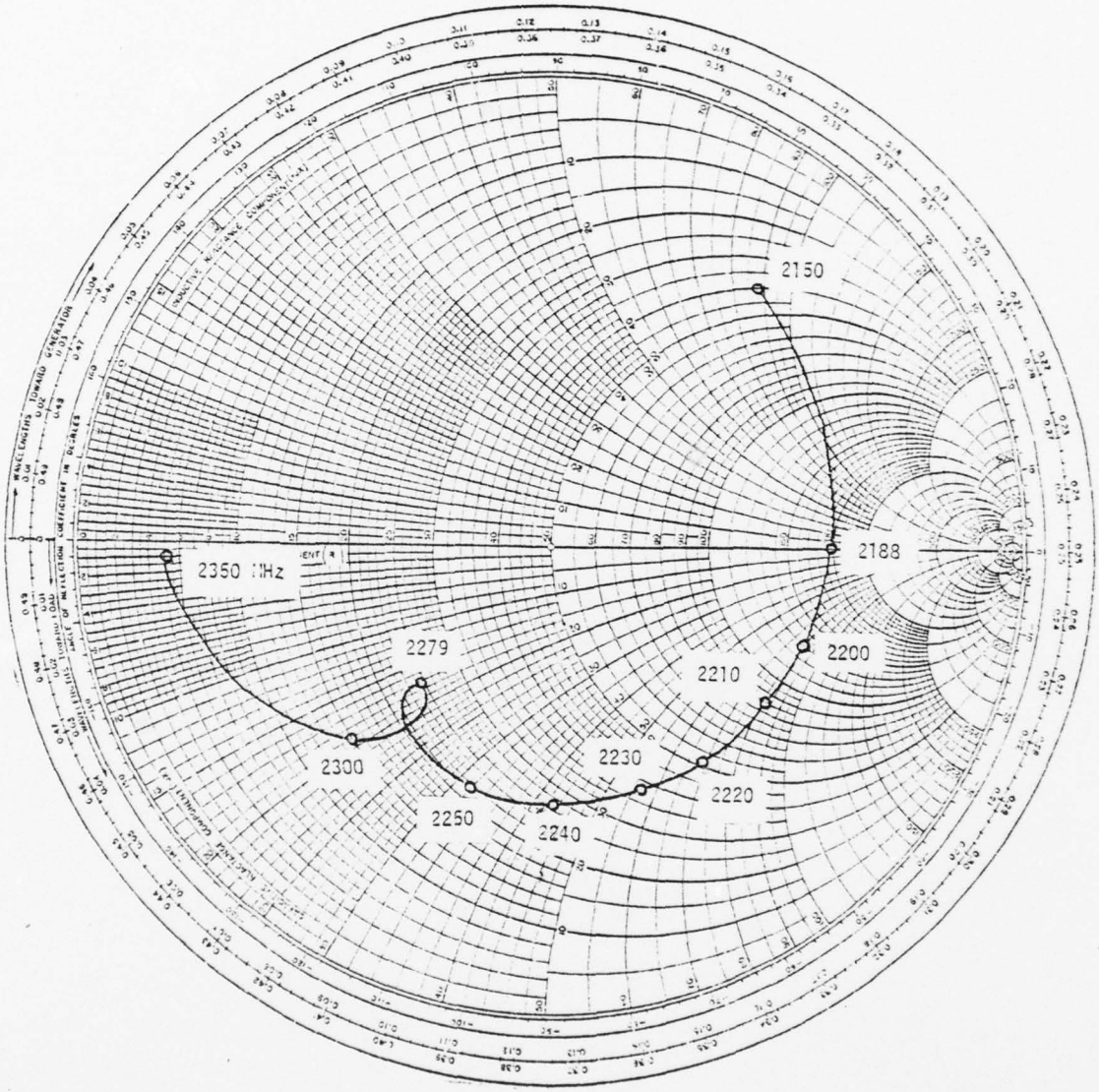

Fig. 4.18 Measured impedance diagram for an S-band pentagon microstrip antenna [Weinschel, 1973]. Impedance includes effect of quarter-wave matching transformer.

10 X 10 TO THE INCH • 7 X 10 INCHES
KEUFFEL & ESSER MADE IN U.S.A.
46 0702

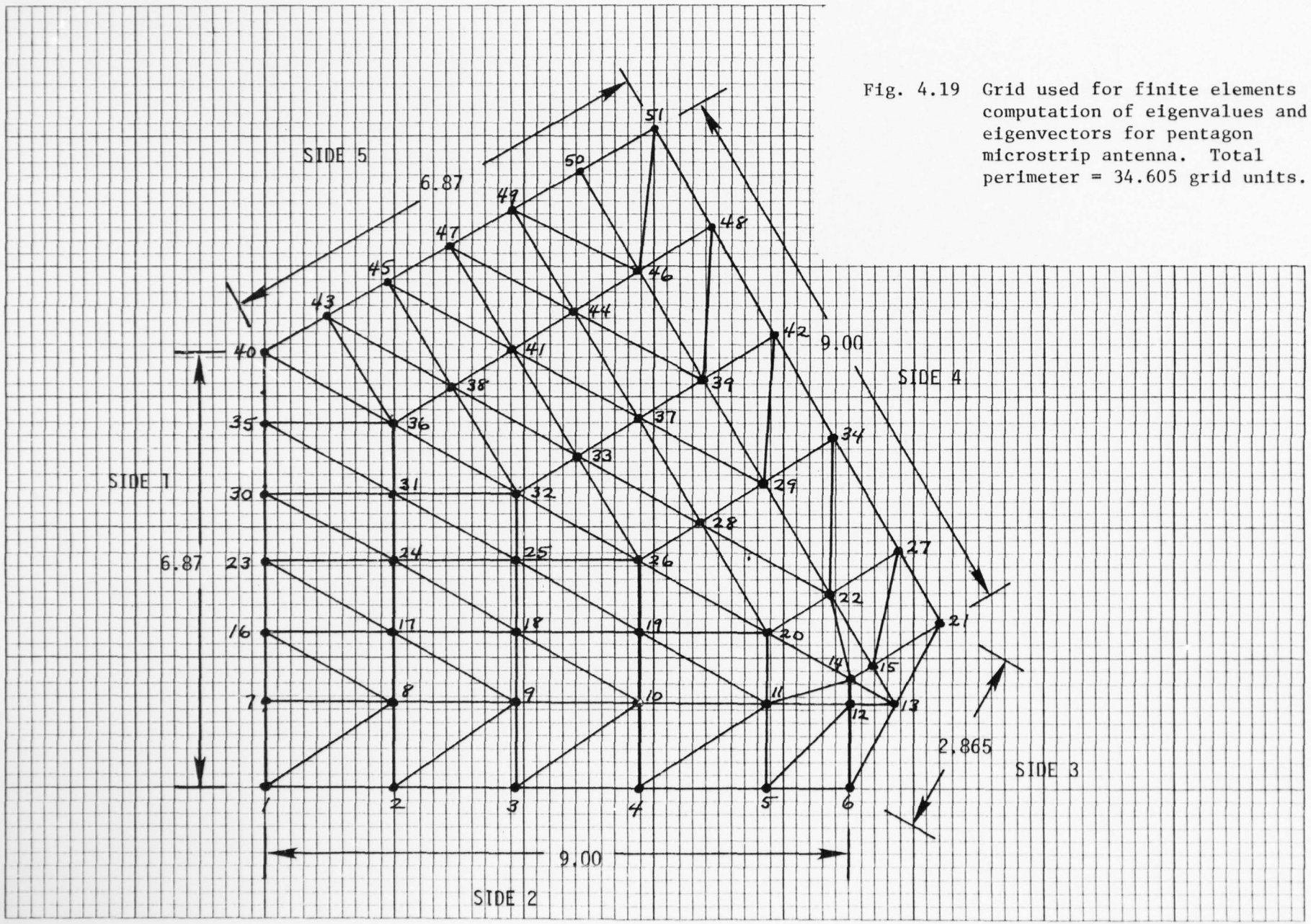

Fig. 4.19 Grid used for finite elements computation of eigenvalues and eigenvectors for pentagon microstrip antenna. Total perimeter = 34.605 grid units.

Fig. 4.20 Graph of the modal electric fields in the pentagon radiating walls as a function of perimeter position (see Fig. 4.19) for modes 27, 28 and 31.

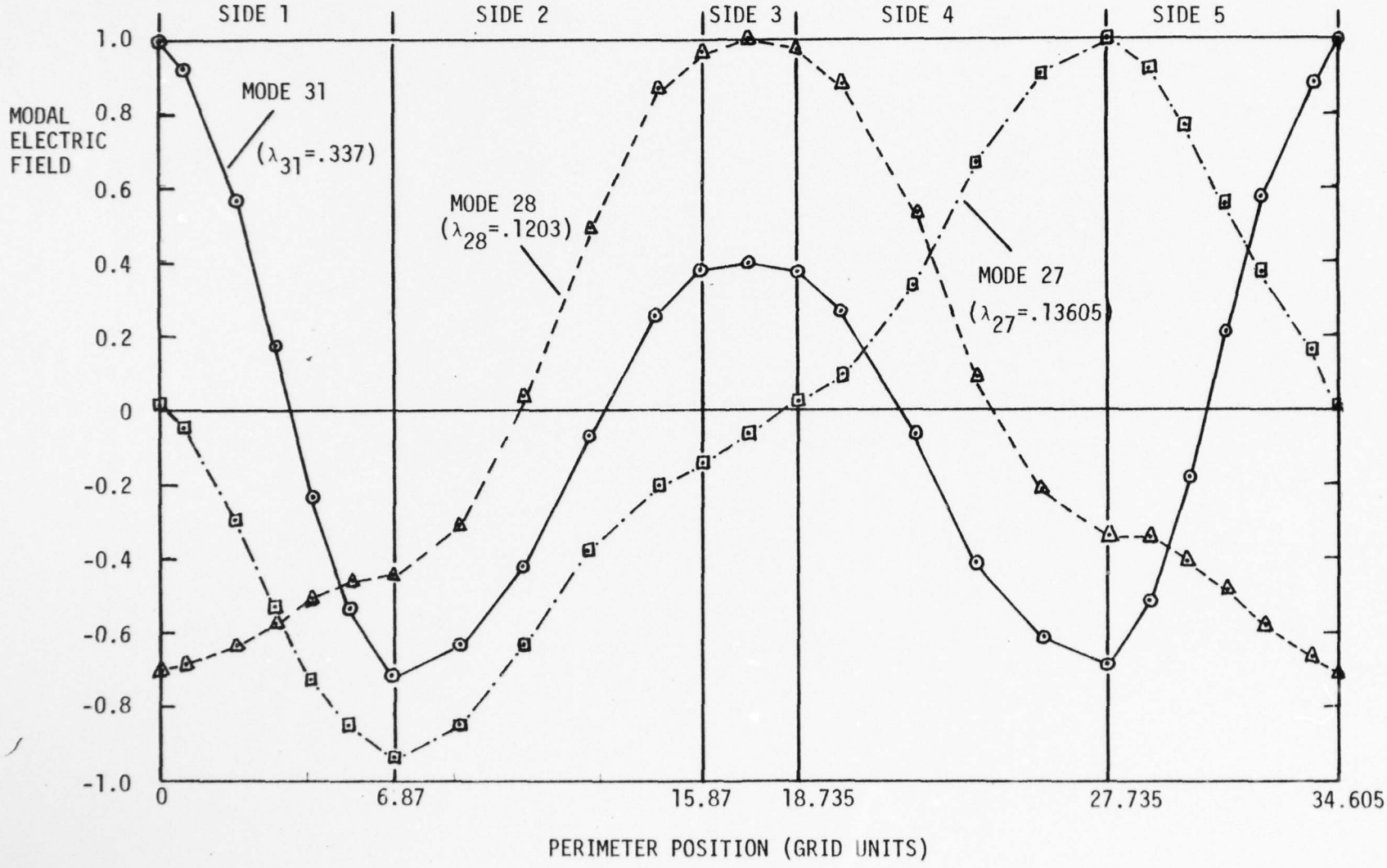

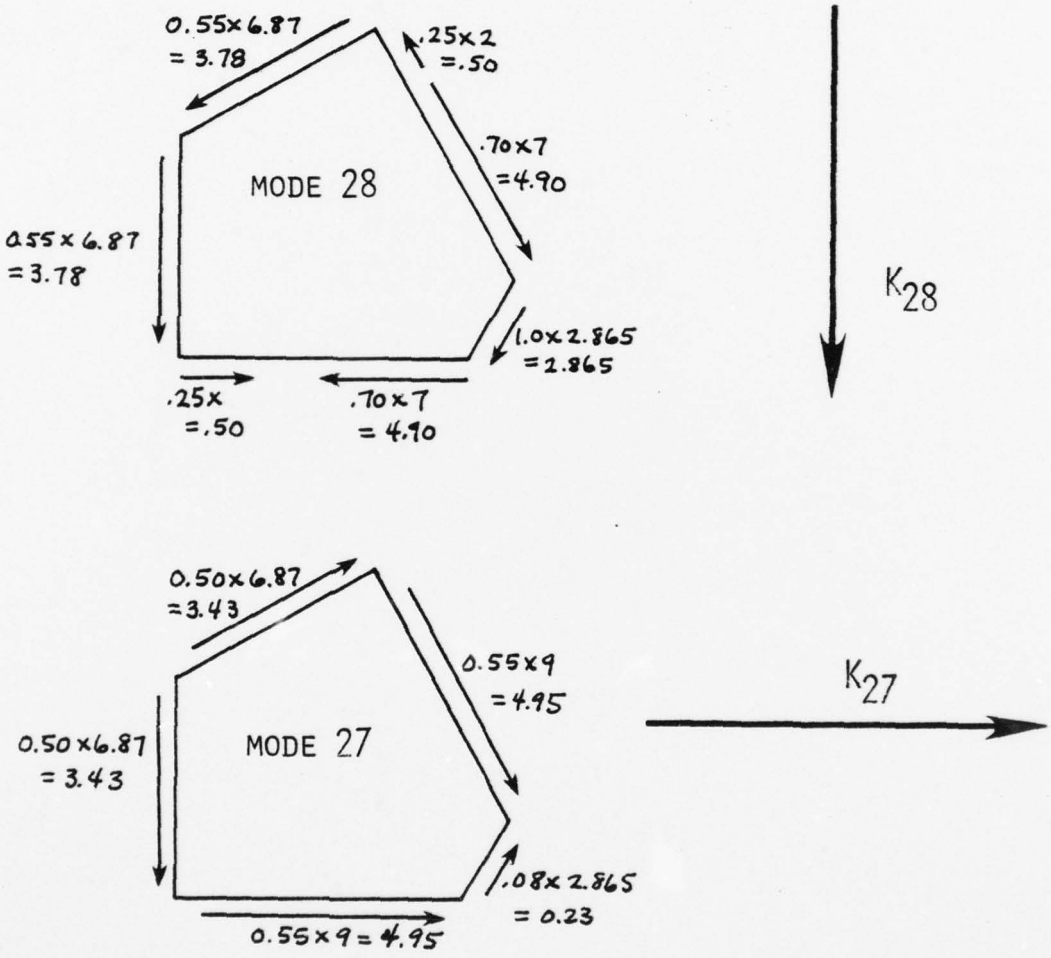

Fig. 4.21 Illustrating individual magnetic currents in each wall for modes 27 and 28; also illustrating vector sum for modes 27 and 28 - K_{27} and K_{28} are within 1% of being perpendicular.

5.0 CONCLUSIONS

This report has presented a method of analysis which can be applied to microstrip antennas. The primary emphasis to date has been on the prediction of the interior fields, since this is a more difficult problem than the prediction of the antenna pattern.

For formulations based on a cavity model with open-circuit walls (fields satisfying a Neumann boundary condition) both the interior mode vectors and eigenvalues are real. However, the microstrip patch presents a wall admittance which is complex, with the capacitive susceptance usually being several times the conductance. Thus, the mode vectors are nearly real and the eigenvalues are nearly real. Solution of a transcendental equation can very accurately predict the resonant frequencies once the appropriate wall admittance is known.

The problem of finding the wall admittance of an arbitrary microstrip patch shape has not yet been solved and emphasis should be placed on finding solutions. However, an approximate formula has been found which uses the conductance of a TEM parallel-plate waveguide and the susceptance of an open-ended microstrip capacitor. This gives good agreement between measured and calculated input impedances for the rectangular and circular patches considered. The input resistance at the resonant frequency is determined by the wall conductance, whereas the resonant frequency is primarly related to the patch dimensions and the wall susceptance.

For a patch fed by a coaxial probe, the input impedance to the patch proper will differ from the measured input impedance to the coaxial connector by a series inductive reactance term, given by eqn. (4-24). This term must be known in order to correct measured impedances with a probe to the true input impedances seen by a microstrip transmission line used in an array design.

When a corner-fed nearly-square patch operates in a two-mode configuration with two closely-spaced resonant frequencies, it is possible theoretically to obtain circular polarization over a 1% bandwidth. This multiple-mode effect, discussed in Sec. 4.1.3, has been experimentally confirmed at PSL.

The method of finite elements has been applied to the analysis of a

five-sided patch which, when properly excited, can produce circular polarization. This analysis, which is in a preliminary stage, confirms the existence of two spatially-orthogonal exterior fields at broadside and at two closely-spaced resonant frequencies. The feedpoint problem has not yet been solved for this geometry.

Both the classical expansion analysis and the numerical analysis approaches will be continued. The finite elements program (MICRO) will be expanded to include (1) sparse matrix algorithms to decrease computer storage requirements and (2) subspace iteration to decrease execution time.

6.0 REFERENCES

Abramowitz, M. and I. A. Stegun (ed.),Handbook of Mathematical Functions, National Bureau of Standards, Applied Mathematics Series 55, U.S. Government Printing Office, Washington, D.C., June, 1964.

Carver, K. R. , "The radiation pattern of a microstrip disc antenna," Physical Science Laboratory, New Mexico State University, Las Cruces; PSL Tech. Memorandum, November 29, 1976.

Coffey, E. L. , "An analog/hybrid computer solution of electromagnetic scattering problems," Ph.D. dissertation, Virginia Polytechnic Institute and State University, Blacksburg; June, 1976.

Coffey, E. L. and K. R. Carver, "Towards the theory of microstrip antenna patterns," 1977 Allerton Antenna Applications Symposium Digest, University of Illinois, Urbana, April, 1977.

Coffey, E. L. and K. R. Carver, "Progress report on an investigation of the analysis and synthesis of microstrip antennas: ARO grant DAAG29-78-G-0082," Physical Science Laboratory, New Mexico State University, Las Cruces, 30 June, 1978.

Derneryd, A. G., "Linearly polarized microstrip antennas," IEEE Trans. Ant. and Prop., pp. 846 - 851, November, 1976.

Deschamps, G. A., "Microstrip microwave antennas," presented at the 3rd USAF Symposium on Antennas, 1953.

Dunn, G. A., "Design and construction of a 3-element microstrip antenna array," Dept. of Electrical and Computer Engineering, New Mexico State University, December, 1978.

Hammerstad, E. O., "Equations for microstrip circuit design," 5th European Microwave Conference, pp. 268-272, Sept., 1975.

Harrington, R. F., "Time-Harmonic Electromagnetic Fields," McGraw-Hill Book Co., New York, 1961.

Holand, I. and K. Bell, "Finite Element Methods in Stress Analysis," Tapir, Trondheim, Norway, 1969.

Howell, J. Q., "Microstrip antennas," IEEE Group on Antennas and Propagation, International Symposium, p. 177, Dec., 1972.

Howell, J. Q., "Microstrip antennas," IEEE Trans. Ant. and Prop., AP-23, pp. 90-93, Jan., 1975.

Kraus, J. D. and K. R. Carver, "Electromagnetics," 2nd ed., McGraw-Hill Book Co., New York, 1973.

Kaloi, C. M., "Corner-fed electric microstrip dipole," Naval Missile Center, Pt. Mugu, California; no date on paper; received in March, 1978.

Lo, Y. T. , D. Solomon, F. R. Ore, D. D. Harrison and G. A. Deschamps, "Study of microstrip antennas, microstrip phased arrays, and microstrip feed networks," Department of Electrical Engineering, University of Illinois, Urbana; Rome Air Development Center report RADC-TR-77-406, 21 October, 1977.

Marcuvitz, N., "Waveguide Handbook," MIT Radiation Laboratory Series, Volume 10, McGraw-Hill Book Co., 1951.

Munson, R. E., "Single slot cavity antenna assembly," U. S. Patent 3713162, Jan. 23, 1973.

Munson, R. E., "Conformal microstrip antennas and microstrip phased arrays," IEEE Trans. Ant. and Prop., pp. 74-78, Jan., 1974.

Newman, E.H., and D. M. Pozar, "Electromagnetic modeling of composite wire and surface geometries," IEEE Trans. Ant. and Prop., AP-26, #6, pp. 784-788, November, 1978.

Parks, F. and M. C. Bailey, "A low sidelobe microstrip array," 1977 IEEE International Symposium on Antennas and Propagation, Stanford Univ., Stanford, California, Digest pp. 77-80, June, 1977.

Schneider, M. V., "Microstrip dispersion," Proc. IEEE, 60, #1, pp. 144-146, Jan., 1972.

Strang, G. and G. J. Fix, "An Analysis of the Finite Element Method," Prentice-Hall, Englewood Cliffs, N. J., 1973.

Weinschel, H. D. , "Progress reports on development of microstrip cylindrical arrays for sounding rockets," Physical Science Laboratory, New Mexico State University, Las Cruces, 1973.

Weinschel, H. D. and R. Lanphere, "Data book on microstrip antenna measurements for S-band array," Physical Science Laboratory, New Mexico State University, Las Cruces, 1973.

Weinschel, H. D., "A cylindrical array of circularly polarized microstrip antennas," 1975 AP-S International Symposium, p. 177 of digest.

Weinschel, H. D. and K. R. Carver, "A medium-gain circularly polarized macrostrip UHF antenna for marine DCP communication to the GOES satellite system," presented at the 1976 IEEE AP-S International Symposium, October 14, 1976.

Wexler, A., "Solution of large systems of algebraic equations," 1978 URSI XIX General Assembly, Helsinki, Finland, Aug. 2, 1978.

Zollenkpof, K. and J. K. Reid (ed.), "Large Sparse Sets of Linear Equations," Academic Press, 1971.

DISTRIBUTION

(2) Dr. James Mink
Army Research Office
Box 12211
Research Triangle Park
North Carolina 27709

(2) Dr. Dan Schaubert
Harry Diamond Laboratories
2800 Powder Mill Rd.
Adelphi, Md. 20783

(2) Dr. Edgar L. Coffey, III
BDM Corporation
2600 Yale Blvd. S.E.
Albuquerque, N. M. 87106

(1) Dr. M. C. Bailey
NASA Langley Research Center
Hampton, Virginia

(1) Dr. Chalmers M. Butler
Department of Electrical Engineering
University of Mississippi
University, Mississippi

(1) Dr. Robert Elliott
School of Engineering & Applied Science
University of California at Los Angeles
Los Angeles, California

(1) Mr. Cyril M. Kaloi
Pacific Missile Test Center
Point Mugu, California 93042

(1) Dr. Y. T. Lo
Department of Eleetrical Engineering
University of Illinois at Urbana/Champaign
Urbana, Illinois 61801

(1) Dr. Ed Newman
Electroscience Laboratory
The Ohio State University
Columbus, Ohio 43212

(1) Dr. L. C. Shen
Department of Electrical Engineering
University of Houston
Houston, Texas

Mr. Robert E. Munson
Aerospace Division
Ball Brother Research Corporation
Boulder, Colorado 80302

Dr. C. H. Walter
Electroscience Laboratory
The Ohio State University
Columbus, Ohio 43212

Dr. James S. Yee
The Boeing Aerospace Co.
Seattle, Washington

END

DATE
FILMED

6-79

DDC